

AD-A064 737

AIR FORCE INST OF TECH WRIGHT-PATTERSON AFB OHIO SCH--ETC F/G 17/8  
FUNDAMENTAL LIMITATIONS OF OPTICAL TRACKERS.(U)

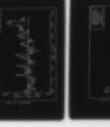
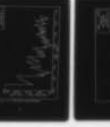
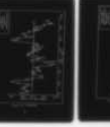
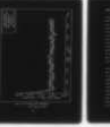
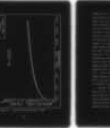
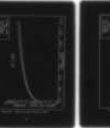
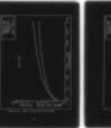
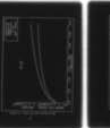
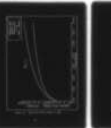
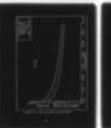
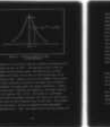
DEC 78 J M SANTIAGO

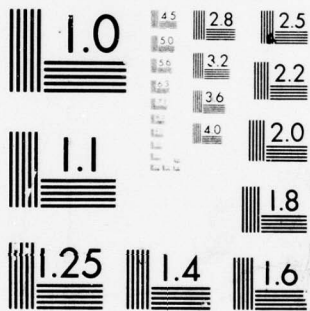
AFIT/GE0/EE/78-4

UNCLASSIFIED

NL

1 OF 2  
AD  
A0 647 37





MICROCOPY RESOLUTION TEST CHART  
NATIONAL BUREAU OF STANDARDS-1963-A



ADA064737

DDC FILE COPY



UNITED STATES AIR FORCE  
AIR UNIVERSITY  
AIR FORCE INSTITUTE OF TECHNOLOGY  
Wright-Patterson Air Force Base, Ohio

DISTRIBUTION  
Approved  
Distribution

79 01 30 13

AFIT/GEO/EE/78-4

FUNDAMENTAL LIMITATIONS  
OF OPTICAL TRACKERS

THESIS

AFIT/GEO/EE/78-4      John M. Santiago, Jr.  
2nd Lt                      USAF

Approved for public release; distribution unlimited

79 01 30 135

AFIT/GEO/EE/78-4

# FUNDAMENTAL LIMITATIONS OF OPTICAL TRACKERS.

# THESIS

⑨ Master's thesis

Presented to the Faculty of the School of Engineering  
of the Air Force Institute of Technology

Air Training Command

in Partial Fulfillment of the  
Requirements for the Degree of  
Master of Science

by

John M. Santiago, Jr  
2nd Lt USAF

Graduate Electro-optics

~~December 1978~~

AD6733104 68

NAME \_\_\_\_\_

DOB \_\_\_\_\_

SEX \_\_\_\_\_

JOB \_\_\_\_\_

SSN \_\_\_\_\_

DATE \_\_\_\_\_

TIME \_\_\_\_\_

BY \_\_\_\_\_

REMARKS \_\_\_\_\_

1

Approved for public release; distribution unlimited

042 225

## Preface

This thesis was under the sponsorship of the Air Force Weapons Laboratory at Kirtland Air Force Base in New Mexico. It is a theoretical study to determine the performance capabilities of optical trackers when fundamentally limited by the quantum nature of light and the photon detectors used to detect the optical fields. This study involves a knowledge of optical communications, optimal filter theory, and software simulation techniques that made the study interesting.

I would like to first thank Capt Stan Z. Lewantowitz for sponsoring this thesis, and Maj Joseph W. Carl for his interest in this work. I am extremely thankful to my thesis advisors, Dr. Peter S. Maybeck and Capt Stanley R. Robinson, for their guidance, expertise, and patience that they have given to me during this research study. Also, I would like to give many thanks to Cindy Held and Sheri Vogel for burning the midnight oil in typing this final product. Finally, even though thousands of miles away, I would like to thank my mom and dad and the rest of my family for their encouragement and moral support during this period of learning.

John M. Santiago, Jr.

## Contents

Preface . . . . .	11
List of Figures . . . . .	v
List of Tables . . . . .	vii
Abstract . . . . .	viii
I Introduction . . . . .	1
Background . . . . .	1
Method of Tracking . . . . .	1
Quantum Effects . . . . .	3
Measurement Models . . . . .	5
Assumptions of the Snyder Filter . . . . .	7
Problem . . . . .	8
Overview and Approach . . . . .	8
II Snyder Filter and its Open Loop Estimation	
Performance . . . . .	13
Optical Receiver Model . . . . .	13
General Description . . . . .	14
Photodetectors . . . . .	14
Detector Noise . . . . .	17
Photodetector Statistics . . . . .	19
The Snyder Filter . . . . .	22
Characterization of Spot . . . . .	22
Characterization of Spot's Motion . . . . .	23
Position-Sensitive Measurements . . . . .	25
Snyder's Filter Equations . . . . .	25
Upper and Lower Bounds . . . . .	31
Summary . . . . .	44
III Simulation of the Snyder Filter and	
Performance Analysis . . . . .	46
Simulation of Spot's Dynamics . . . . .	46
Noise Generators . . . . .	49
Point Process Generation in Time and Space . . . . .	50
Binomial Method . . . . .	51
Transformation Equation . . . . .	53
Conditional Method . . . . .	54
Aspects of Implementing each method . . . . .	63
Performance Analysis . . . . .	66
Sample Statistics . . . . .	68
Plots . . . . .	68
Test Cases . . . . .	70
Summary . . . . .	70



IV	Results . . . . .	72
	Mean and Variance Convergence . . . . .	72
	Binomial Method (without dark current) . . . . .	81
	Conditional Method (without dark current) . . . . .	90
	Conditional Method (with dark current) . . . . .	104
	Summary . . . . .	140
V	Conclusions and Recommendations . . . . .	149
	Conclusions . . . . .	149
	Recommendations . . . . .	150
	Bibliography . . . . .	152
	Appendix A . . . . .	153
	Appendix B . . . . .	160
	Vita . . . . .	165

## List of Figures

	<u>Page</u>
1. Target Within Field-of-View of Direct Detection Optical Receiver . . . . .	2
2. Direct Detection Optical Receiver . . . . .	15
3. Photodetector Model . . . . .	16
4. Intensity Profile of Spot in One-Dimension . . . . .	24
5. Properties of a First Order Markov Process . . . . .	26
6. Upper and Lower Bounds on MSE . . . . .	33
7. Flowchart of Binomial Method . . . . .	52
8. Generation of a Specified Probability Distribution . . . . .	54
9. Resolution Problem in Binomial Method . . . . .	65
10. Sampling the Error Process with Fixed Sample Period (Conditional Method) . . . . .	67
11. Mean and Variance Convergence . . . . .	73
12. X-Position Variances (Sample Runs) . . . . .	76
13. X-Position Error and Filter Variance (Sample Run) . . . . .	82
14. X-Position and Filter Variance (Sample Run 2). . . . .	84
15-17. X-Position Variances (3 test cases in Binomial Method). . . . .	87
18. X-Position (mean error $\pm$ one standard deviation) . . . . .	91
19. X-Position error and Filter Variance (Conditional Method) . . . . .	92
20. "Time-Average" Technique . . . . .	94
21. Simulation Values of True and Filter Variances . . . . .	96
22. A Test Case of Conditional Method (without dark current) . . . . .	100
23. X-Position Variances (steady-state and confidence issues) . . . . .	105
24-28. Test Cases of Conditional Method (with dark current) . . . . .	108

29-32.	Sample Runs of Error Process and Filter Variance to Observe Filter's Sensitivity. . . . .	123
33-36.	X-Position Variances (ad hoc methods of compensation) . . . . .	148
A1	Infinitesimally-fined Detector Array. . . . .	155
A2.	Partitions of x-axis,y-axis and t-axis. . . . .	155
A3.	Time-Space Counting Process . . . . .	155



## List of Tables

1. Test Cases for Binomial Method (without dark current) . . 71
2. Test Cases for Conditional Method (without dark  
current). . . . . 71
3. Test Cases for Conditional Method (without dark  
current) . . . . . 95
4. Test Cases for  $X=5$  and  $Y=1$  (with dark current) . . . . .138
5. Test Cases for  $X=20$  and  $Y=1$  (with dark current) . . . . .139

### Abstract

A problem is considered to determine the tracking capabilities of an estimator, applied in optical sensing. The estimator tracks the centroid of a one-dimensional Gaussian-shaped intensity based on time-space point process measurements. The centroid assumes to move dynamically as a First Order Gauss-Markov process. Filter performance is described by steady-state upper and lower bounds on mean-square-error (MSE) which are evaluated as a function of two physically motivated parameters: average number of photons detected in a coherence time of centroid dynamics and mean square value of centroid jitter normalized by the square of the beam width. The parameters establish regions of operations where upper and lower bounds converge to the actual MSE. Results from the Monte Carlo simulation demonstrates the bounds' usefulness. Noise measurements from dark current or background radiation are included in the simulation. Results show that the filter is very sensitive to these measurements, resulting in very poor tracking. Ad hoc methods of filter tuning and residual monitoring are employed to improve tracking performance; results indicate that filter performance can be improved substantially through residual monitoring.

## Fundamental Limitations of Optical Trackers

### I. Introduction

Alignment problems exist in any optical system. To image a point object over large distances requires aligning an optical receiver with the object. When the object is within the receiver's field-of-view, an image is formed on the photodetector surface. This is shown in Fig. (1). Because the optical receiver has a relatively narrow field-of-view, aligning the receiver becomes difficult. Furthermore, because of variations of index of refraction in the atmosphere and other outside disturbances that cause relative motion between receiver and object, active alignment is necessary. Thus, optical trackers are needed to keep the object within the receiver's field-of-view.

#### Background

Several methods are currently being developed in the Air Force to track the target in presence of several disturbances. The disturbances include target motion, mirror vibration, beam jitter, stochastic effects of the atmosphere, and other processes that can cause relative motion between the beam and target.

Method of Tracking. One scheme to accomplish this tracking task uses a direct detection optical receiver to determine the arrival angle of the incident radiation at the receiver. The arrival angle is converted (through optics) into a position of a spot of light on the active surface of a photodetector array. Once this angle arrival is determined, it can be used to generate error signals to other tracking components to correct

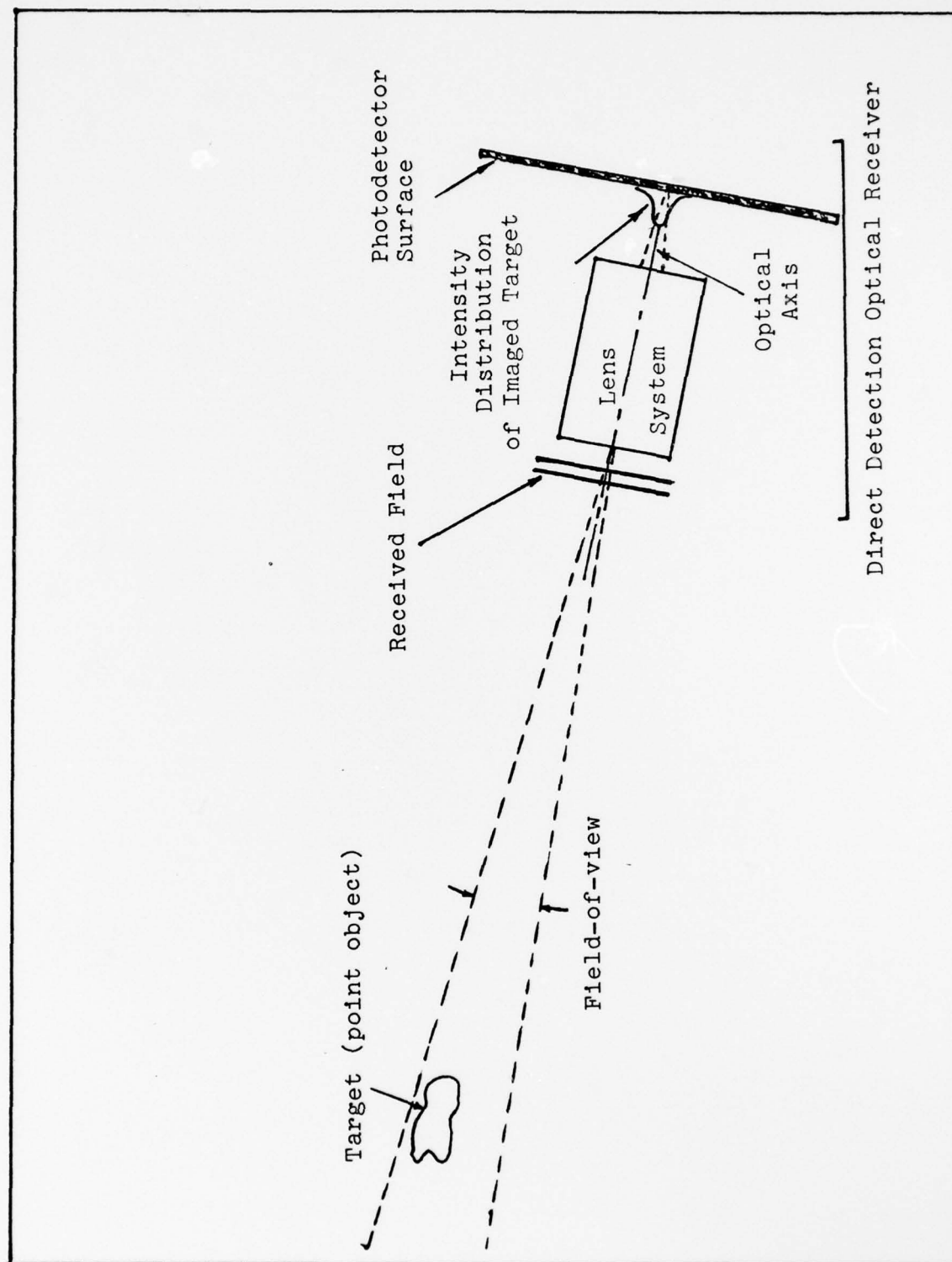


Figure 1. Target Within Field-of-View of Direct Detection Optical Receiver

any offset alignment between the receiver and target that may occur. Because of disturbances that cause relative motion between the beam and target, the beam's arrival angle varies at the optical receiver. Thus, variations of arrival angle are therefore converted into variations of the spot's position on the detector surface. The spot of light moves dynamically on the surface, releasing photoelectrons statistically distributed about the spot's position of maximum intensity.

A minimum-mean-square estimator which will be known as the Snyder Filter estimates the position of maximum intensity based on the observations of the photoelectrons (Ref. 1). These photoelectrons are measurement data to the filter in order to obtain an estimate of the spot's current position. Here, the Snyder Filter assumes that the measurements only include the target's signal intensity. However, other disturbances also cause photoelectrons to be released from the surface. These disturbances which degrade the Snyder Filter's tracking capability are caused by background radiation from the sky, moon, sun, stars, and other sources, and dark current present in the absence of photoexcitation on the photodetector. Each of the noise sources are discussed in the next chapter. It should be noted, however, that thermal noise is ignored for photodetectors with high gain, such as a photomultiplier or avalanche photodiode.

Quantum Effects. At higher frequencies, the quantum nature of light is an important consideration in many optical measurement systems which use photon or quantum detectors to detect these optical fields. In this case, light can be described as



a collection of discrete packets of energy called photons. With a given probability, each photon converts into an electron. These photoelectrons, distributed in time and space, are released from the photodetector surface. Because of these quantum effects in the detection process, especially when the field intensity is low at the receiver's input, there is an uncertainty associated with estimating the spot's position of maximum intensity based on the sensed photoelectrons. Theoretically, both the quantum nature of light and the nature of the detection process fundamentally limit the tracking capability of optical trackers (in other words, the ability to detect the signal photons is the fundamental limit).

Because of the quantum effects associated in the detection process, the statistics of the receiver's output process must be described accurately; the Snyder Filter is based on these statistics. Experimental evidence indicates that the statistics of the output can be modelled as a random point process in time and space conditioned on knowing the optical field incident on the receiver (Ref. 2). A random point process by definition is "a mathematical model to describe a physical phenomenon characterized by highly localized events distributed randomly in a continuum (Ref. 3:2)." The discrete events are the photoelectrons or photoconversions distributed randomly on the photodetector surface. Associated with each event are the temporal and spatial location of the photoelectron. Here, the event location is used as distributed measurement or data,

in order to estimate the current position of maximum intensity. To summarize, the point process model describes the fundamental uncertainty of photon-to-electron conversion in the measurement or detection process.

Measurement Models (Gaussian versus Point Process Descriptions). To contrast the point process measurement description with other noise models, several Gaussian descriptions modelling different types of noise are briefly presented. A stationary white noise is one model which describes noise as having a power spectral density of infinite bandwidth, having energy at all frequencies. Also, infinite bandwidth implies that the noise samples are uncorrelated in time. Although no noise has infinite bandwidth, the white noise model does provide a reasonable description for wideband noise having a wider bandpass than the physical system of interest. In other words, the wideband noise appears white with respect to the system. In many instances, however, noises are not well modelled as uncorrelated in time (e.g., bandlimited noise), and other models must be exploited. For such causes, a Gaussian white noise, driving the input of a small linear system, can generate an output that duplicates or closely approximates the second order characteristics of a given noise source. The linear system, or "shaping filter", duplicates the second order statistics of the actual noise by generating a Gaussian process with the same second order statistics. For example, the statistics of a zero-mean exponentially time-correlated (First Order Markov) noise can be duplicated by taking the output

statistics of a first order lag driven by white-Gaussian noise of zero mean. This model approximates a variety of experimentally observed random behavior that have wide or narrow bandwidths with a flat power spectral density. Another noise model is the Second Order Markov process model which describes phenomena having vibration, bending or any other periodic random characteristics. This process can be generated as the output of a second order system driven by white noise.

The different models that were just described typically model noise as due to a number of sources that are always present (or continuous) in a dynamics system or measurement device. By the Central Limit Theorem of Statistics, when a number of random variables are added together, the sum of these random variables has a probability distribution which is nearly Gaussian, regardless of the shape of the individual densities. The Gaussian models are exploited in many cases where macroscopic phenomenon are observed. On the other hand, the quantum effects are observed as a microscopic interaction between the photons in the incident field and the atoms on the photodetector surface. The result of this discrete interaction is the probability of releasing a photoelectron at a particular time and location from the photodetector array. Thus, various disturbances affecting a system or measurement device cannot always be described as having additive corrupted noise with Gaussian statistics. To incorporate the quantum effects or uncertainty, the random point process description is used to model the measurement process from the optical receiver under limited operations.



Assumptions of the Snyder Filter. This report assumes that the point object is within the field-of-view of the optical receiver and is imaged as a single spot on the photodetector array. In other words, the tracker has acquired the target and, hence, the tracker is said to be in "fine-tracking" mode. As mentioned previously, the solution of estimating the position of maximum intensity based on released photoelectrons is the Snyder Filter. For this research, the Snyder Filter is implemented in open-loop configuration (i.e., no control or feedback input). The Snyder Filter models the spot as having a Gaussian-shaped intensity profile and the spot drifts dynamically as a First Order Gauss-Markov process. These characteristics and the Snyder Filter are discussed in detail in the next chapter.

In addition to the above assumptions, this estimator assumes its measurements are from a photodetector array capable of measuring the "exact" temporal and spatial component of the photoelectron. This idealization places a limit in tracking capabilities which can be accomplished with photodetectors arrays of finite resolution, such as a quadrant photomultiplier. However, the Snyder Filter assumes that its measurement data contain no extraneous (or noise) measurements. That is, photoelectrons are not released due to background radiation or dark current. This report investigates the tracking performance of the Snyder Filter based on observations of the sensed photoelectrons as input data.

## Problem

The problem is to establish the performance capabilities of the Snyder Filter. In this case, the issue is whether this minimum mean-square-error estimator commits errors small enough to yield good tracking. Thus, the problem is to describe the error performance of the Snyder Filter in order to make this evaluation. Once the performance description is established (under the assumptions of no background or dark current), an additional objective is to determine the sensitivity of the Snyder Filter when noise data is presented to the filter as input. To improve filter performance in the presence of the above disturbances, ad hoc methods which alter the filter structure will be investigated.

## Overview and Approach

Chapter II describes the models employed in the tracking scheme and establishes conditions in tracking performance under which the Snyder Filter is evaluated. The chapter begins by describing the model of the direct detection optical receiver and its detection process. In this section, the semiclassical approach is used to describe the photodetection process. The results of this analysis are used to derive the statistics of the output process from the optical receiver (Appendix A). Following this discussion is a description of the detector noise which affects the output of the receiver.

Following the model of the optical receiver is a section on the Snyder Filter. A characterization of the spot's

intensity profile and its dynamics are given. Following the subsection is a portrayal of position-sensitive measurements available to the Snyder Filter. As noted earlier, these measurements consist of point process photoconversions in time and space. Concluding the section are the filter equations of the Snyder Filter.

Chapter II finally concludes with a description of performance parameters to describe the mean-square-error (MSE) of the Snyder Filter. In this case, performance descriptions of estimators and controllers that employ point process observations in time and space are available in recent literature (Ref. 4). However, this report addresses only the estimation performance of the Snyder Filter. Also, the Snyder Filter is a minimum mean-square-error (MMSE) estimator, under ideal conditions (i.e., input data from background radiation or dark current are not included). The MSE, also denoted as  $E[P(t)]$ , is used to determine whether the errors committed by the Snyder Filter are sufficiently small for tracking purposes. However, the MSE cannot be evaluated in closed form; thus, upper and lower bounds are derived rather than solving for MSE. In Appendix B, the models and conditions of the Snyder Filter are applied in the upper and lower bounds.

In the appendix, two physically motivated parameters are defined from these bounds to establish conditions under which the Snyder Filter yields good tracking: the average number of photoelectrons in a coherence time of the spot's dynamics and the mean square value of the spot's jitter

normalized to the square of the beamwidth. These parameters establish regions of operations where the upper and lower bounds converge to the actual MSE (i.e., bounds are identical). The parameters are discussed in detail at the end of Chapter II. Note that the performance measures themselves assume perfect data; that is, these measures of performance are not valid for cases which include data from dark current and background radiation.

To demonstrate the tracking performance provided by the above parameters and to determine the filter's sensitivity to noise measurements, a Monte Carlo simulation and performance analysis is performed on a digital computer. Chapter III develops algorithms to simulate the models in the computer required to perform this study. The chapter begins with a section on simulating the spot's dynamics on the detector surface and the required noise generators are discussed next. Following these sections are time-space point process generators. Two methods are used to generate these data measurements: one, the Binomial Method, uses the incremental definition of the point-process, and the other, the Conditional Method, involves Bayes' rule and the statistics of the output of the optical receiver. The Binomial Method involves a threshold test to declare an event (photoconversion) at each infinitesimal area on the detector surface. The Conditional Method calls a uniform random variable distributed between zero and one from the computer system and transforms it into another random variable with a desired probability distribution. This transformed variable is a



realization of either the time or space coordinates associated with the photoconversion process. After describing these two methods, the theoretical and practical aspects of implementing each method in the computer are discussed. Concluding Chapter III is the performance analysis which characterizes the error process generated by the Snyder Filter. Given in this section are the sample statistics, plots, and test cases required to evaluate filter performance. Assuming perfect measurements (i.e., no background or dark current events), the actual performance of the Snyder Filter is compared with the upper and lower bounds on MSE. This analysis should indicate where the actual performance lies with respect to the bounds. Then noise measurements are included in the analysis to determine the filter sensitivity to these measurements. Finally, ad hoc methods of residual monitoring and filter tuning are employed to enhance tracking performance in the presence of the noise measurements.

Chapter IV contains results from the simulation. For perfect measurements, the simulation results indicate the usefulness of the bounds in describing the actual performance of the Snyder Filter. Also, these results show for low signal events per coherence time that the upper bound describes the actual performance. When measurements from background radiation or dark current are included in the simulation, the estimator was found to be quite sensitive to these noise measurements, resulting in very poor tracking. Finally, it was found that

tracking performance can be improved substantially by an ad hoc procedure called residual monitoring.

The last chapter is a summary of conclusions and recommendations for further research.

## II. The Snyder Filter and Its Open Loop Estimation Performance

The Snyder Filter is a recursive data processing algorithm. This algorithm employs point process observations in time and space to estimate optimally the position of maximum intensity on a detector array of infinitesimally fine partition. However, its estimate is only as good as the model describing the output statistics of the photodetector array (the key component in the optical receiver). Therefore, the model of the direct detection optical receiver and its detection process deserves description. The modelling will involve a statistical description of the receiver's output. Following the receiver model, the Snyder Filter is discussed. Concluding the chapter is the tracking performance by which this estimator is to be judged using upper and lower bounds on MSE. For this case, two parameters are defined to describe the actual performance of the Snyder Filter. The concepts are presented in one spatial dimension.

### Optical Receiver Model

There are two classes of optical receivers, direct detection receivers and heterodyning receivers. The difference between these two receivers is that the former operates to detect the instantaneous power in the collected field at receiver's input and the latter operates to detect a combined field formed by mixing a locally generated field with the received field. This study is concerned with direct

detection receivers.

General Description. The direct detection receiver is also known as a noncoherent detector which is shown in Fig. 2. The receiver consists of a lens system and a photodetector. The lens system, also referred to as the front end of the receiver, performs two functions. One is to focus the optical field onto the photodetector surface at a focal point. Another function is to provide some degree of reducing the intensity of the background noise (i.e., radiation from the sun or sky) prior to photodetection. The photodetector then converts the incident field into an electrical signal.

Photodetectors. Photodetectors consist of two types: photon and thermal detectors. Because thermal detectors have a slower response for the frequencies of interest, they are not considered further (Ref. 5:87). On the other hand, photon or quantum detectors respond quickly at the optical frequencies. An excellent discussion on quantum detectors, their description, performance, and characteristics, is given in Refs. 5:87 and 6:298 . However, of all the available types of detectors using photosensitive materials, all behave according to quantum-mechanical principles (Ref. 2:6). Figure 3 portrays the photodetector model. These detectors use photosensitive materials to produce electrical signals in response to changes in the input field intensity. The signals are electrons, released from the photodetector surface, and they are collected at the anode by an electric field. This collection and movement



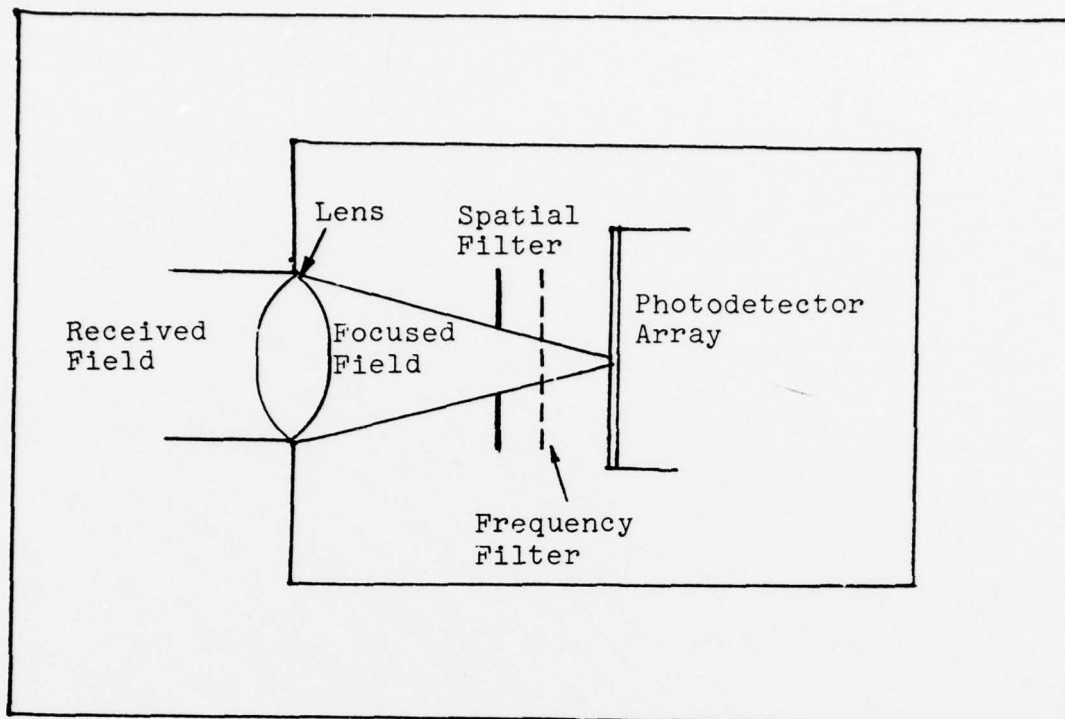


Figure 2. Direct Detection Optical Receiver  
(copied from Ref. 2:5)

of charge at the anode creates an output current. Because the conversion of optical field to electron flow and the arrival times of electrons at the anode are probabilistic, the observed output current is a random process in time and space (Ref. 2:39). This fact is true even if the input field is deterministic. In short, the detection operation inherently induces a randomness in the detector output.

To model the relationship between the optical field and the number of photoelectrons released involves a treatment in quantum mechanics (Ref. 3). This treatment has two approaches to describe the above phenomenon. One is to describe the field as a collection of discrete packets of energy called photons. Here, each photon produces an electron

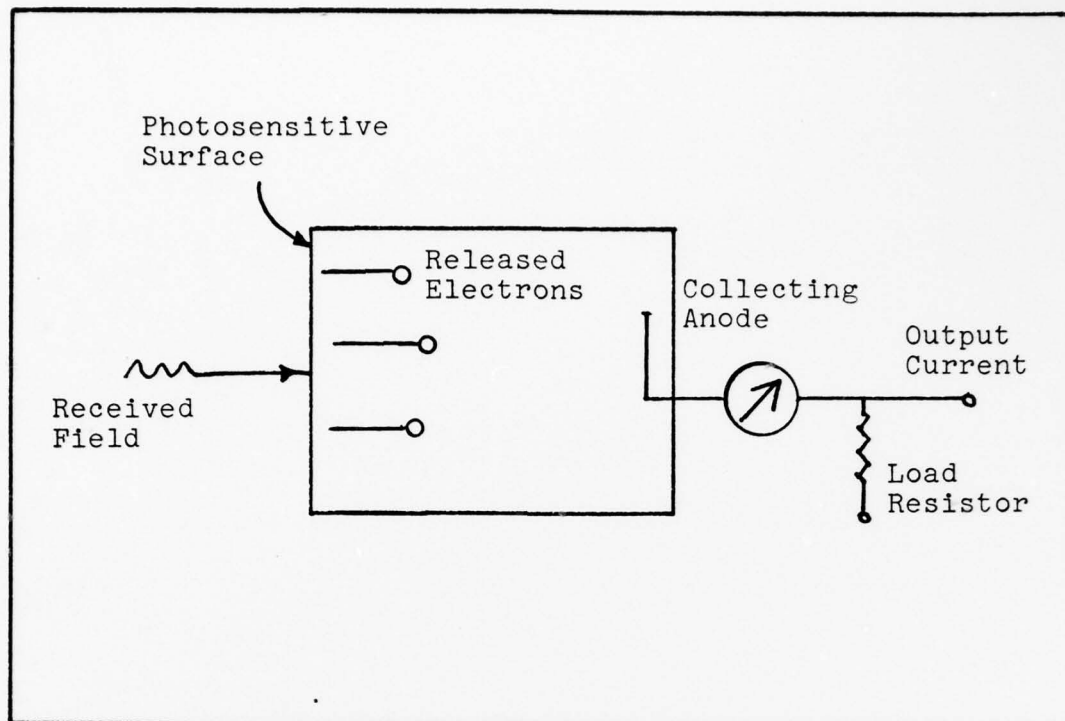


Figure 3. Photodetector Model  
(copied from Ref. 2:38)

at the detector surface with a given probability. This probability of conversion is termed the quantum efficiency,  $\eta$ . The second method, referred to as a semiclassical analysis (a direct result of quantum-mechanical considerations), treats the focussed field as a wave, and it incorporates a statistical relation to describe the interaction between the optical wave and the detector surface. The second method is preferred for its simplicity and the added insight it provides. An outline of the second approach is found in Ref. 2 and a detailed description is given in Ref. 7. Since a detailed description of the semiclassical analysis is quite lengthy, only results of this semiclassical approach are given. These results are

as follows: in a short infinitesimal time interval,  $\Delta t$ , the release of an electron from an atom at a differential length  $\Delta l$  on the detector is proportional to the field intensity over the observation area,  $\Delta l \Delta t$ . That is,

$$P \left[ \begin{array}{l} \text{one electron released} \\ \text{in a length } \Delta l \text{ during} \\ \text{the time } \Delta t \end{array} \right] \underset{\Delta l \Delta t \rightarrow 0}{\approx} \gamma I(t, r) \Delta t \Delta l \quad (1)$$

where  $P[.]$  denotes probability of,  $\gamma$  is a proportionality constant,  $I(t, r)$  denotes the field intensity at time  $t$  and point  $r$  on the detector surface, and  $\Delta l$  is located at  $r$ . Other results from this approach are as follows:

$$P \left[ \begin{array}{l} \text{no electrons released} \\ \text{from } \Delta l \text{ during } \Delta t \end{array} \right] \underset{\Delta l \Delta t \rightarrow 0}{\approx} 1 - \gamma I(t, r) \Delta t \Delta l \quad (2)$$

$$P \left[ \begin{array}{l} \text{more than one electron} \\ \text{released from } \Delta l \\ \text{during } \Delta t \end{array} \right] \underset{\Delta l \Delta t \rightarrow 0}{\approx} 0 \quad (3)$$

Along with these results is an assumption that the release of electrons from disjoint observation areas  $\Delta t \Delta l$  are treated as independent events. This assumption and Eqs (1) through (3) mathematically model the photodetecting surface.

Detector Noise. With no noise sources, the output current is given by

$$i(t, r) = q \sum_{k=1}^n \delta(t - t_k) \delta(r - r_k) \quad (4)$$

where  $q$  is the electronic charge,  $t_k$  is the  $k^{\text{th}}$  event arrival time,  $r_k$  is the corresponding event location,  $r$  denotes a position on the detector surface,  $n$  is the number of events in an observation area, and  $\delta(t)$  and  $\delta(r)$  are delta functions. Eq. (4) assumes that the detector has infinite bandwidth (e.g., a photomultiplier or avalanche photodiode fits closely to this description). The relation also indicates that the current is a random process since  $n$ ,  $t_k$ , and  $r_k$  are random variables.

However, the imperfection of the optical receiver and background radiation also affect the output current. In general, the output current from the photodetector array at  $(t, r)$  can be represented as

$$i(t, r) = i_s(t, r) + i_b(t, r) + i_d(t, r) + i_{th}(t, r) \quad (5)$$

where  $i_s(t, r)$  is due to signal current,  $i_b(t, r)$  is current due to background noise,  $i_d(t, r)$  is due to dark current, and  $i_{th}(t, r)$  is current due to thermal noise. The dark current is a result of current flowing in absence of photoexcitation. Also, the dark current is well modelled as a point process (Ref. 5:148) with a rate function that is constant (i.e.,  $\lambda_d(t, r) = \lambda_d$  is termed homogeneous (Ref. 3:54)). Further, the background noise can be associated with a point process in nighttime operation, and its rate function is homogeneous provided that three conditions are satisfied: (1) background electric field has zero mean, (2) background intensity is constant, and (3) the product between the ensemble average

of the number of electrons,  $n_b$ , and the bandwidth of the background radiation,  $\frac{1}{\tau_b}$ , is much less than 1. The last condition,  $n_b \tau_b \ll 1$ , is known as low photon coherence which is a valid approximation for nighttime operation. For convenience, the dark current in this study will be the combined effects due to the detector dark current and due to background radiation. Finally, the thermal or Johnson noise current  $i_{th}(t,r)$  is caused by thermal fluctuations of electrons in a resistor. It is modelled as a white Gaussian random process (Ref. 5:145).

To describe the output current in Eq. (5) statistically is very difficult. It is difficult because the output current is a mixed process (i.e., a sum of a discrete process (Point-Process model) and a continuous process (Gaussian model)). Hence, limiting cases must be considered. This study will ignore the current due to thermal noise since one of the objectives of this study is to observe the quantum effects of dark current in filter performance. Also, if the detector is a photomultiplier or avalanche photodiode with high gain, one can assume for low input intensity that the optical receiver is operating in the point process regime, and thus, thermal noise is ignored.

Photodetector Statistics. It is assumed in the detector model that the electrons arriving at the anode of each detector of an array are independent. Then the output statistics of each detector can be treated independently of one another. One needs the statistics describing the number of events,  $n$ , the ordered event times,  $t_k$ 's, and, ordered event locations,



$r_k$ 's, to characterize the detector output completely. Thus, the joint density of these variables is needed. With the results given in Eqs. (1) through (3), the above joint density of the photodetector can be derived. Before stating the results, it is convenient to define a complex envelope which characterizes (in part) the focussed or received field (i.e., a classical description). Let  $u(t,r)$  denote the scalar optical field. Then the complex envelope  $U(t,r)$  of the scalar field is defined implicitly as

$$u(t,r) = \text{Re}(U(t,r)e^{j2\pi f_0 t}) \quad (6)$$

where  $R(\cdot)$  denotes the "real part of" the quantity in parenthesis, and  $f_0$  denotes the carrier frequency. The intensity of the field is represented as

$$I(t,r) = \frac{1}{2} \frac{1}{Z_m} |U(t,r)|^2 \quad (7)$$

where  $|\cdot|$  denotes the modulus of the complex field, and  $Z_m$  denotes the impedance of the medium (Ref. 2:10).

With the definition of a complex envelope and using Eqs. (6) and (7), the output of the photodetector, conditioned on knowing the optical field, can be modelled as a point process (Ref. 2) with rate function (in one dimension)

$$\lambda(t,r) = \underbrace{\frac{n}{hf_0} \int_{\mathcal{A}} |U(t,r)|^2 d\mathcal{A}}_{\text{due to signal}} + \underbrace{\lambda_d}_{\text{due to dark current}} \quad (8)$$

$(\lambda_d(t,r) = \lambda_d)$

where  $n$  is quantum efficiency,  $h$  is Planck's constant,  $f_0$  is the optical signal frequency,  $U_s(t,r)$  is the complex envelope of the scalar field incident on the detector surface at  $(t,r)$ ,  $l$  is the length of detector array, and  $dl$  is the differential detector length. The integral in Eq. (8) represents the total optical power deposited by the beam on the detector surface and the energy of a photon is  $hf_0$ . Also, recall from the previous section that the homogeneous dark rate function is due to the combined effects of background radiation (of zero mean electric field) satisfying low photon coherence and dark current resulting from imperfection of the photodetector. This dark rate function, denoted as  $\lambda_d$ , which is assumed to be independent in time and space can be expressed as

$$\lambda_d = \underbrace{\frac{n}{hf_0} \int_l E [ |U_b(t,r)|^2 ] dl}_{\text{due to background radiation}} + \underbrace{\lambda_d'}_{\text{due to photodetector}} \quad (9)$$

Note that in Eq. (8) and (9) the optical receiver assumes to be operating at the point-process regime. Also, the first term at the right-hand side of Eq. (9) is a constant rate function, since this study assumes a constant background intensity. In other words, the dark current,  $\lambda_d$ , is independent of time and space. Finally with Eqs. (1) through (3), the output statistics of the optical receiver conditioned on knowing the input field is found in Appendix A as

$$f[\{t_k\}, \{r_k\}, n] = \exp(-\int_{\ell} \int_0^T \lambda(\alpha, \beta) d\alpha d\beta) \prod_{k=1}^n \lambda(t_k, r_k) \quad (10)$$

where  $\{t_k\}$  denotes set of ordered event times,  $\{r_k\}$  denotes the corresponding set of event locations,  $\ell$  is detector length,  $n$  is the number of events in a time interval  $[0, T]$  on  $\ell$ . Again, this joint density completely characterizes the statistical output of the optical receiver.

### The Snyder Filter

The previous sections described the statistical model of the optical receiver which is used in the optical tracking problem. The lens system of a receiver focusses the received field on a detector surface at the focal plane. The array of detectors responds to the received field which arrives at various angles at the receiver. Because of random disturbances, the spot wanders randomly on the detector plane. Electrons are released at a rate proportional to the light intensity, given by Eq. (8). For the model upon which the Snyder Filter is based,  $\lambda_d$  is assumed to equal zero. The Snyder Filter estimates the position of maximum intensity on the detector plane in terms of these time-space photoelectrons. An outline of its models and results will now follow specializing for one spatial dimension.

Characterization of Spot. The spot of light on the detector surface is a diffraction pattern focussed by the receiver's lens. It is assumed that the spot of light has a Gaussian-intensity profile given by



$$I(r, \underline{x}(t), t) = I_0(t) \exp\left[-\frac{1}{2}\left(\frac{r - \underline{x}(t)}{\sigma(t)}\right)^2\right] \quad (11)$$

where  $I_0(t)$  is the maximum intensity,  $\sigma(t)$  characterizes the beam spread, and  $\underline{x}(t)$  is the true location of the spot (i.e., the location at the centroid of the beam). For this study,  $I_0(t)$  and  $\sigma(t)$  are assumed to be static (i.e.,  $I_0(t) = I_0$  and  $\sigma(t) = \sigma$ ). Figure 4 portrays this intensity profile. From the figure, the beam width (or beam radius) in this study is defined as a point from the maximum intensity,  $I_0$ , to a point in which the intensity is reduced to  $I_0 e^{-1/2}$ , or about 60.7% of the maximum intensity.

Characterization of Spot's Motion. The motion of the spot's centroid is assumed to be modelled by the following linear stochastic differential equation

$$d\underline{x}(t) = F(t)\underline{x}(t) + G(t)d\beta(t); \underline{x}(t_0) = \underline{x}_0 \quad (12)$$

where  $\beta(t)$ ,  $t \geq 0$  is a standard Wiener process,  $F(t)$  is the state coefficient, and  $G(t)$  is the noise input coefficient. The spot's dynamics are governed by a number of disturbances. The atmosphere is one such disturbance; characterized as an inhomogeneous random optical channel (Ref. 9:16-26), the atmosphere changes its index of refraction due to temperature variation. Because of the stochastic nature of the atmosphere, and frequency at which the field propagates, the optical wave interacts with the foreign particles in the atmosphere. One consequence of this phenomenon is that the received field causes variations in the beam's arrival angle, causing the spot to move randomly on the detector plane. Platform

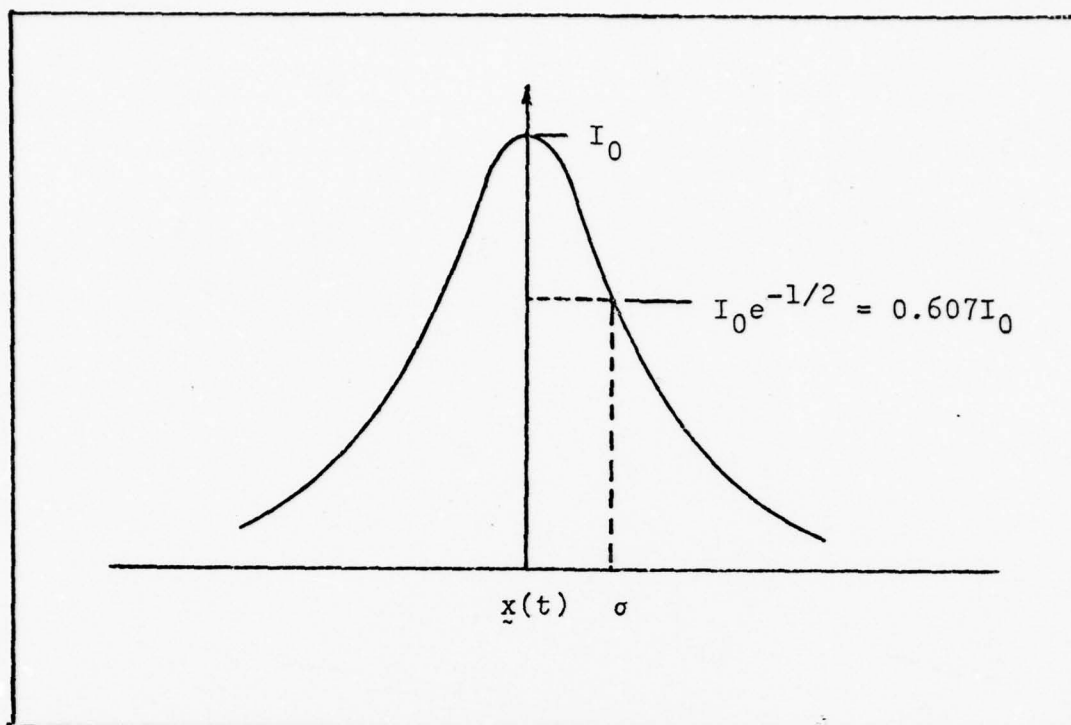


Figure 4. Intensity Profile of Spot  
in One-Dimension

vibration of the optical receiver is another disturbance which causes the spot to drift. The important point is that any relative motion between object and receiver due to other effects will result in the spot to drift dynamically on the detector plane. However, it is not the purpose of this study to model accurately the motion of the spot, but to provide a reasonable and simple model for digital simulation. A model was developed to describe the dynamics of the target relative to the receiver (Ref. 10:42). This model is a stationary First Order Gauss-Markov process, the output of a first order lag driven by white Gaussian noise of zero mean. This process also describes a variety of phenomena having bandlimited characteristics. Thus, this model will be used to describe the

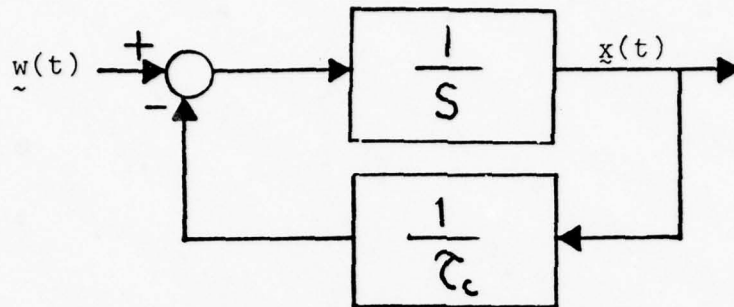
dynamics of the spot. Another name for this process is an exponentially time-correlated Gaussian process. Figure 5 portrays the properties of a First Order Markov Process. Two parameters of interest to describe the output of the first order lag are the coherence time  $\tau_c$ , and its mean squared value  $\sigma_x^2$ . The coherence time (or correlation time), describes how fast the resulting output process,  $\underline{x}(t)$ , will vary in time. The reciprocal of  $\tau_c$  is viewed as the bandwidth of the disturbance process (i.e., turbulence plus other effects). Heuristically, the spot's rms value of random displacements (or spot's rms jitter), is a measure of how much the spot will fluctuate about its mean position on the detector array. Finally, the strength of a white Gaussian noise driving the first order lag is given as

$$E[\underline{w}(t)\underline{w}(t+\tau)] = Q\delta(\tau) \quad (13)$$

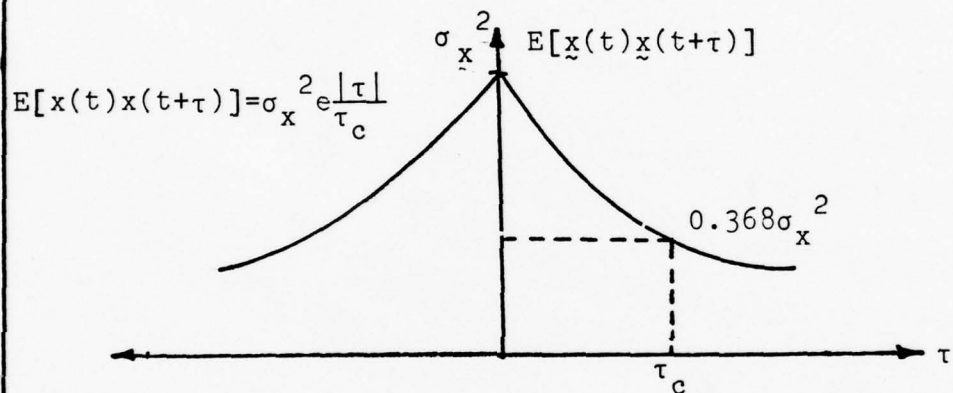
where  $Q = \frac{2}{\tau_c} \sigma_x^2$  (Ref. 9:4.77). The strength,  $Q$ , describes how fast the Wiener Process or Brownian Motion,  $\underline{\beta}(t)$ , diverges in mean square value from its initial condition of zero (Ref. 9:4.29).

Position-Sensitive Measurements. As mentioned earlier in the report, these measurements consist of event locations which provide information about the position of maximum intensity. Assuming no dark current, the conversion rate at the detector surface is modelled as

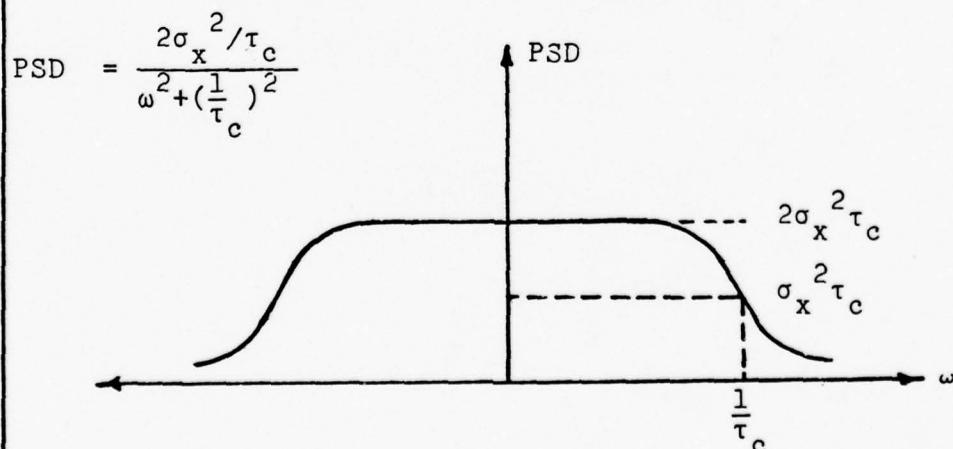
$\tilde{w}(t)$  white noise of zero mean



a) Shaping Filter for First Order Markov Process  $\tilde{x}(t)$



b) Autocorrelation of Output Process,  $\tilde{x}(t)$



c) Power Spectral Density (PSD) of  $\tilde{x}(t)$   
( $\omega \triangleq$  Angular Frequency)

Figure 5. Properties of a First Order Markov Process

$$\lambda_g(r, \underline{x}(t)) = \left( \frac{n I_0 \sqrt{2\pi} \sigma}{h f_0} \right) \left[ \frac{1}{\sqrt{2\pi} \sigma} \exp\left\{ \frac{-1}{2\sigma^2} (r - \underline{x}(t))^2 \right\} \right] \quad (14)$$

If the detector length is sufficiently large, the quantity in brackets,  $[\cdot]$ , in Eq. (14) integrates over the entire detector length to a value very close to one. Note that Eq. (14) is derived by substituting Eq. (11) as the signal intensity in the first term of Eq. (8). The term  $n I_0 \sqrt{2\pi} \sigma$ , represents the average optical energy deposited on the detector by the spot to release photoelectrons. The term  $h f_0$  represents the energy of a single photon, characterizing the particle nature of light of frequency  $f_0$ . Then integrating Eq. (14) both over time (with limits from 0 to T) and space (over entire detector length), yields  $\left( \frac{n I_0}{h f_0} \sqrt{2\pi} \sigma \right) T$ . This term represents the ensemble average of the number of photons detected at the output over the time-space observation area. Recall that the data measurements are obtained from a photo-detector array, capable of measuring the exact temporal and spatial component of a photoelectron. With this idealization the estimator's performance, derived in Appendix B, places a limit in performance which can be achieved with arrays of finite resolution. In other words, a decrease in spatial resolution should result in poorer performance. It is also assumed that the detector array is large such that edge effects of the spot's intensity profile, described as Gaussian-Shaped can be ignored. A good "rule of thumb" is to have the detector large such that the distance between the center of the spot



and the edge of the detector array is at least six beam widths. This is "good" because with respect to a Gaussian-shaped beam, the above "rule of thumb" closely approximates a detector of infinite length. Also, by having the detector length large, edge effects may be ignored as the spot moves dynamically even with large wanderings on the detector surface.

Snyder's Filter Equations. This subsection presents the dynamical filter equations that incorporate point-process observations to estimate the position of maximum intensity. These equations, specialized for one-dimension state as follows:

$$d\hat{x}(t) = F(t)\hat{x}(t)dt + \int_{\ell} K(t)[r-H(t)\hat{x}(t) N(dt dx d\ell)] \quad (15)$$

$$\begin{aligned} d\hat{P}(t) = & F(t)\hat{P}(t)dt + \hat{P}(t)F(t)dt + G(t)Q(t)G(t)dt \\ & - \int_{\ell} K(t)H(t)N(dt dx d\ell) \end{aligned} \quad (16)$$

$$K(t) = \hat{P}(t)H(t)[H(t)\hat{P}(t)H(t) + R(t)]^{-1} \quad (17)$$

$$\hat{x}(t_0) = 0, P(t_0) = P_0 \quad (\text{initial conditions at } t_0) \quad (18)$$

where  $\hat{x}(t)$  is the conditional estimate of the spot's centroid given the measurement data (i.e., event locations that are random in time and space),  $\hat{P}(t)$  is the conditional error variance,  $H(t)$  is the measurement coefficient,  $K(t)$  is the filter gain,  $r$  is the location of the photoconversion from a differential detector length,  $d\ell$  in the differential time,  $dt$ , and  $N(dt dx d\ell) = dN$  is the differential number of events in the differential "space-time" observation area,  $dt dx d\ell$ .

The filter equations, Eq. (15) through (18) are recursive relations, similar in form to the discrete-time measurement Kalman-Bucy Filter. They differ in that the Snyder Filter updates its estimate and uncertainty at the event times whereas the Kalman-Bucy Filter updates at predetermined times. The mean and the variance of the conditional probability density function which describes the error in the estimate of the spot's centroid are propagated forward from the time period of the  $k^{\text{th}}$  photoconversion  $t_k^+$ , to the time of the  $(k+1)^{\text{st}}$  photoconversion,  $t_{k+1}^-$ . Then the filter updates at time  $t_{k+1}$ , by processing the measurement at that time, to achieve the estimate  $\hat{x}(t_{k+1}^+)$ , where "-" denotes before measurement update and "+" denotes after measurement update

It is convenient to expand further the interpretation of the filter equations. During interarrival times between photoconversions, the filter's conditional estimate of the centroid's position  $\hat{x}(t)$ , and its error variance  $\hat{P}(t)$ , evolve in time by the following equations

$$\frac{d\hat{x}(t)}{dt} = F(t)\hat{x}(t) \quad ; \quad t_k < t \leq t_{k+1} \quad (19)$$

$$\frac{d\hat{P}}{dt} = 2F(t)\hat{P}(t) + G(t)Q(t)G(t) \quad ; \quad t_k < t \leq t_{k+1} \quad (20)$$

The above relations govern how  $\hat{x}(t)$  and its associated conditional error variance  $\hat{P}(t)$  will propagate when the filter does not observe a photoconversion. But when the filter does observe an event, via the detector array, it will update  $\hat{x}(t)$  and  $\hat{P}(t)$  after the occurrence of the event by the following update

equations:

$$\hat{P}(t_k^+) = [H(t_k)R^{-1}(t_k)H(t_k) + \hat{P}(t_k^-)]^{-1} \quad (21)$$

$$\hat{x}(t_k^+) = \hat{P}(t_k)[H(t_k)R^{-1}(t_k)r_k + \hat{P}^{-1}(t_k^-)\hat{x}(t_k^-)] \quad (22)$$

where  $t_k^+$  is the time after the occurrence of the  $k^{\text{th}}$  photoconversion,  $t_k^-$  is the time before this occurrence, and  $r_k$  is the location of photoconversion (or photoelectron). By using the matrix inversion lemma (Ref. 1), Eqs (21) and (22) may be alternatively expressed as

$$\hat{x}(t_k^+) = \hat{x}(t_k^-) + K(t_k^-)[r_k - H(t_k)\hat{x}(t_k^-)] \quad (23)$$

$$\hat{P}(t_k^+) = \hat{P}(t_k^-) - K(t_k^-)H(t_k)\hat{P}(t_k^-) \quad (24)$$

where

$$K(t_k) = \hat{P}(t_k^-)H(t_k)[H(t_k)\hat{P}(t_k^-)H(t_k) + R(t_k)]^{-1} \quad (25)$$

Eqs. (22) and (23) indicate, clearly, the recursive nature of how  $\hat{x}(t)$  and  $\hat{P}(t)$  evolve in time given the history of data measurements. In other words, the "recursive" nature of the Snyder Filter does not require all previous data measurements to be kept in storage and processed every time a photoconversion is observed. This saves computer resources which is an important consideration for filter implementation.

To summarize, the Snyder Filter is a recursive data processing algorithm, using the available information from the photoconversions to improve the accuracy of estimating

the spot's current position of maximum intensity. The Snyder Filter is a minimum mean square error estimator; it attempts to provide the best estimate possible in such a manner that the error is minimized statistically.

The next section specifies parameters where sufficient conditions are presented to provide actual mean-square-error (MSE).

#### Upper and Lower Bounds

A question should be asked whether or not the filter errors are small enough for tracking purposes. Thus, the MSE (i.e., an expectation of the conditional error variance given the data measurements over all possible histories of measurements taken), is used to make this evaluation.

Unfortunately, finding the mean-square-error cannot be evaluated in closed form. Rather than attempt to solve for the MSE, one can bound it above and below. The method involves easily precomputed upper and lower bounds ( $P_{*A}$  lower bound on MSE and  $P^*A$  upper bound on MSE).

The following is a quote from Ref. (4) in how these bounds are derived:

"The upper bounds are derived by evaluating exactly the performance of a parameterized family of suboptimum design; one of these is identified as having smaller performance than any other, thus providing a minimal upper bound within this family of suboptimum design. The lower bounds are obtained directly by calculations involving inequalities."

The above results are specialized for this open-loop problem in one dimension. Here, the upper and lower bounds are

solved in steady state (i.e.,  $\frac{dP^*}{dt} = \frac{dP}{dt} = 0$ ) and are derived in Appendix B. The solution to this steady-state estimation problem involves a quadratic equation yielding a result given as

$$\frac{P^*}{\sigma^2} = -\frac{1}{2X} \left[ -1 + (1 + 4XY)^{1/2} \right] \quad (26)$$

$$\frac{P^*}{\sigma^2} = \frac{1}{2(X+1)} \left[ (Y-1) + \{(Y-1)^2 + 4(X+1)Y\}^{1/2} \right] \quad (27)$$

where

$$X = \left( \frac{n}{hf_0} I_0 \sqrt{2\pi} \sigma \right) (1/2\tau_c) \quad (28)$$

$$Y = \frac{\sigma_x^2}{\sigma^2} \quad (29)$$

Several comments deserve mentioning with regard to Eqs. (26) through (29). The upper and lower bounds are normalized with respect to the square of the beam width. This normalization is convenient since the error in estimating the spot can be measured in terms of beam width (i.e., a performance or criterion can be established). Thus, for good tracking performance, it is desirable to have  $\frac{P^*(t)}{\sigma^2}$  and  $\frac{P^*(t)}{\sigma^2}$  small. Figures (6a-6i) are plots of the upper and lower bounds on MSE as a function of X and Y. Note the absolute magnitude and relative separation of the bounds as X and Y are varied on each of these plots. Consider Figs. 6a-6d : for a fixed Y, the bounds both decrease in magnitude and in relative



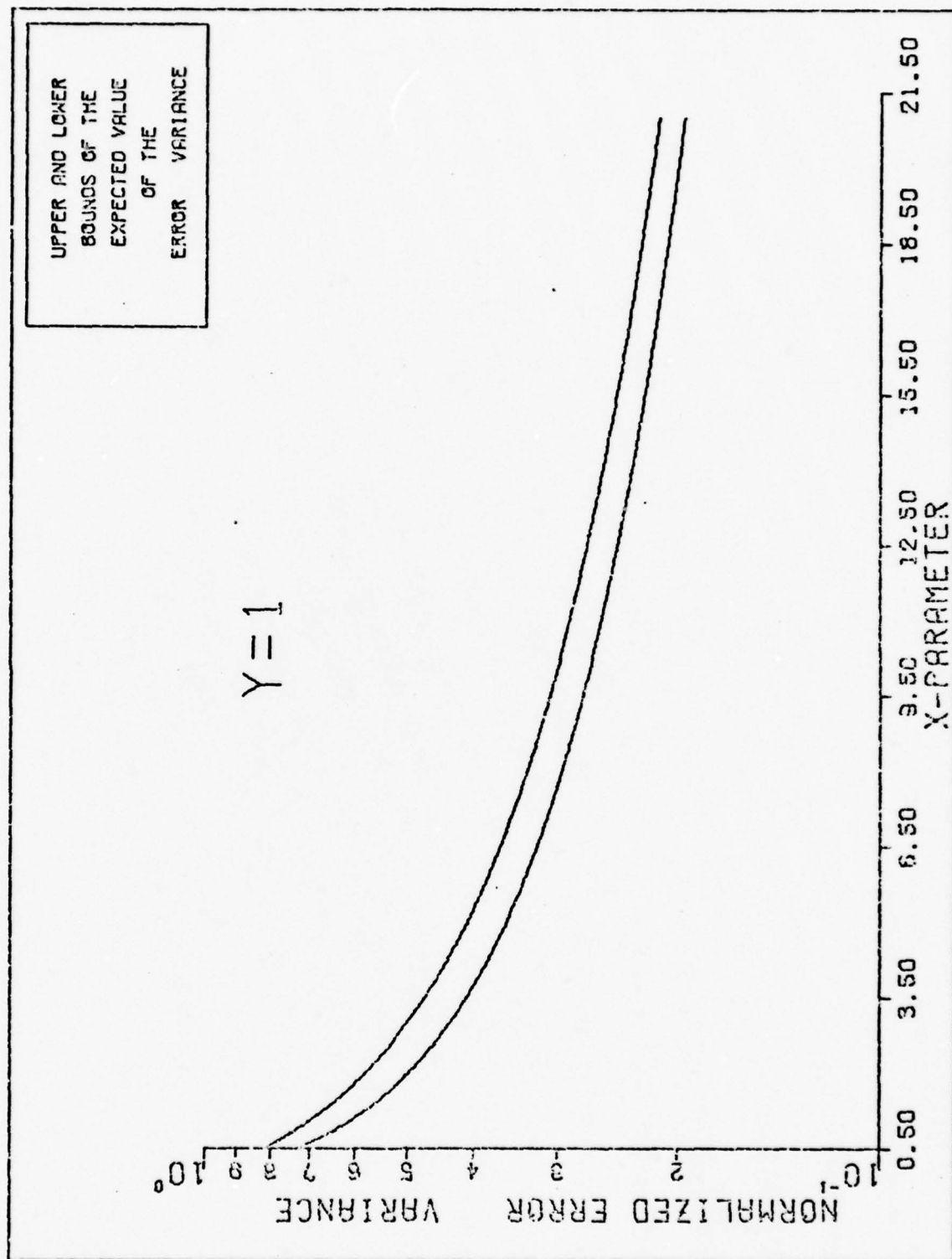


Figure 6a. Upper and Lower Bounds on MSE

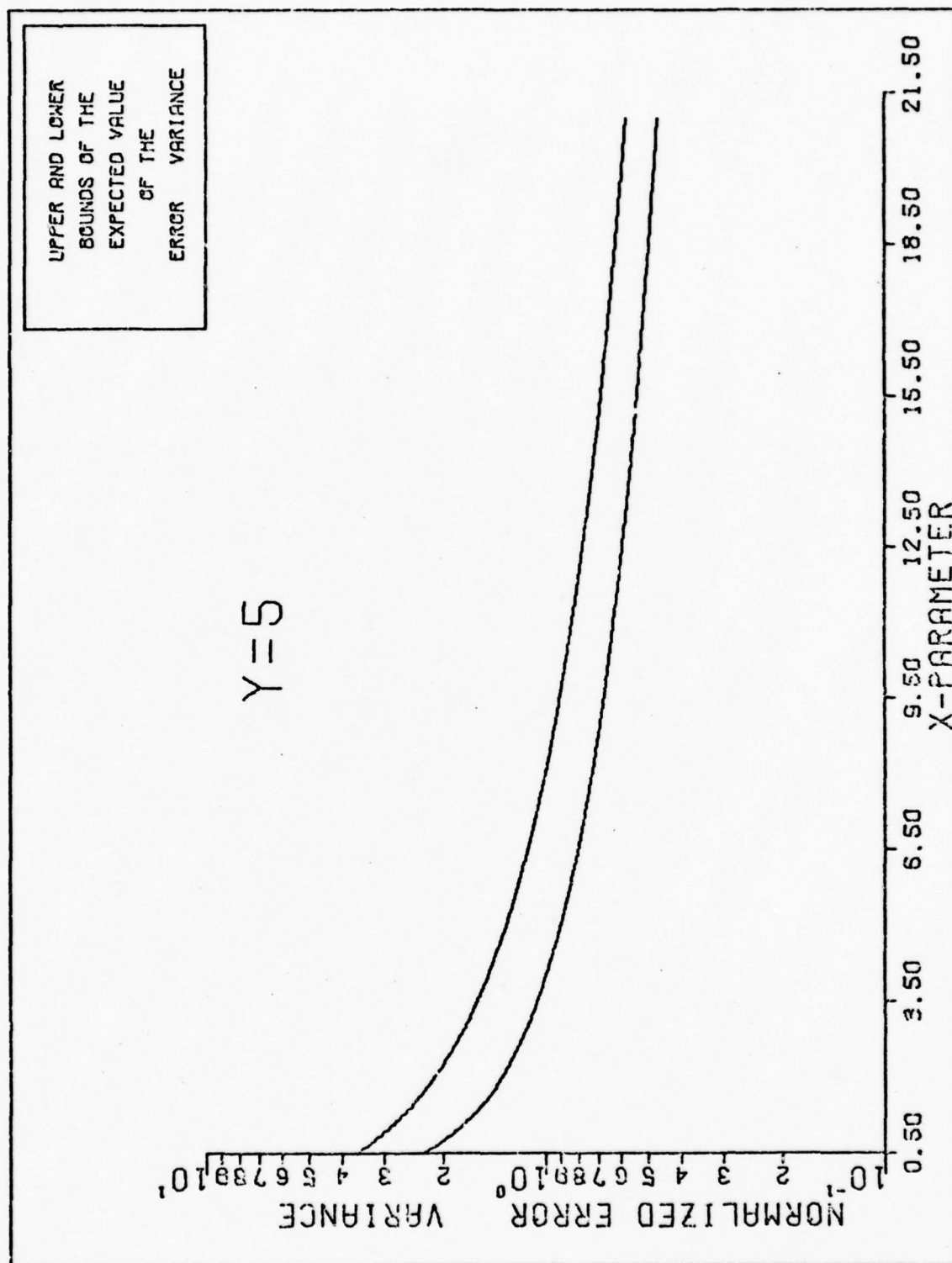


Figure 6b. Upper and Lower Bounds on MSE

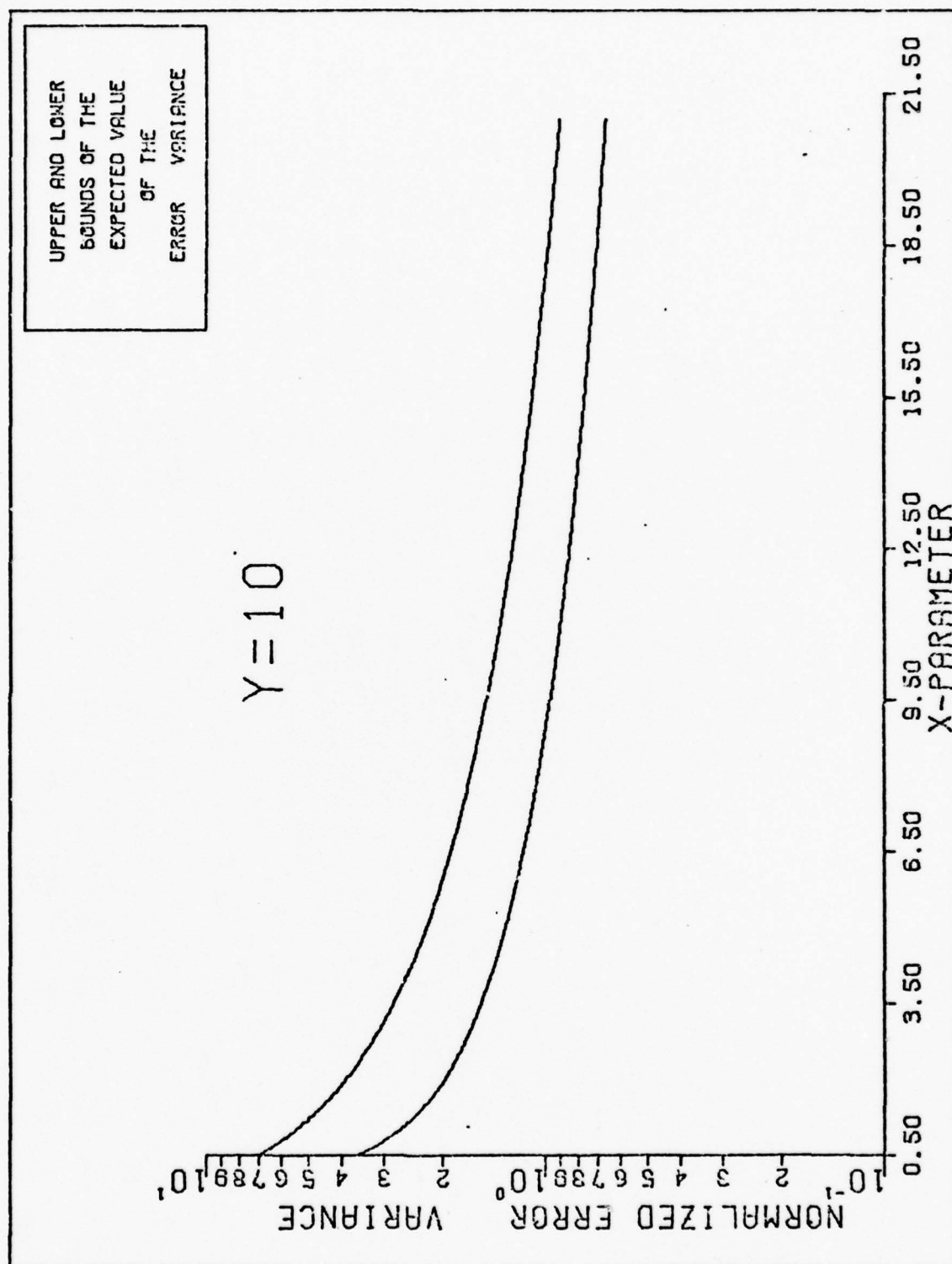


Figure 6c. Upper and Lower Bounds on MSE

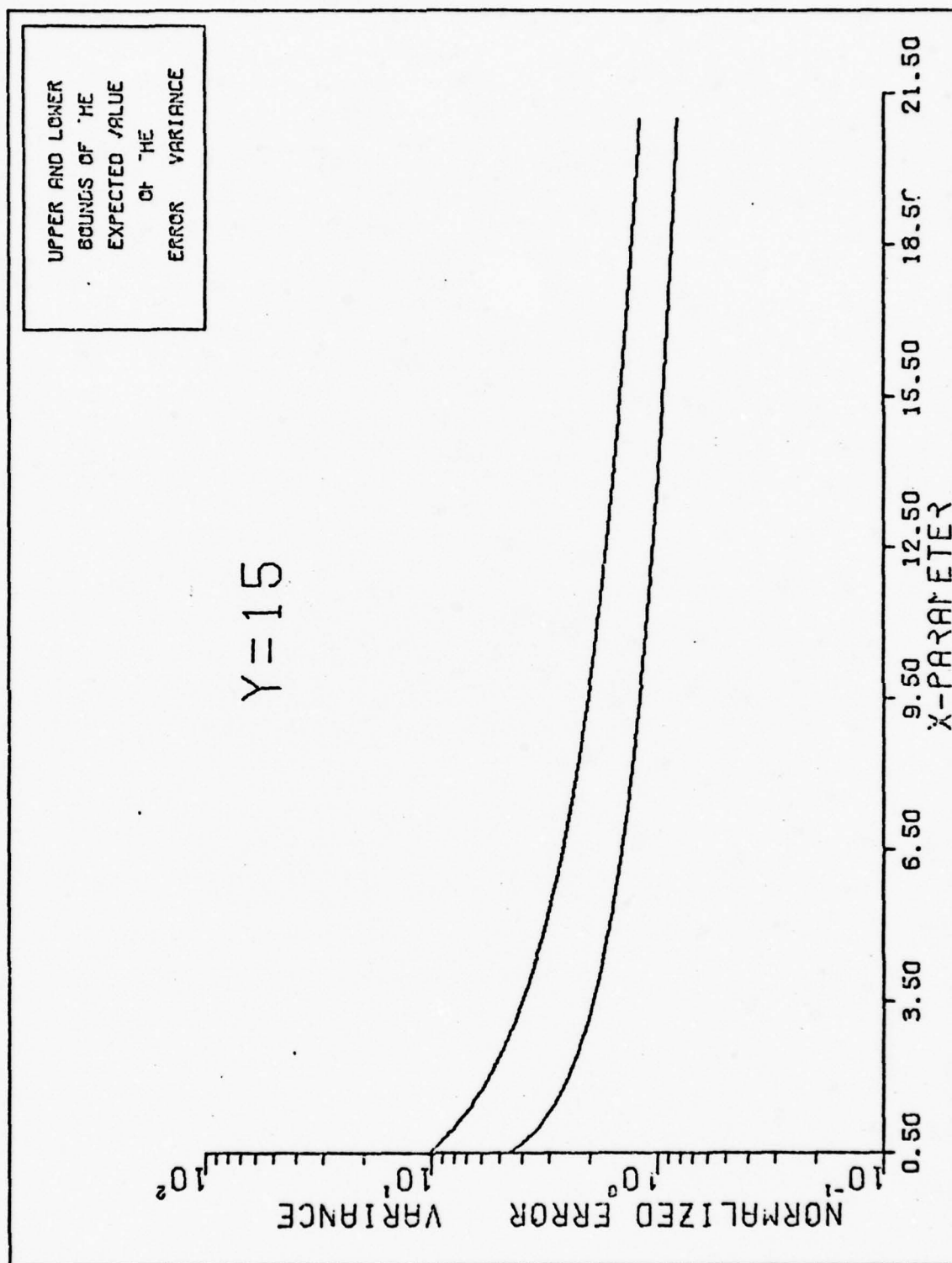


Figure 6d. Upper and Lower Bounds on MSE

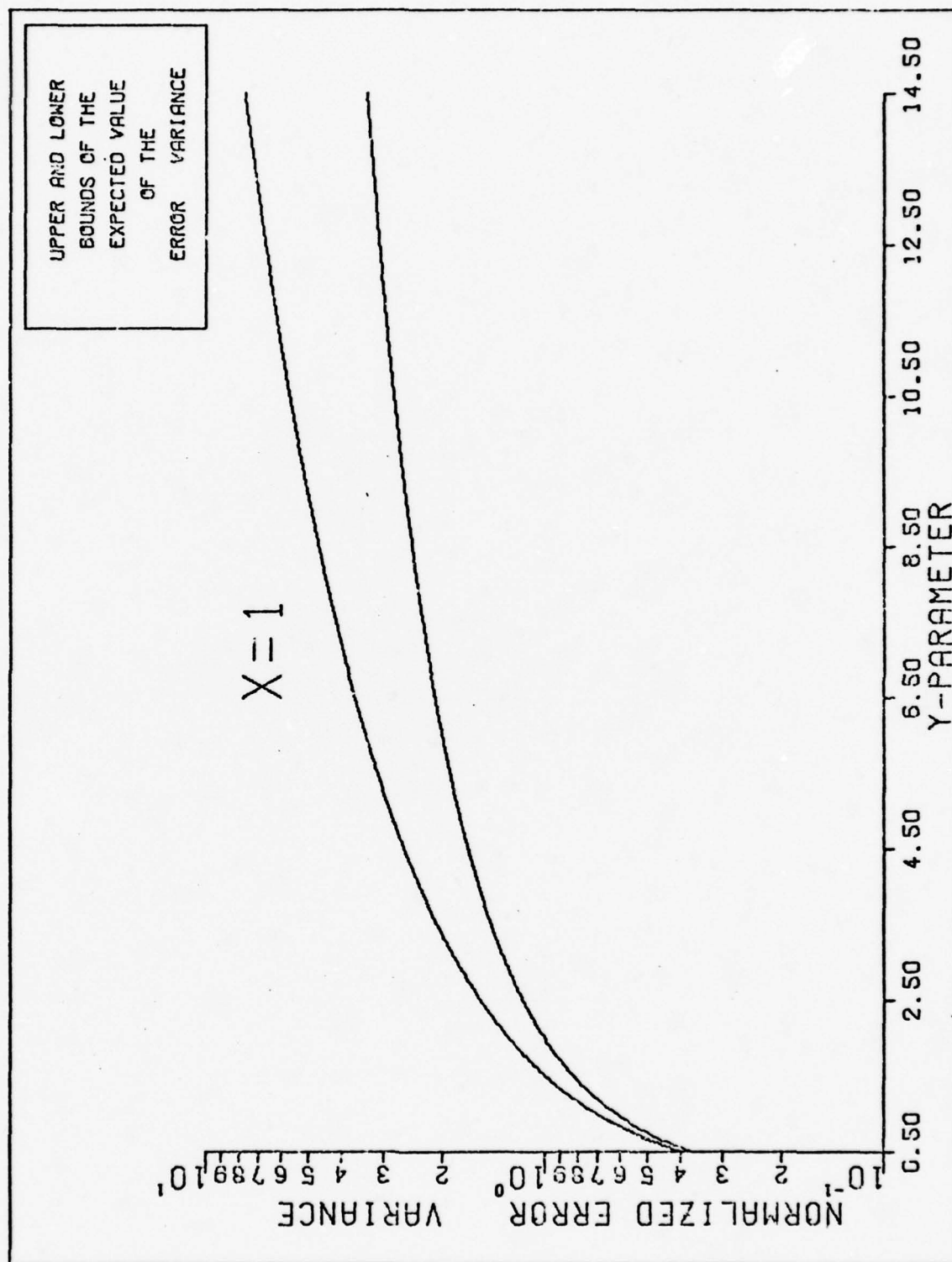


Figure 6e. Upper and Lower Bounds on MSE



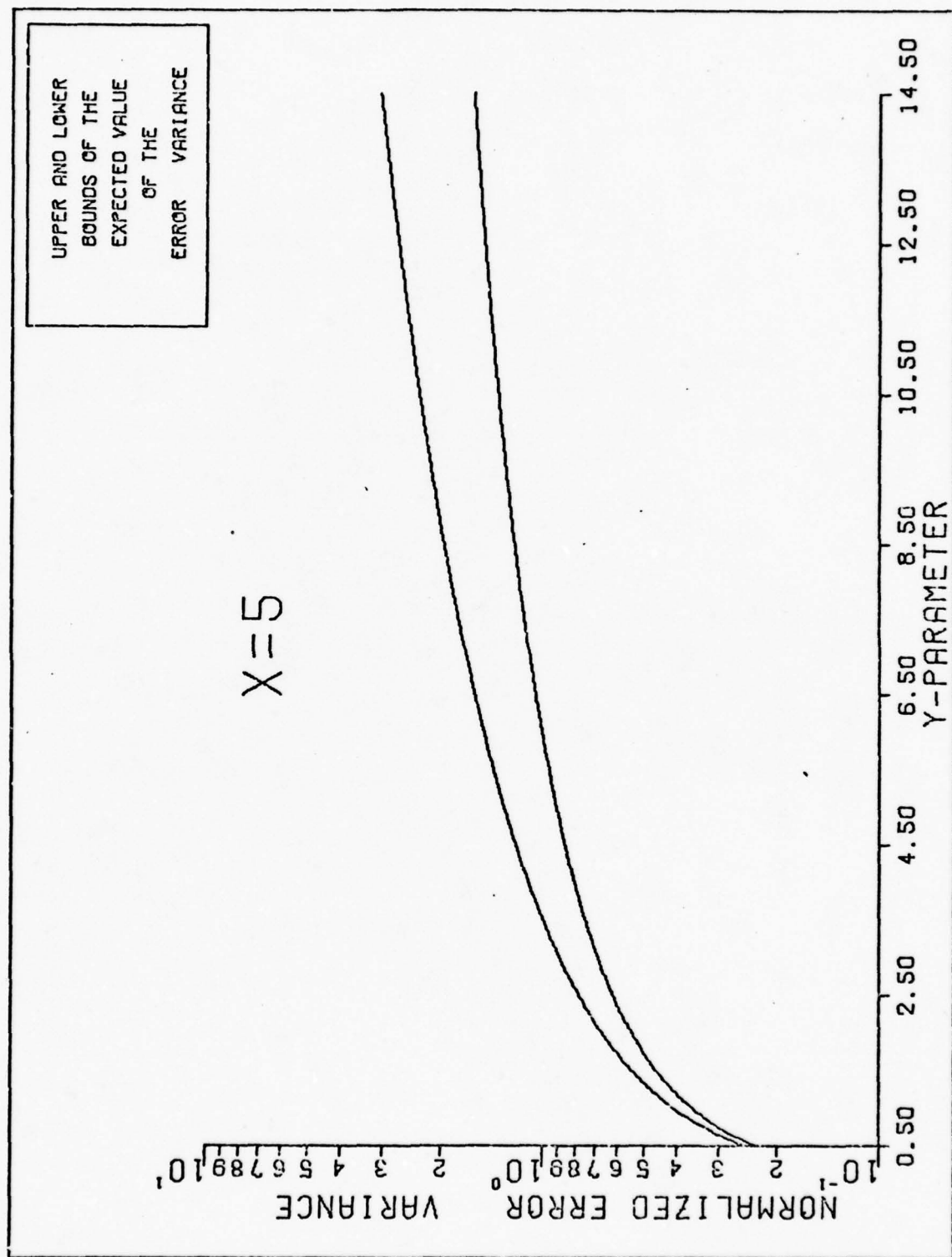


Figure 6f. Upper and Lower Bounds on MSE

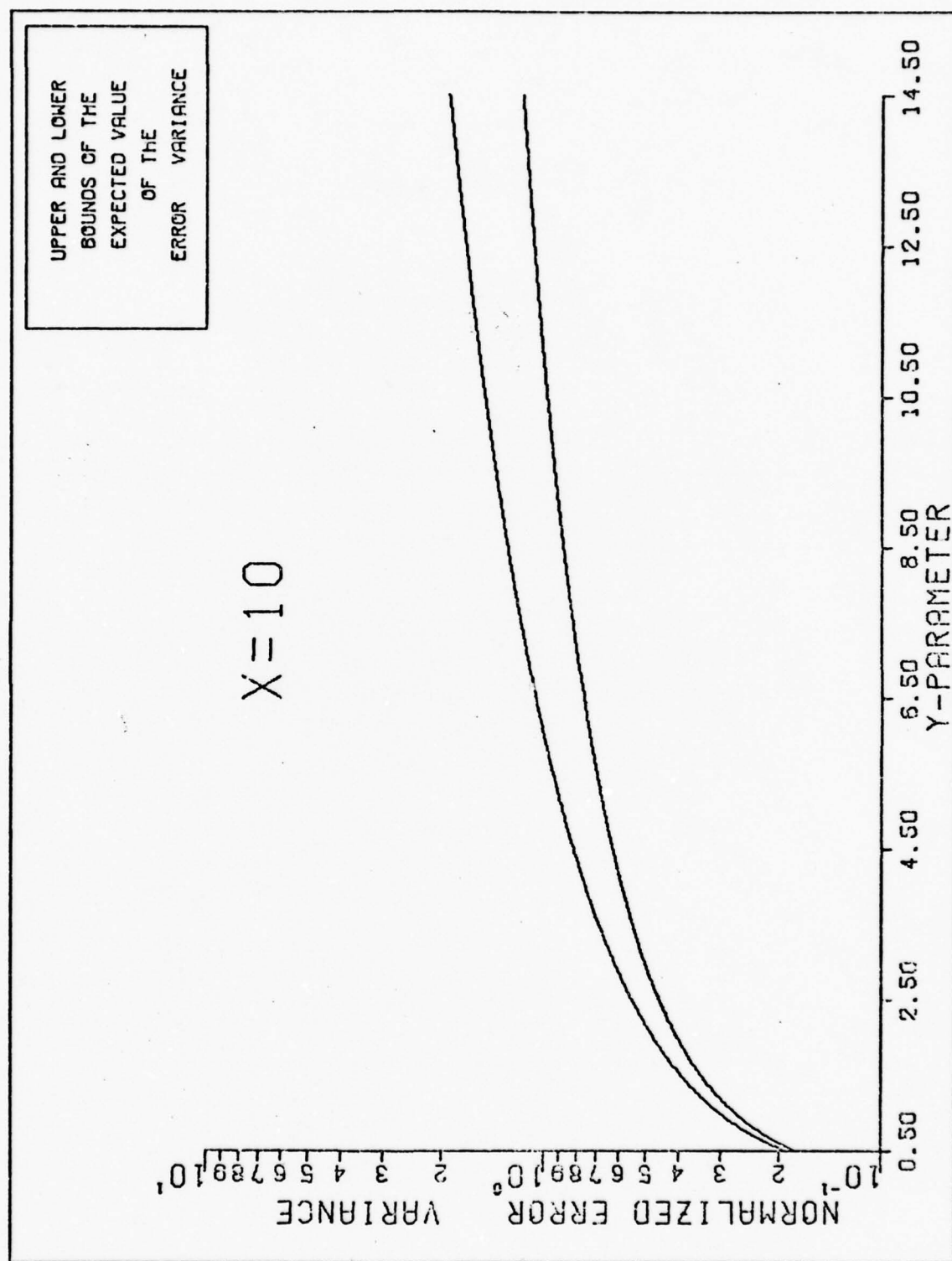


Figure 6g. Upper and Lower Bounds on MSE

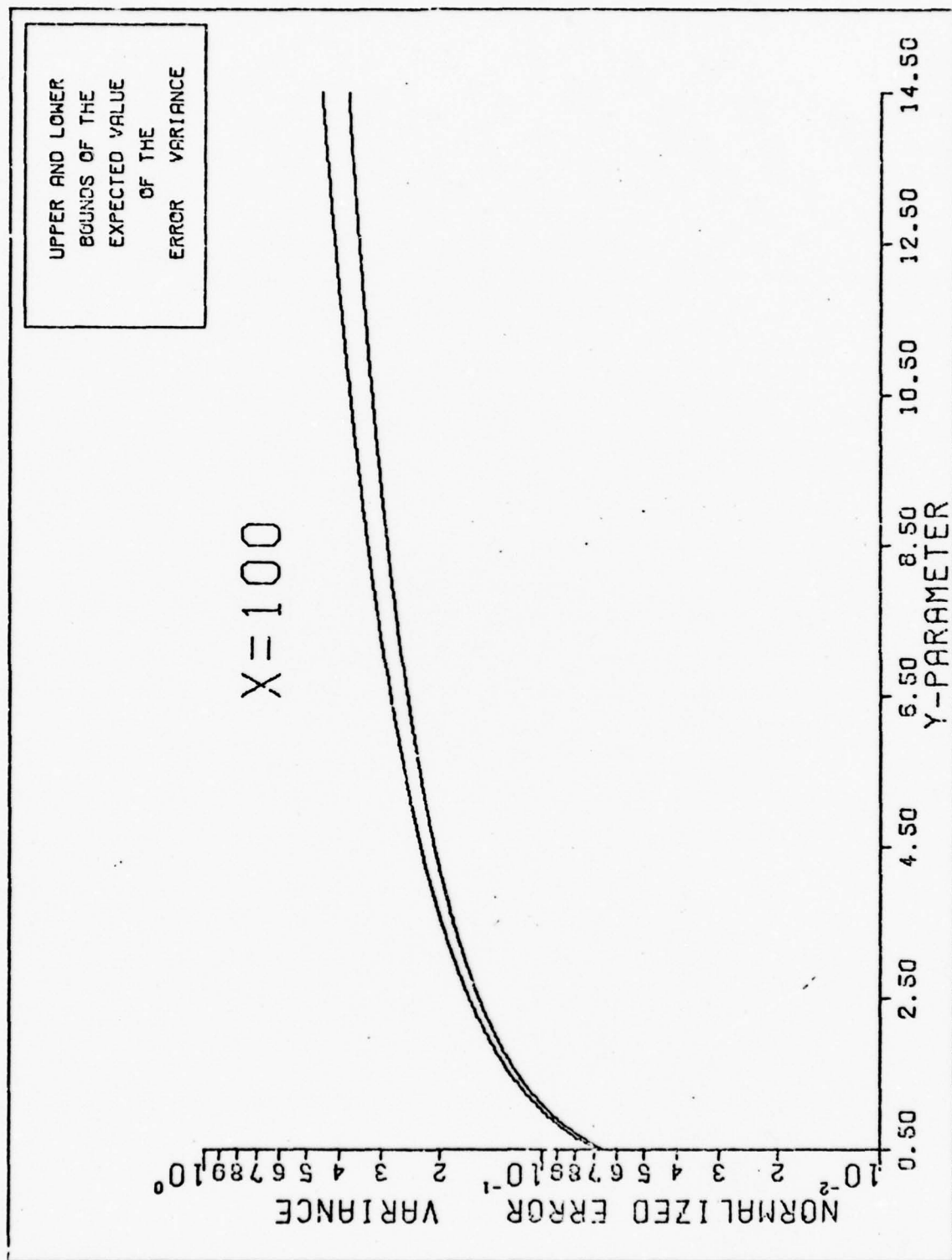


Figure 6h. Upper and Lower Bounds on MSE

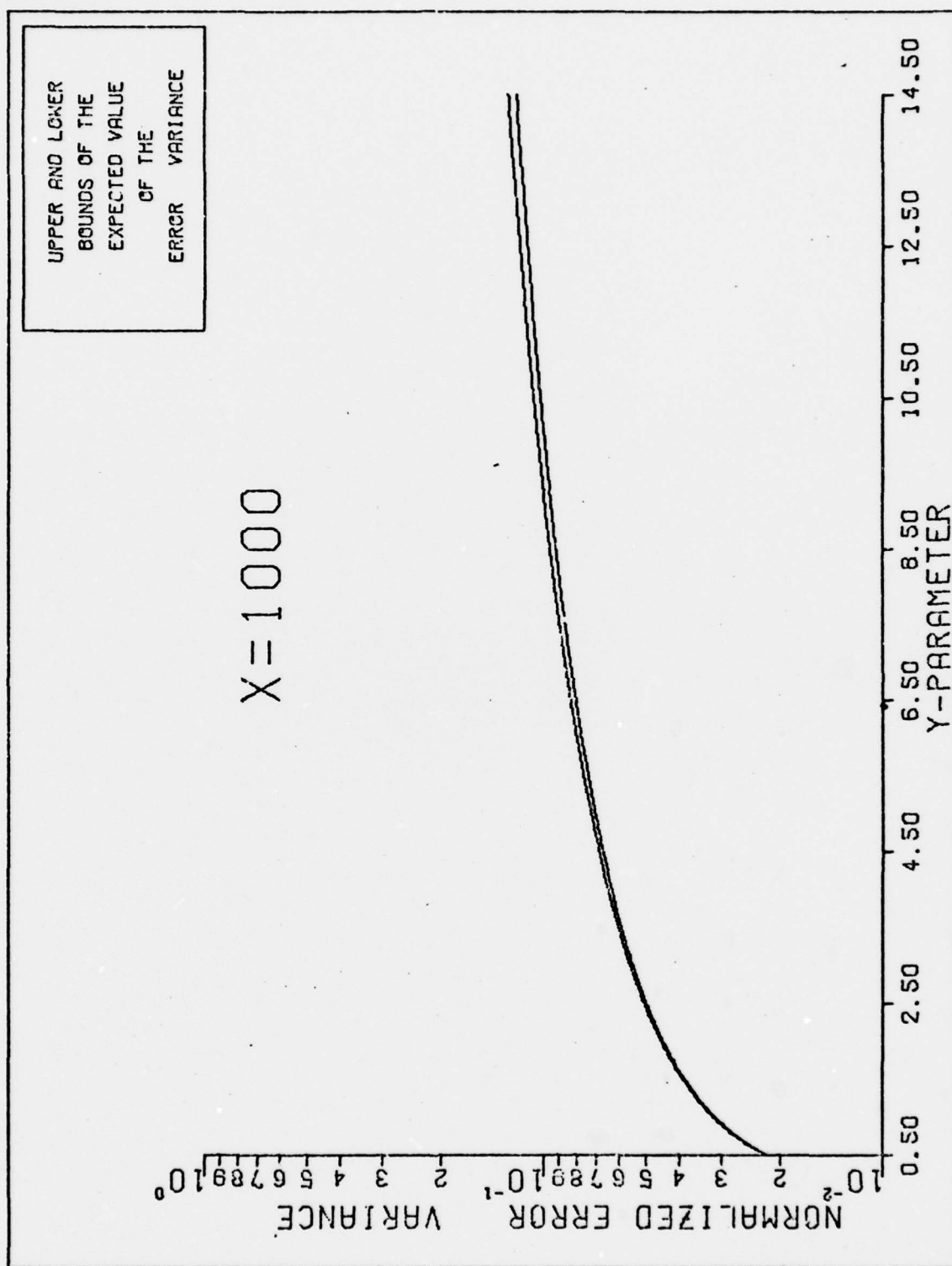


Figure 61. Upper and Lower Bounds on MSE

separation as  $X$  gets larger. Physically, the  $X$ -parameter can be described as the number of photoconversions in a coherence time of the spot's dynamics. As the number of data observations increases (i.e.,  $X$ -parameter increases), the filter has more information to correct and update its estimate of the spot's current position of maximum intensity. Thus, the filter can update its estimate frequently if a large number of events are observed in a relatively short period of time. Suppose, for example, the spot drifts on the detector with large "wanderings". Also, assume the filter has just processed one event and does not observe another event in a relatively long time (i.e., a low rate function or a small  $X$ ). Then the information provided by the "processed" event, has little value at some later time if the spot is "jittering" at higher frequency with large "wanderings" (i.e., spot dynamics have a small coherence time,  $\tau_c$ , and a large jitter,  $\sigma_x^2$ ). On the other hand, if the filter frequently observes a larger number of events within a coherence time, the Snyder Filter has more information concerning the spot's location on the detector surface.

Consider now a fixed  $X$  and a variation of the  $Y$ -parameter (Fig. 6e-6i). As  $Y$  increases, the bounds increase in magnitude and in relative separation.  $Y$  is the ratio between the spot's jitter normalized by the square of the beam width. The beam width indicates whether the filter should track the event locations closely in order to locate the spot. As the beam



width increases, photoelectrons are distributed at larger distances from the spot's centroid. Hence, increasing the beam width results in having less weight in the point-process measurements. Thus, the optimal gain,  $K(t)$ , should decrease as seen in Eq. (17).

Similarly, the noise strength,  $\sigma_x^2$ , indicates stronger noise sources driving the dynamics of the spot or increasing the uncertainty in the model. Increasing  $\sigma_x^2$  increases both the rate of growth of the conditional error covariance,  $\hat{P}(t)$ , between event times. This results in increasing values of the filter gain, implying larger weighting of the point process measurements. Stated another way, increasing the jitter indicates that the filter must put less "confidence" in the prediction capability of the filter's own internal dynamics model.

Physically, it is desirable to have a narrow beam width such that electrons can be distributed near the position of maximum intensity. At the same time, the spot's jitter should be small so that photoelectrons are released from a small area on the detector. This physical reasoning is described by the  $Y$  parameter.

With regard to the above discussion and by careful observation of Eqs (26) and (27), the upper and lower bounds converge to the steady state value of the actual MSE when  $X \gg 1$  and  $Y \ll 1$ . Referring back to the performance parameters, the estimator will perform well if a large number of signal photoelectrons are observed frequently and they appear

in a small area of a photodetector surface. This physical reasoning is described by the above parameters derived from upper and lower bounds. These parameters establish regions of operation where the upper and lower bounds converge to the actual mean square error. However, when the bounds do not converge, actual performance is difficult to obtain. To demonstrate the usefulness of the bounds and to determine which bound lies closer to actual performance, a Monte Carlo simulation is conducted. These parameters and the Snyder Filter assumes no dark current in the measurement process; and so an additional objective is to include dark current in the simulation to determine its effects in filter performance.

#### Summary

The chapter began by describing the direct detection optical receiver. The important point to remember is that the statistics of the output of the receiver govern the performance of optical components performing postdetection processing and vice versa. These statistics are described by a mathematical model called the point process. The model is applied in situations when the receiver is operating under low signal and background radiation. In this case, the discrete nature of light at optical frequencies and the nature of the detection process fundamentally limit the performance of optical trackers.

The Snyder Filter was discussed next. This filter, a recursive data processing algorithm, processes the point process observations of the receiver to estimate optimally the position of

maximum intensity on the detector surface. The Snyder Filter assumes its observations are from an infinitesimally fine detector array (i.e., the detector array has infinite resolution to measure the exact location of a photoconversion).

The chapter concluded with the performance parameters describing the mean-square-error of the Snyder Filter. The parameters are derived from the upper and lower bound on MSE. The two parameters are defined to establish conditions under which the Snyder Filter should yield good tracking. One parameter is the ensemble average of the number of photons detected in a coherence time of the spot's dynamics, and the other is the spot's jitter normalized by the square of the beam width. These parameters also indicate sufficient conditions, such that the bounds converge to the actual MSE. The MSE can then be used to evaluate the tracking capabilities of the Snyder Filter (i.e., to determine whether the average errors committed by the Snyder Filter are sufficiently small for tracking purposes). Again, these performance parameters and the Snyder Filter assume that the events locations are only due to the spot.

### III. Simulation of the Snyder Filter and Performance Analysis

The last chapter addressed the following concepts: (1) a mathematical model of the output process of the optical receiver, (2) a model of the spot's intensity profile and its dynamics, (3) the Snyder Filter which incorporates the measurement data  $\{t_k\}$  and  $\{r_k\}$  from the output of the receiver to estimate the position of maximum intensity, and (4) performance parameters which establish regions of operations where the bounds converge to actual MSE.

This chapter develops algorithms to implement the above models and to simulate the Snyder Filter in a digital computer. The algorithms that were developed are (1) simulation of spot's dynamics, (2) a noise generator, and (3) algorithms to generate the time-space point process observation (two methods).

Concluding the chapter is the performance analysis used to evaluate the tracking capabilities of the Snyder Filter.

#### Simulation of Spot's Dynamics

The spot's dynamics on the detector surface modelled by a linear stochastic differential equation given in Eq. (12), or in less rigorous form,

$$\dot{\tilde{x}}(t) = F(t)\tilde{x}(t) + G(t)\tilde{w}(t) \quad (30)$$

where  $\tilde{w}(t)$  is a white noise with zero mean and variance

$$E[w(t)w(t')] = Q(t)\delta(t-t') \quad (31)$$

where  $Q(t)$  is a diffusion strength variable. Consider an equivalent discrete-time model for digital simulation. Here, equivalence means that a discrete time process has the same second order statistics as  $\underline{x}(t)$ , when viewed at the sample times. As shown in Ref. (9:4.63), an equivalent discrete time solution to Eq. (30) is

$$\underline{x}(t_{i+1}) = \phi(t_{i+1}, t_i) \underline{x}(t_i) + \underline{w}_d(t_i) \quad (32)$$

where  $t_{i+1}, t_i$  are the discrete points in time,  $\phi(t_{i+1}, t_i)$  is the state transition matrix (scalar, in this case),  $\underline{w}_d(t_i)$  is the white discrete-time stochastic process with statistics:

$$E[\underline{w}_d(t_i)] = 0$$

$$E[\underline{w}_d^2(t_i)] = Q_d(t_i)$$

$$= \int_{t_i}^{t_{i+1}} \phi(t_{i+1}, \tau) G(\tau) Q(\tau) G(\tau) \phi(t_{i+1}, \tau) d\tau$$

$$; t_i = t_j$$

$$E[\underline{w}_d(t_i) \underline{w}_d(t_j)] = 0$$

$$; t_i \neq t_j$$

From Ref. (9:30), the mean  $m_x(t)$  and variance  $P_{xx}(t)$  of the process  $\underline{x}(t)$  propagate in time as

$$m_x(t_{i+1}) = \phi(t_{i+1}, t_i) m_x(t_i) \quad (33)$$



$$P_{xx}(t_{i+1}) = \Phi(t_{i+1}, t_i) P_{xx}(t_i) \Phi(t_{i+1}, t_i) + Q_d(t_i) \quad (34)$$

A simple model of the spot's dynamics on the detector is an output process of a first order lag driven by white Gaussian noise of zero mean. This model is represented as

$$\dot{x}(t) = -\frac{1}{\tau_c} x(t) + w(t) \quad (35)$$

where  $F(t) = -\frac{1}{\tau_c}$  and  $G(t) = 1$ . Then, its state transition matrix is

$$\phi(t, \tau) = \phi(t - \tau) = e^{-\frac{1}{\tau_c}(t - \tau)}$$

The model therefore becomes,

$$x(t_{i+1}) = e^{-\frac{\Delta t}{\tau_c}} x(t_i) + w_d(t_i)$$

where  $\Delta t$  is sample period (or observation time increment), and  $w_d(t_i)$  is a white Gaussian discrete-time process of zero mean and covariance

$$\begin{aligned} E[w_d^2(t_i)] &= \int_{t_i}^{t_{i+1}} \phi(t_{i+1}, \tau) G(\tau) Q(\tau) G(\tau) \phi(t_{i+1}, \tau) d\tau \\ &= \frac{\tau_c}{2} Q [1 - e^{-\frac{2\Delta t}{\tau_c}}] \\ &= \sigma_x^2 [1 - e^{-\frac{2\Delta t}{\tau_c}}] \end{aligned}$$

where  $Q = \frac{2}{\tau_c} \sigma_x^2$ , and  $\sigma_x^2$  Δ mean square value of output process  $x(t)$ , (in this report,  $\sigma_x^2$  represents the "jitter" of spot).  $Q$  is found in Ref. 9:4.77 ; and it represents the

the strength of the white noise. Eq. (35) is the expression which simulates the spot's dynamics on the detector. The next section discusses how a white Gaussian discrete-time process  $w_d(t)$  is generated.

### Noise Generators

A uniform random variable distributed between 0 and 1 is supplied by the computer system. This uniform number generator is used to generate realizations of random variables described by desired probability density functions or probability distribution functions. This will be shown in the next section.

However, applying the Central Limit of Statistics, one can generate an essentially Gaussian random variable by adding twelve independent uniform random variables distributed between 0 and 1. Since the mean and variance of a single uniform random variable is  $1/2$  and  $1/12$ , respectively, the above addition yields a Gaussian random variable with mean 6 and variance 1. To obtain a zero mean and a unit variance simply subtract 6 from the above result. Note that the Central Limit Theorem implies that the resulting random variable  $w$  has a probability distribution that approximates a Gaussian distribution (Ref. 11).

Finally, a Gaussian random variable  $w$  of desired variance  $\sigma_w$  and mean  $\mu_w$  is given by the following transformation equation

$$z = \frac{w - \mu_w}{\sigma_w}$$

or

$$w = \sigma_w z + \mu_w$$

where  $z$  is a Gaussian random variable with zero mean and unit variance.

The "whiteness" of the Gaussian discrete-time sequence  $w_d(t_i)$ , is obtained by independent calls of the above algorithm. The resulting set of  $w$ 's forms the white-Gaussian discrete-time process  $w_d(t_i)$  (i.e.,  $E[w_d(t_i)w_d(t_j)] = 0$  for all  $t_i \neq t_j$ ). Also, note that the second order statistics of  $w_d(t_i)$  (or set of random variables  $w$ ) are the second order statistics of the output process  $x(t)$ , of the first order lag. The statistics of  $w_d(t_i)$  are

$$\mu_w = 0$$

$$\sigma_w^2 = \sigma_x^2 (1 - e^{-\frac{2\Delta t}{\tau_c}})$$

#### Point Process Generation in Time and Space

In this report, two methods are employed to generate the event locations in time and space. One, the Binomial Method, is based on the incremental definition of the point process, and the other, the Conditional Method, makes use of conditional probability densities describing the output statistics of the receiver. The latter method uses Bayes' Rule. It should be noted that these conditional densities are derived by the incremental definition of a point process.

The Binomial rule will be discussed first. Next, a transformation equation used by the Conditional Method is described; then the Conditional Method follows. Concluding this section is a discussion on the theoretical and practical aspects of the two methods of simulation.

Binomial Method. Shown in Fig. (7) is a flowchart of the Binomial algorithm that generates the time-space events. As mentioned earlier, this development is based on the incremental definition of a point process. It is the same development describing the model of the photodetecting surface. For the purpose of clarity, a discussion on the point process incremental definition in one-dimensional space is given as

(1) Event in a space-time observation area,  $\Delta l \Delta t$ , are statistically independent where  $\Delta l$  is the incremental detector length,  $\Delta t$  is the incremental time observation.

$$P \left[ \begin{array}{c} \text{one event in} \\ \Delta l \Delta t \\ \text{located at } (t, r) \end{array} \right] = \lambda(r, \underline{x}(t)) \Delta t \Delta l + o(\Delta t \Delta l) \quad (36)$$

$$P \left[ \begin{array}{c} \text{zero events in} \\ \Delta l \Delta t \\ \text{located at } (t, r) \end{array} \right] = 1 - \lambda(r, \underline{x}(t)) \Delta t \Delta l + o(\Delta t \Delta l) \quad (37)$$

where  $P[\cdot]$  denotes probability of, the " $o\Delta l \Delta t$ " denotes higher order terms of  $\Delta l \Delta t$  (i.e.,  $\lim_{\Delta t \Delta l \rightarrow 0} \left( \frac{o(\Delta t \Delta l)}{\Delta t \Delta l} \right) = 0$ ), and  $\underline{x}(t)$  denotes location of maximum intensity on the detector surface. Note that different values of  $r$  will give different values of rate functions,  $\lambda(r, \underline{x}(t))$ .

Consider a uniform random number distributed between zero and

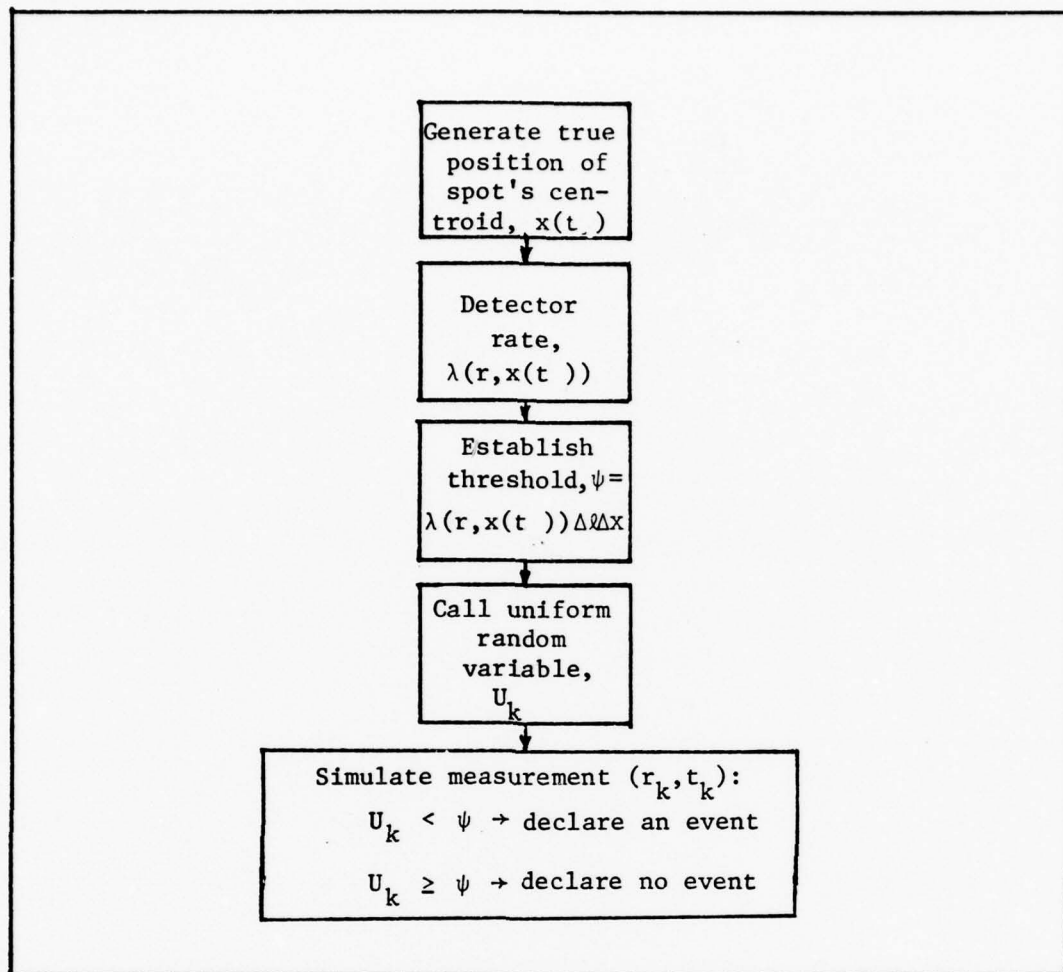


Figure 7. Flowchart of Binomial Method

one. Then, the probability of a value between zero and a number  $\psi$ , is simply  $\psi$ . So let  $\psi = \lambda(r, x(t)) \Delta t \Delta x$  establish a threshold to declare an event, where  $U_k$  is called from a uniform random generator (that is,  $U_k < \lambda(r, x(t)) \Delta t \Delta x$  means an event occurred at  $r$  on the detector surface).

The above module takes into account a different threshold and rate function when moving from one spatial point to another on the detector length. This method also includes effects of dark current (i.e.,  $\lambda(r, x(t)) = \lambda_g(r, x(t)) + \lambda_d$ ,



where  $\lambda_g \triangleq$  Gaussian rate function  $\lambda_d \triangleq$  dark rate function). The Binomial Method imposes a significant computational load in the simulation, as will be shown in a later section following the Conditional Method. Note that this method is an approximation for finite  $\Delta x$  and  $\Delta t$  and that there is an issue of coarseness of the time and space discretization. This creates implementation and theoretical aspects which will be discussed in a later section.

Transformation Equation. The transformation equation is used to generate a desired random variable of a given probability distribution function by calling a uniform random generator. In this case, either an event location or event time is generated by calling a uniform random variable  $U$  which is distributed between zero and one with probability density height 1. The solution to this transformation problem is found in Ref. (12:184) and is given as

$$U = F_D(D) \quad (38)$$

or

$$D = F_D^{-1}(U) \quad (39)$$

where  $F_D$  is the desired distribution function,  $D$  is the desired random variable,  $F_D^{-1}$  is the inverse function of  $F_D$ . Fig. (8) graphically depicts this solution.

The random variable,  $D$  represents either the random event location or time of the time-space point process. Similarly,  $F_D$  (or equivalently, the transformation function), corresponds

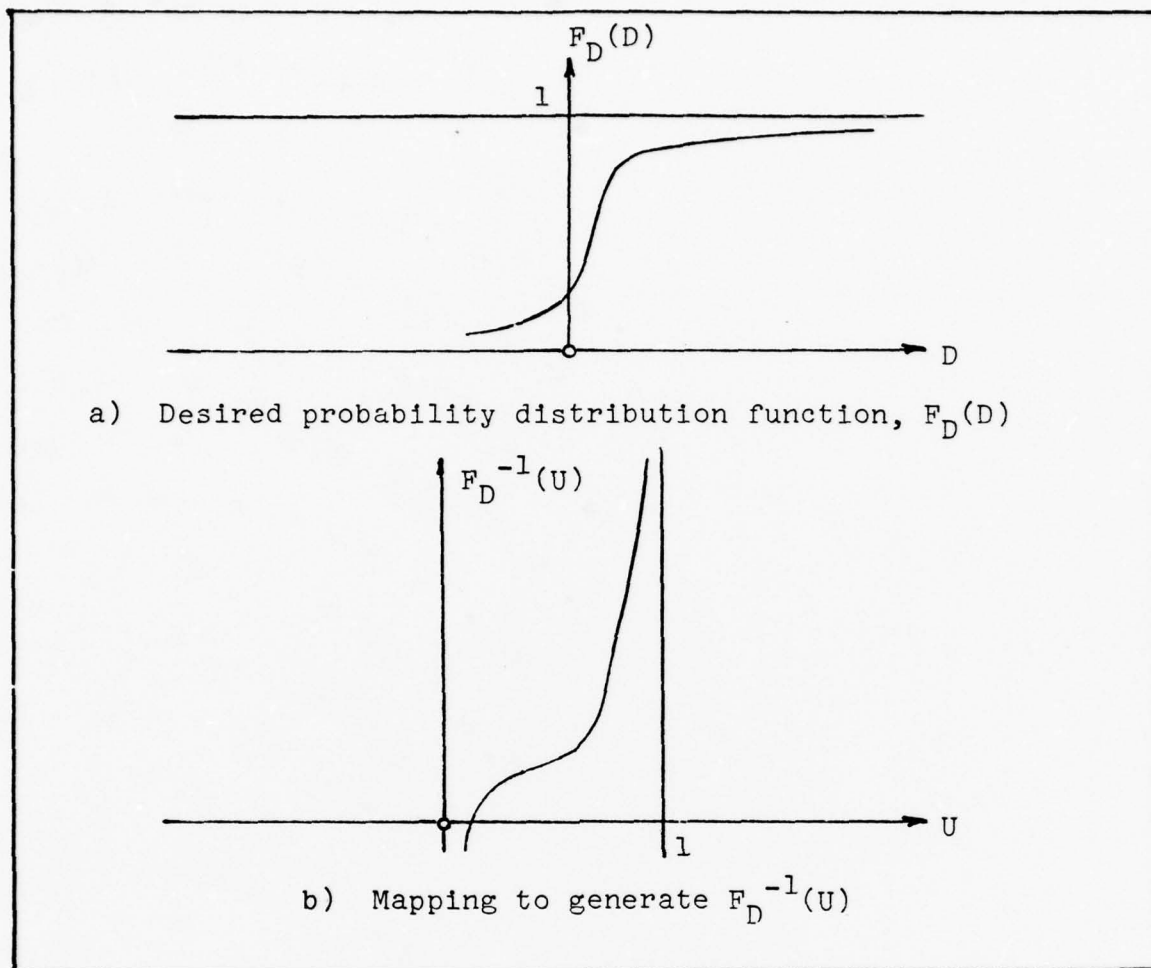


Figure 8. Generation of a Specified Probability Distribution Function (Copied from Ref. 12:184)

to either the event location or time probability distribution. In this report, these probability distributions are derived from the densities  $f[r_k|t_k, n]$  and  $f[s_k]$  where  $s_k$  is the interarrival times of ordered events 1, ( $k=0, 1, 2, \dots, n$ ),  $t_k$  is the event times from a time origin, and  $n$  is the number of events. These densities are shown in the next subsection.

Conditional Method. To generate the time-space point process events from the output process of the detector surface,

the number of events, the event times and event locations are needed. Here, the probability density  $f[\{r_k\},\{t_k\},n]$  is required to characterize output. This joint density is employed to derive the conditional densities of event times and event locations conditioned on knowing certain variables, where the variables are generated by actual implementation of the simulation. The development of this section will involve some lengthy (but not complex) derivations of expressions needed to generate  $\{r_k\}$  and  $\{t_k\}$ . Also, physical insights about the Snyder Filter's tracking capabilities will be cited where appropriate.

In this study, the variables  $I_0(t)$ ,  $\sigma(t)$ ,  $F(t)$ ,  $G(t)$ ,  $H(t)$ , and  $Q(t)$  are time-invariant. Then the average rate at which photoelectrons appear on the photodetectors array (after integrating the spatial dependence of the rate function, defined in Eq. (8), over entire detector length) yields

$$\lambda_0 = \frac{n}{nf_0} I_0 \sqrt{2\pi} \sigma + \lambda_d \ell \quad (40)$$

where Eq. (14) was used, and  $\ell$  is the detector length of array. Eq. (40) has terms including the effects due to dark current; however, in this relation, some assumptions were used, brought forth earlier in the report. To explain the first term in Eq. (40), it is assumed that the detector surface is large, such that, with respect to the spot's Gaussian intensity profile, the detector surface is infinitely large. Thus, edge effects of the spot's intensity profile on the detector may be ignored. On the other hand,  $\lambda_d$  is finite which means that  $\int_{-\infty}^{\infty} \lambda_d d\ell$

has an infinite value. Therefore, the integral,  $\int_{-\frac{l}{2}}^{\frac{l}{2}} \lambda_d d\ell$  results in the second term of Eq. (40). The major point is that the detector length must be large so that edge effects between the spot and detector are negligible when the spot is jittering about on the detector surface.

Consider the simulation of event times. It is known that the interarrival time, denoted as  $s_k$ , has an exponential density function (Ref. 3:60) given as

$$f[s_k] = \lambda_0 \exp(-\lambda_0 s) \quad (41)$$

To obtain  $F_D[s_k]$ , integrate Eq. (41) over the time continuum between  $-\infty$  and  $s_k$ . Using the transformation function from Eq. (38), Eq. (41) yields

$$U_k' = F[s_k] = 1 - \exp(-\lambda_0 s_k) \quad (42)$$

where  $U_k'$  is a uniform random variable distributed between zero and one. It then follows that  $U_k = 1 - U_k'$  is also a uniform variable with the same statistics. By straight forward manipulation, Eq. (42) yields

$$s_k = -\frac{1}{\lambda_0} \ln U_k \quad (43)$$

To get the event times, just use a running sum. In this case, with  $t_0$  as the initial time the event times of the point process with rate function  $\lambda_0$  can then be simulated by the following algorithm: call a uniform random variable,  $U_1$ ; use Eq. (43) to transform  $U_1$  to  $s_1$ ; assign  $s_1$  as the time from  $t_0$  to the first

photoconversion (i.e.,  $T_1 = t_0 + s_1$ ); call another uniform random variable,  $U_2$ ; transform  $U_2$  to  $s_2$ ; assign  $s_2$  as the time between the first and second photoconversion (i.e.,  $T_2 = T_1 + s_2$ ), and so forth (Ref. 3:62).

The next problem is finding an algorithm to generate the event locations,  $r_k$ 's. This problem is solved by using densities  $f[\{r_k\}, \{t_k\}, n]$  and  $f[\{t_k\}, n]$  (see Appendix A for derivation). These densities describe the statistics of the output process from the photodetector surface which are expressed as

$$f[\{t_k\}, \{r_k\}, n] = \exp\left(-\int_0^T \lambda(\alpha, \beta) d\alpha d\beta\right) \prod_{k=1}^n \lambda(t_k, r_k) \quad (44)$$

$$f[\{t_k\}, n] = \exp\left(-\int_0^T \lambda(\alpha) d\alpha\right) \prod_{k=1}^n \lambda(t_k) \quad (45)$$

where

$$\lambda(t_k, r_k) = \frac{n I_0}{f_0} \exp\left(-\frac{(r_k - \bar{x}(t_k))^2}{2\sigma^2}\right) + \lambda_d \quad (46)$$

$$\lambda_g(r_k, t_k)$$

$$\lambda(t_k) = \frac{n I_0}{f_0} \sqrt{2\pi} \sigma + \lambda_D \quad (47)$$

$$= \lambda_0$$

Note that  $f[\{t_k\}, n]$  is the marginal density of  $f[\{t_k\}, \{r_k\}, n]$  and that  $\lambda(t_k)$  in Eq. (47) has no spatial or temporal dependence.



Also, the integrals in Eq. (44) and (45) will both yield  $\lambda_0 T$ . Thus Eqs. (44) and (45) respectively yield

$$f[\{t_k\}, \{r_k\}, n] = \exp(-\lambda_0 T) \prod_{k=1}^n \lambda(t_k, r_k) \quad (48)$$

$$f[\{t_k\}, n] = \exp(-\lambda_0 T) \prod_{k=1}^n \lambda(t_k) \quad (49)$$

With the help of Bayes' rule, the conditional probability density function of event locations conditioned on knowing the event times and the number of events is given as

$$f[\{r_k\} | \{t_k\}, n] = \frac{f[\{t_k\}, \{r_k\}, n]}{f[\{t_k\}, n]}$$

$$= \prod_{k=1}^n \frac{\lambda_g(t_k, r_k) + \lambda_d}{\lambda_0}$$

or

$$f[\{r_k\} | \{t_k\}, n] = \left[ \frac{\lambda_g(t_1, r_1) + \lambda_d}{\lambda_0} \right] \left[ \frac{\lambda_g(t_2, r_2) + \lambda_d}{\lambda_0} \right] \cdot \left[ \prod_{k=3}^n \frac{\lambda_g(t_k, r_k) + \lambda_d}{\lambda_0} \right]$$

$$= f_1[r_1 | t_1, n] f_2[r_2 | t_2, n]$$

$$\cdot \prod_{k=3}^n f_k[r_k | t_k, n] \quad (50)$$

where Eqs. (48) and (49) were used. The above relation says that the joint conditional density  $f[\{r_k\}|\{t_k\},n]$ , can be derived by forming the product of each of the densities at the time-space coordinates,  $(t_k, r_k)$ . Thus, for  $n=1$  at  $(r_k, t_k)$ , the conditional density of  $r_k$  given  $t_k$  is expressed as

$$f[r_k|t_k] = \frac{\lambda_g(t_k, r_k)}{\lambda_0} + \frac{\lambda_d}{\lambda_0} \quad (51)$$

Before proceeding further, it is useful to check if Eq. (51) is normalized (i.e.,  $\int_{-\infty}^{\infty} f[r_k|t_k] d\alpha_k = 1$ ). That is,

$$\begin{aligned} \frac{1}{\lambda_0} \int_{-\infty}^{\infty} \frac{n}{f_0} I_0 \exp\left(-\frac{(\alpha_k - x)^2}{2\sigma^2}\right) d\alpha_k + \frac{1}{\lambda_0} \int_{-\frac{\ell}{2}}^{\frac{\ell}{2}} \lambda_d d\alpha_k \\ = \frac{1}{\lambda_0} \left( \frac{n}{hf_0} I_0 \sqrt{2\pi} \sigma + \lambda_d \ell \right) = 1 \end{aligned}$$

Again, it is assumed that the detector is large such that the limits in the integral of the first term on the left side of Eq.(52) are approximately valid.

To get the probability distribution function,  $F[r_k|t_k]$  integrate  $f[r_k|t_k]$  over the detector plane from  $-\infty$  to  $r_k$  for the first term and from  $-\frac{\ell}{2}$  to  $r_k$  for the second term in Eq. (51). The result is expressed as

$$F[r_k|t_k] = \frac{1}{\lambda_0} [\text{erf } v + \lambda_d (r_k + \frac{\ell}{2})] \quad (53)$$

where

$$\operatorname{erf} v \triangleq \frac{2}{\sqrt{\pi}} \int_0^v \exp(-z^2) dz$$

$$v \triangleq \frac{r_k - x(t_k)}{\sqrt{2} \sigma}$$

Using the transformation equation defined in Eq. (39) and after algebraic manipulation, Eq. (53) yields

$$\operatorname{erf} v + \left( \frac{2}{\sqrt{\pi}} A_1 \right) v = 2A_2 U_k - 1 + 2A_3 x(t_k) + \frac{\ell}{2} \quad (54)$$

where

$$A_1 \triangleq \frac{\lambda_d}{\frac{n I_0}{h f_0}}$$

$$A_2 \triangleq \frac{\frac{n I_0}{h f_0} \sqrt{2\pi} \sigma + \lambda \ell}{\frac{n I_0}{h f_0} \sqrt{2\pi} \sigma}$$

$$A_3 \triangleq \frac{\lambda_d}{\frac{n I_0}{h f_0} \sqrt{2\pi} \sigma}$$

Eq. (54) is used to generate the event locations at the event times given the variables defined in this expression. The event locations are generated by a table lookup method with linear interpolation and is performed as follows:

(1) Evaluate and obtain all necessary variables, i.e.,  $A_1$ ,  $A_2$ ,  $A_3$ ,  $\frac{\ell}{2}$ ,  $U_k$ , and  $x(t_1)$ ,

(2) For a specific range of values for  $v$ , solve the expression on the left-hand side of Eq. (54), and store the results in a table (i.e., computer memory),

(3) Derive a random variable  $s$  by calling a uniform random variable,  $U_k$ , distributed between (0,1) and by obtaining the true position of the centroid,  $\underline{x}(t)$ , from the truth model simulation. Given these values, the right-hand side of Eq. (54) is evaluated and the random variable realization  $s$  is obtained,

(4) To find  $v$ , obtain  $s$  by a table lookup with linear interpolation. In the table the increment of  $v$  is equal to 0.025, where erf  $v$  is piecewise linear for this approximation; thus, linear interpolation is used

(5) Upon finding  $v$ , it then follows that the event location is evaluated by the following expression:

$$r_k = (\sqrt{2} \sigma)v + x(t_k)$$

This paragraph completes the algorithm of generating the event locations.

Since Eq. (54) governs the generation of event locations, it is useful to examine this relation for limiting cases (i.e.,  $\lambda_d = 0$  and  $\lambda_g(t_k, r_k) = 0$ ). This investigation will provide insights into the tracking capabilities of the Snyder Filter.

$\lambda_d = 0$  implies  $A_1 = A_3 = 0$  and  $A_2 = 1$ . Eq. (54) is then manipulated into a convenient form as

$$U_k = 1/2 \left( 1 + \operatorname{erf} \left( \frac{r_k - x(t_k)}{\sqrt{2} \sigma} \right) \right) \quad (55)$$

$$U_k = F_D(r_k | t_k) \quad (56)$$

where Eq. (38) is implemented in the last expression. Corresponding to  $F_D(r_k | t_k)$  is  $f(r_k | t_k)$  which is given as

$$f[r_k | t_k] = \frac{1}{\sqrt{2\pi}\sigma} \exp\left\{-\frac{1}{2\sigma^2}[r_k - x(t_k)]^2\right\} \quad (57)$$

The event locations are generated by calling a Gaussian random variable of mean  $x(t_k)$  and variance  $\sigma$ , at the event times. Note that the intensity profile of the spot being Gaussian-shaped leads to a result that the event locations are generated as Gaussian random variables conditioned on knowing the event times. The Snyder Filter is based on the assumption of a Gaussian-shaped profile of the spot. Thus, for  $\lambda_d \neq 0$ ,  $A_1$  "smears" out the Gaussian information as seen in Eq. (54).

For  $\lambda_g(r, t) \gg \lambda_d$ , the effect of dark current is examined by doing a perturbation analysis. This analysis is performed by factoring out the larger of the two rate functions in Eq. (47). Then the natural logarithm of the left and right hand side of Eq. (47) becomes

$$\ln f(\{r_k\} | \{t_k\}, n) \approx \sum_{k=1}^n \ln \frac{\lambda_d}{\lambda_0} + \sum_{k=1}^n \frac{\lambda_g(r_k, t_k)}{\lambda_0}$$

where the approximation  $\ln \left( 1 + \frac{\lambda_g(r_k, t_k)}{\lambda_d} \right) \approx \frac{\lambda_g(r_k, t_k)}{\lambda_d}$  and



$\frac{\lambda_g(r_k, t_k)}{\lambda_d} \ll 1$  is used. The exponential of the left and right hand side of the above equation yields

$$f[\{r_k\}|\{t_k\}, n] \approx \prod_{i=1}^n \frac{\lambda_d}{\lambda_o} \exp\left(\frac{\lambda_g(r_k, t_k)}{\lambda_o}\right) \quad (58)$$

Again, Eq (58), can be derived by forming the product of the above individual densities at  $(r_k, t_k)$ . Then, setting  $\lambda_g(r_k, t_k) = 0$  in Equation (58) and applying this condition to Eq (40), Eq (58) yields

$$f[r_k|t_k] \approx \frac{1}{\ell} ; \quad -\frac{\ell}{2} < r_k < \frac{\ell}{2} \quad (59)$$

where  $n = 1$ . Intuitively, Eq (58) is reasonable, since at any given time a dark event can occur in any differential length on the detector surface with equal probability.

In summary, for signal-limited conditions, the event locations are called as a Gaussian random variable with mean  $\bar{x}(t_k)$  and variance  $\sigma^2$ ; for dark-limited conditions the event locations are generated as uniform random variables distributed in  $(-\frac{\ell}{2}, \frac{\ell}{2})$  with probability density height  $\frac{1}{\ell}$ ; and for generating event locations other than the limiting cases, Eq (54) is implemented. Finally, the generation of event locations is called at the event times given by Eq (43).

Aspects of Implementing each method. The Binomial Method has two restrictions for its algorithm to work properly: one, is  $\lambda[r, x(t)]\Delta\ell\Delta t \leq 1$  and the other, is  $\Delta\ell\Delta t \ll 1$  where for implementation purposes  $\Delta t$   $\Delta$  sample time or observation time

interval. Because of these conditions, several practical and theoretical problems arise. One is a resolution problem. The Snyder Filter assumes that its position-sensitive measurements are from an infinitesimally fine partitioned detector array. No matter how small " $\Delta l$ " is, there is still a problem in extracting the "exact" location of the event. For this report, the detector array is divided into equal increments of  $\Delta l$ , and the value of the rate function at the center of each incremental length, is chosen to evaluate the probability,  $\lambda(r, x(t)) \Delta l \Delta t$ . This procedure determines where an event (if any) occurred on the detector surface. This method is depicted in Fig (9). Note that  $\Delta t$  is the observation increment during the simulation time. From a practical point of view, this method consumes a large amount of computer time; at each time increment of observation,  $\Delta l$  is scanned across the detector surface from one end to the other.

In the Binomial Method, a theoretical point that should be considered is the question of "simultaneous" events occurring on the surface. The Snyder Filter assumes that one event is observed at any one time. With this simulation method, there is a probability that more than one event can occur. Even if  $\Delta t \ll 1$  and  $\Delta l \ll 1$ , there is still a probability (though small) that simultaneous events can occur at different locations. It was mentioned previously that scanning the detector surface for small  $\Delta l$  results in a large consumption of computer time at each time increment. Thus, if a smaller  $\Delta t$  or  $\Delta l$  is chosen to reduce the probability of simultaneous events, this will result in a larger consumption of computer resources.

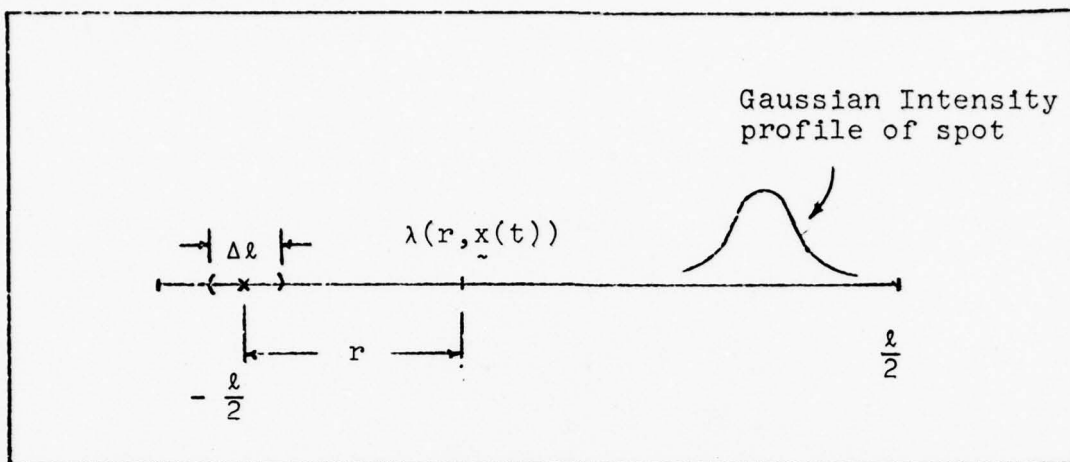


Fig. 9. Resolution problem in Binomial Method

Furthermore, when dark current is included in the simulation, the probability of simultaneous events grows substantially. To reduce the amount of computer resources (and to observe the errors generated by the Snyder Filter between event times), the rate functions are chosen to have a low value. This enables the use of a larger sample period,  $\Delta t$ , which also implies a higher probability of simultaneous events. It is evident now that the Binomial method has implementation problems. In spite of these problems this method is performed in the computer, and the results are shown in the next chapter.

In terms of implementation, the Conditional Method is a better algorithm, since the event locations are called at the event times; (i.e., the problem of simultaneous events is precluded). In the simulation it is desirable to sample the errors committed by the Snyder Filter between successive event times. In this case, it is convenient to break up the simulation time interval (observation time) into time increments,  $\Delta t$ .  $\Delta t$  will denote the sample period in order to sample the

error process (as done in the Binomial Method). When the event times are generated, there is a situation that the interarrival times,  $w_k$ 's, can occur smaller than the sample period (i.e.  $s_k < \Delta t$ ). This situation is shown in figure (10).

#### Performance Analysis

The objective of the performance analysis is to characterize the error process statistically. This is done by generating many samples of the error process through Monte-Carlo simulation. The simulation uses random number generators and shaping filters to generate the random errors. One objective in the simulation is to portray filter performance capabilities when parameters that describe the problem are varied. First, consider the test cases without dark current. Here, the signal rate function or spot's jitter are changed and, thus, filter capabilities can be evaluated. Note that changing the signal rate varies the average number of photons detected per coherence time; similarly, changing the spot's jitter causes variations in the  $Y$  parameter. In this study, the test cases do not meet sufficient conditions which are  $X \gg 1$  and  $Y \ll 1$ ; therefore, the results should provide an indication of which bound is close to actual performance. A plot which contains the sample variance and average filter variance is a useful output to make this comparison.

Second, the measurement model (of which the Snyder Filter is based) is altered by presenting dark events in the measurement process. The above plot is again a useful output to evaluate the filter's sensitivity to dark measurements.

In this study, a final objective of the performance analysis is to change the filter structure, through ad hoc methods, when

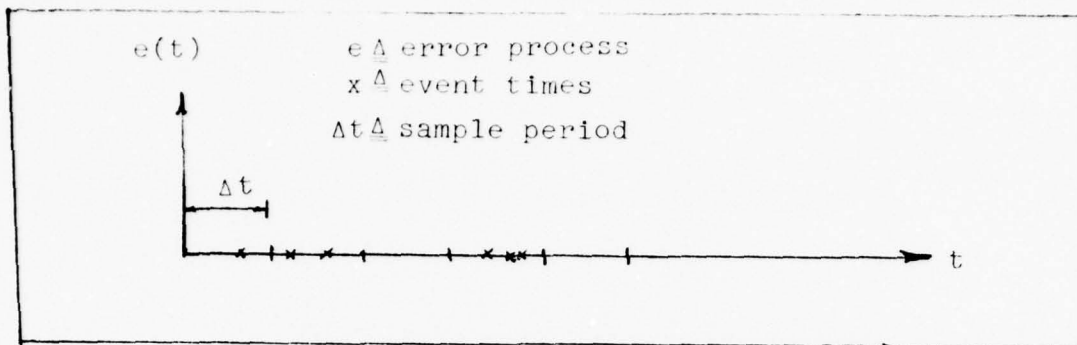


Fig 10. Sampling the Error Process with Fixed Sample Period (Conditional Method)

satisfactory performance cannot be obtained in the presence of dark events. Again, the above plot containing the variances would be useful in providing insights of how to alter the filter structure.

As previously mentioned, the error process is characterized by generating many sample runs of this process. The appropriate number should be chosen sufficiently large, such that additional sample runs does not appreciably change the sample statistics. The last statement is an illustration of the weak law of large numbers: let  $E[\bar{e}] = \bar{e}$  denote the ensemble average of the error process  $\bar{e}$ . Also, let  $\langle \bar{e} \rangle_N$  denote the empirical average for  $N$  runs. When  $N$  is large, the weak law states with high probability that  $\langle \bar{e} \rangle_N$  is close to the number  $\bar{e}$ . In mathematical terms,

$$P[|\langle \bar{e} \rangle_N - \bar{e}| > \epsilon] = \frac{\sigma_{\bar{e}}^2}{N\epsilon^2}$$

where  $\langle \bar{e} \rangle_N \triangleq \frac{1}{N} \sum_{j=1}^N e_j$  sample mean error,  $N \triangleq$  number of statistical independent random variables,  $e_j$  with mean,  $\bar{e}$  and variance  $\sigma_{\bar{e}}^2$ , and  $\epsilon$  is an arbitrary constant. The



weak law is a measure of the confidence of inferring information about the actual statistics of the error process (Ref 11:96). Thus, as the number of sample runs increases, the confidence in characterizing the error process accurately increases.

Sample statistics. The statistics computed at each time point are the calculated mean error  $\bar{e}$ , calculated variance  $\sigma_e^2$ , and the ensemble average of the filter variance terms  $\overline{PF}$ . These calculations are performed over the ensemble of runs  $N$ , for each time point  $t_m$ . These expressions are

$$\langle e(t_m) \rangle_N = \frac{1}{N} \sum_{j=1}^N [\hat{x}(t_m) - x(t_m)] \quad (60)$$

$$\begin{aligned} \sigma_e^2(t_m) &= \frac{\sum_{j=1}^N [x(t_m) - \hat{x}(t_m)]^2}{N-1} \\ &\quad - \frac{\sum_{j=1}^N N[\langle e(t_m) \rangle_N]^2}{N-1} \end{aligned} \quad (61)$$

$$\overline{PF}(t_m) = \frac{1}{N} \sum_{j=1}^N PF(t_m) \quad (62)$$

The above relations are found in Ref (13). Note that the time point  $t_m$  are not event times but are the sample times for a fixed sample period  $\Delta t$ . From Eq (61), the variance  $\sigma_e^2(t_m)$  is divided by  $(N-1)$  instead of  $N$ , which results in an unbiased estimator of variance (Ref 13).

Plots. Mentioned in previous paragraphs is that a useful output in the analysis is a plot of the average filter estimate of the error variance, along with the corresponding computed

sample (or true) variance for all times of interest. This output is used to compare if the sample variance of the error process matches with the filter's average error variance. In other words, this output should indicate how well the filter is estimating its errors with the actual errors it commits; and to compare with the bounds on MSE for test cases where dark current is set equal to zero.

A second useful output on this analysis is a plot of the mean error versus time. Along with this plot are the standard deviation bounds plotted above and below the mean error. This plot is useful if the Snyder Filter provides the desired accuracy. The two plots that were just described, are used to analyze the average error performance of the Snyder Filter. For all cases, these plots are used to determine whether the actual errors committed by the filter are sufficiently small to yield good tracking performance.

Now consider plots of individual sample of the error process. For no dark current, this plot is used to observe how the Snyder Filter minimizes its errors. When dark current is represented in the simulation, then the Snyder Filter sensitivity to the dark measurements can be observed. Along the zero axis of this plot are the event times to indicate clearly how the filter updates its estimate at the event times. Also, a plot of the sample filter variance is also of interest in order to observe how the Snyder Filter propagates the uncertainty of its estimate in time.

Test cases. During this study, different cases using different values of X and Y performance parameters are considered. The test cases are given in tables (1) and (2). All test cases are performed where there is a relative separation between the bounds. Here, the bound lying closer to actual performance can be determined. For the test cases in Table (1) and (2), the dark current is set equal to zero.

When dark current is presented in the simulation separate test cases are performed. The measurement process of the Snyder Filter is altered by this addition of dark current. For these test cases, a sensitivity parameter is defined to be the average signal-to-noise counts ratio which is expressed as

$$\frac{S}{N} = \frac{\frac{nI_o}{hf_o} \sqrt{2\pi} \sigma}{\lambda_d \ell}$$

Here, the degree of degradation in filter performance is observed as the average signal-to-noise counts ratio is varied. Because of the time constraints imposed in the study, limited cases for  $\lambda_d \neq 0$  are examined.

### Summary

The chapter developed the necessary algorithms needed to perform this study. These algorithms consists of simulating the spot's dynamics, and the generation of position-sensitive measurements (i.e. time-space point process). The chapter concluded with a general discussion on performance analysis, where it consists of sample statistics, plots, and test cases needed to investigate the tracking capabilities of the Snyder Filter.

Performance Parameter	
X	Y
5.0	0.1
5.0	0.25
5.0	1.0

Table 1. Test Cases for Binomial Method  
(without dark current)

Performance Parameter	
X	Y
5.0	0.5
5.0	1.0
5.0	5.0
5.0	10.0
1.0	0.5
1.0	1.0
1.0	5.0
1.0	10.0
0.5	5.0
10.0	5.0
15.0	5.0
20.0	5.0
0.5	1.0
10.0	1.0
15.0	1.0
20.0	1.0

Table 2. Test Cases for Conditional Method  
(without dark current)

#### IV Results

This chapter contains results from the Monte Carlo simulation. The simulation will indicate how well the actual performance can be described, when compared to the upper and lower bounds. Thus, various values on the set of parameters, derived from the bounds, are used to determine which bound is closer to actual performance. The bounds are valid only when the measurement is perfect (i.e., there are no dark or background noise events). When dark current is included in the simulation, the results should show the degree of degradation in filter performance. Finally, to compensate for the effects of dark current and to improve tracking performance, different methods in changing the filter structure are exploited.

##### Mean and Variance Convergence

To determine the appropriate number of sample runs, two plots are generated. One plot shows the sample mean error versus the number of runs, and the other plot shows the sample variance of error process versus the number of runs. These plots are shown in Fig. (11) for the Binomial Method. On each of the two plots are four curves corresponding to four arbitrary time points (as indicated in the figure) during the simulation time. By the weak law of large numbers, the mean and variance of the error process should converge to a steady value such that the variance or mean of the error process does not change much in magnitude with each addition of sample runs. Based on this reasoning and the results from the plots, fifty sample runs are selected. This number of runs will also be used in the conditional method. However, it does not appear that fifty runs are sufficient



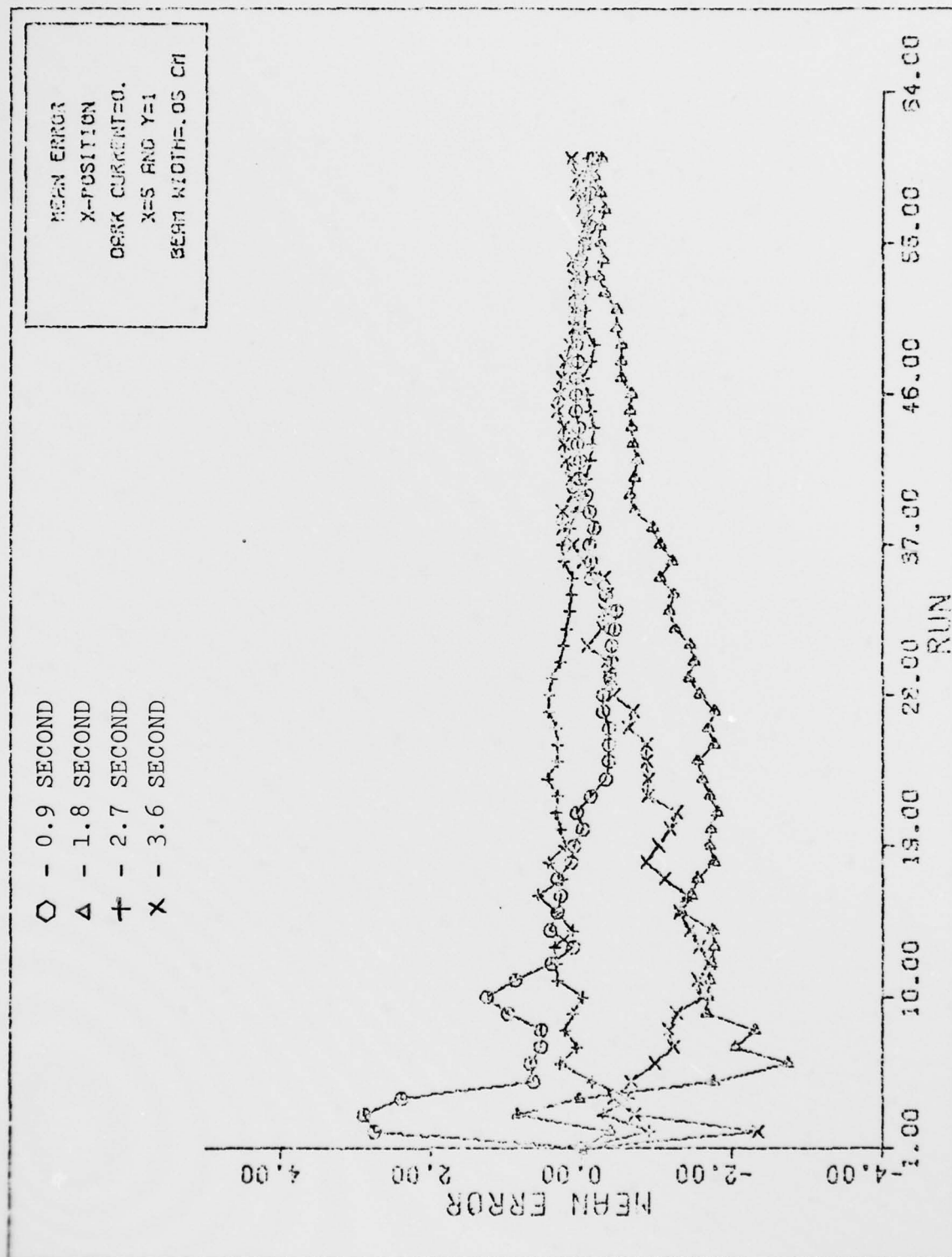


Figure 11a MEAN CONVERGENCE

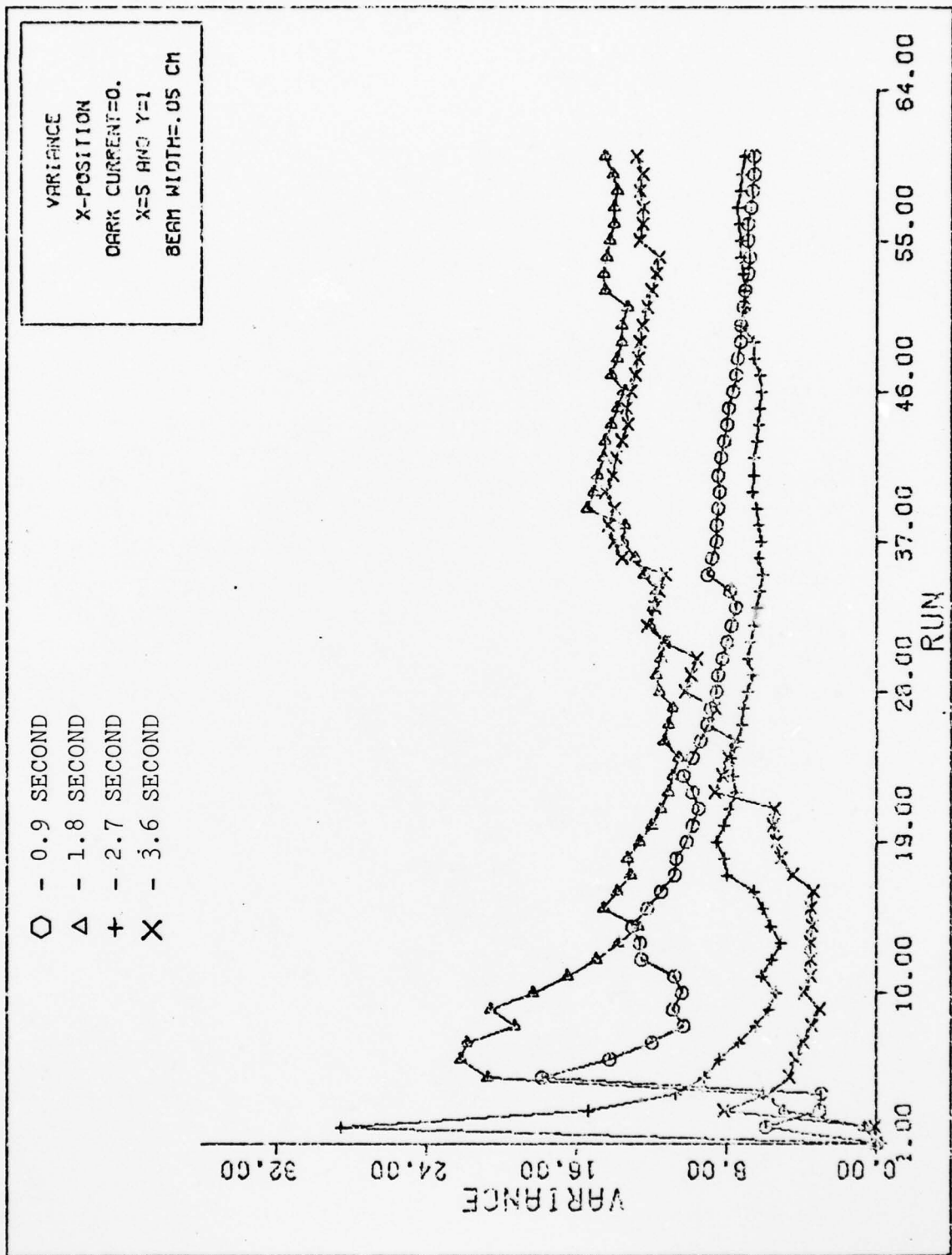


Figure 11b VARIANCE CONVERGENCE

to ensure convergence for all the test cases listed in Tables 1 and 2. That is, the performance parameters, X and Y, which are defined in Chapter II as

$$X = \left( \frac{\eta I_0 \sqrt{2\pi}}{hf_0} \right) \left( \frac{1}{2} \tau_c \right) \Delta \quad \begin{array}{l} \text{average number of electrons} \\ \text{occurring in one-half the} \\ \text{coherence time of spot's} \\ \text{dynamics } (\lambda_d=0) \end{array} \quad (63)$$

and

$$Y = \frac{\sigma_x^2}{\sigma^2} \Delta \quad \begin{array}{l} \text{spot's jitter normalized by the square of} \\ \text{the beam width} \end{array} \quad (64)$$

have different values. The plots shown in Fig. (12) provide an additional illustration of confidence in the sample variances. They are plots of the variances of the error process (calculated from sample statistics) for different numbers of sample runs. On the true variance curves are symbols, denoted as "x", to distinguish from the filter variance curve. Along with the curves are the upper and lower bound on MSE for the given set of parameters X and Y. These plots show that as the number of simulation runs increases, the fluctuations of the true and filter variances decrease. The plots also indicate that the fluctuations should settle to a value that is between the upper and lower bounds (as expected). Hence, the number of runs indicate the amount of confidence that the sample and average filter sample variances approach the corresponding true variances. Although fifty simulation runs may not be appropriate for all the test cases, it does provide an indication of filter performance.

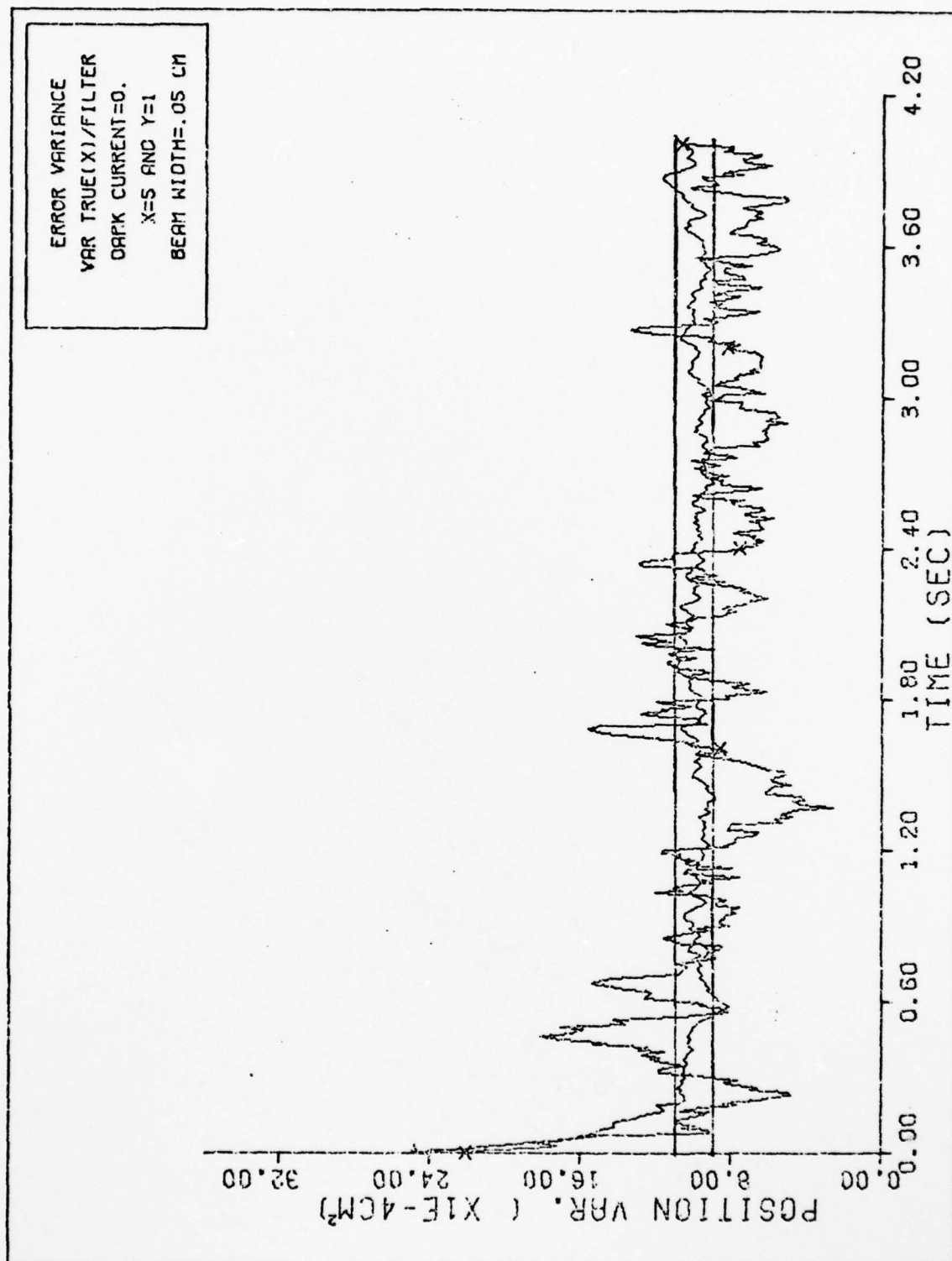


Figure 12a X-POSITION VARIANCES  
(20 SAMPLE RUNS)

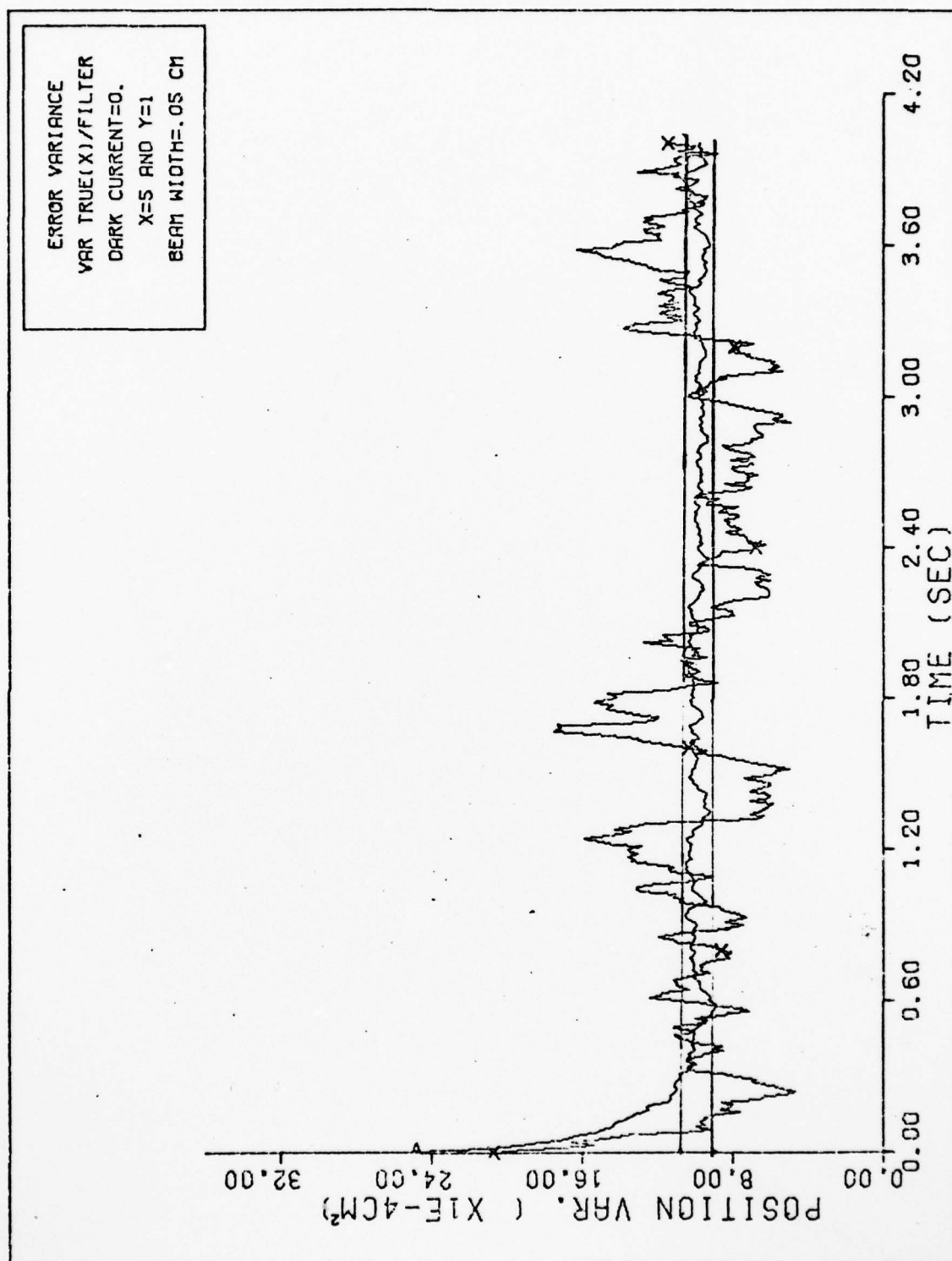


Figure 12b X-POSITION VARIANCES  
(40 SAMPLE RUNS)



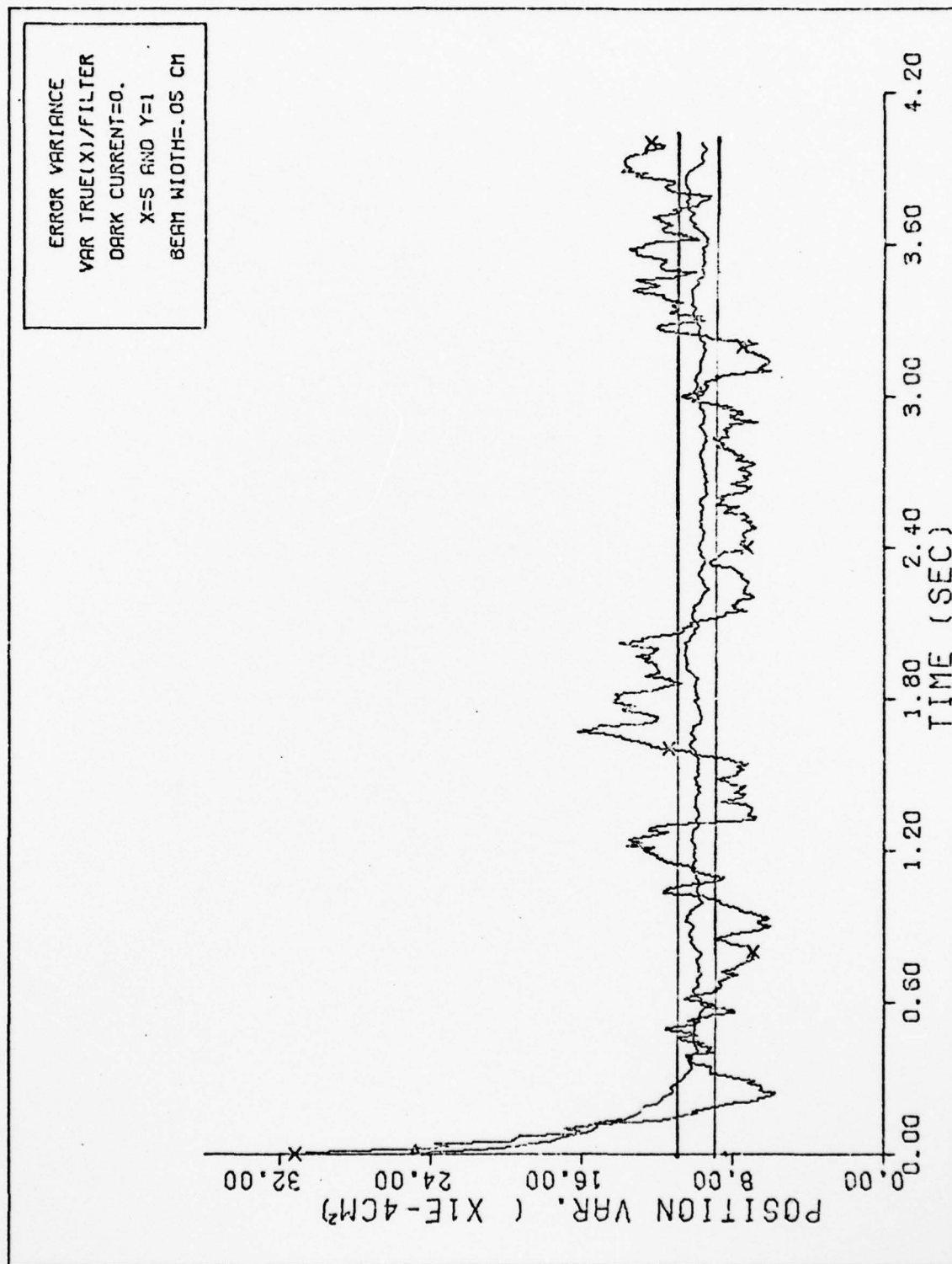


Figure 12c X-POSITION VARIANCES  
(60 SAMPLE RUNS)

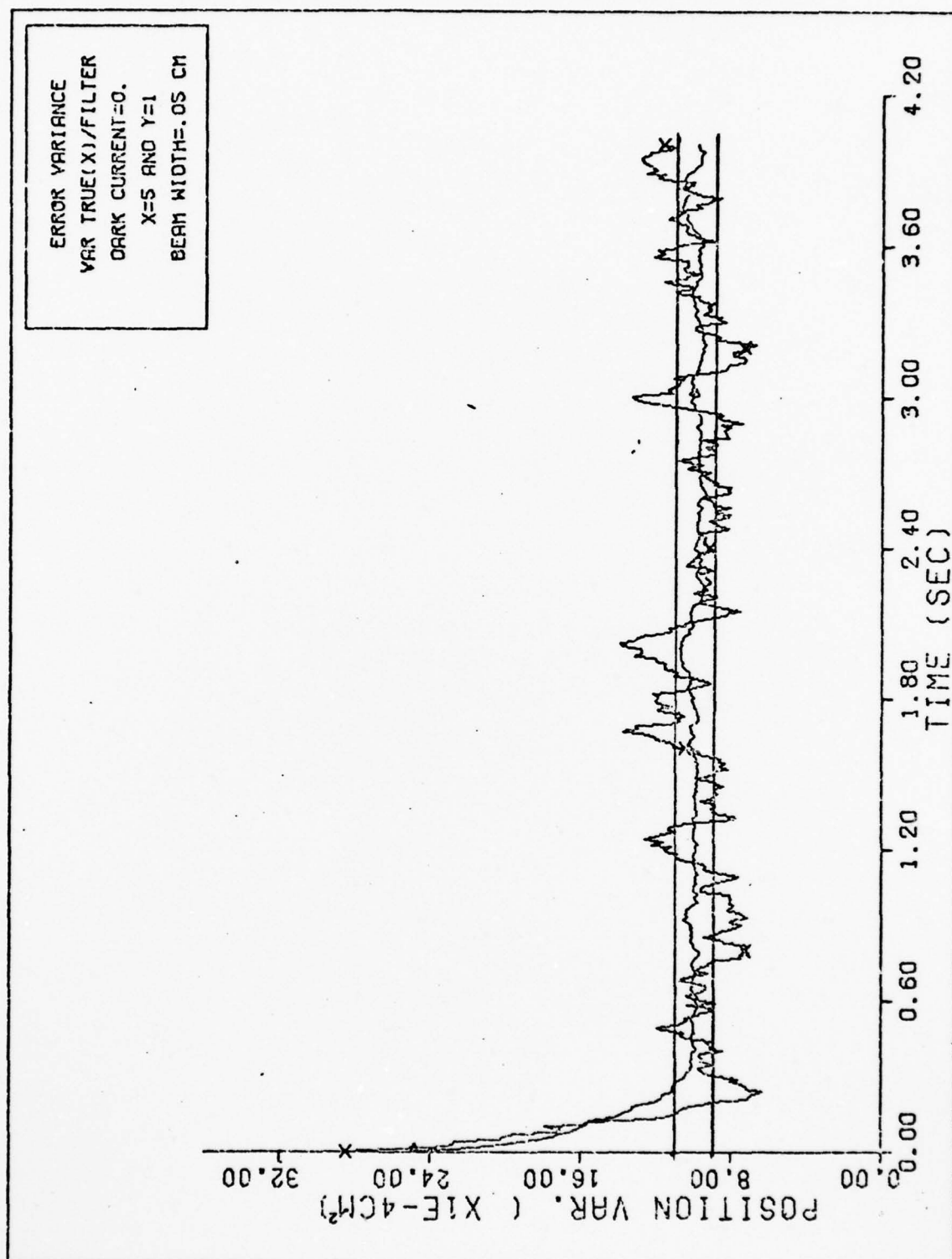


Figure 12d X-POSITION VARIANCES  
(80 SAMPLE RUNS)

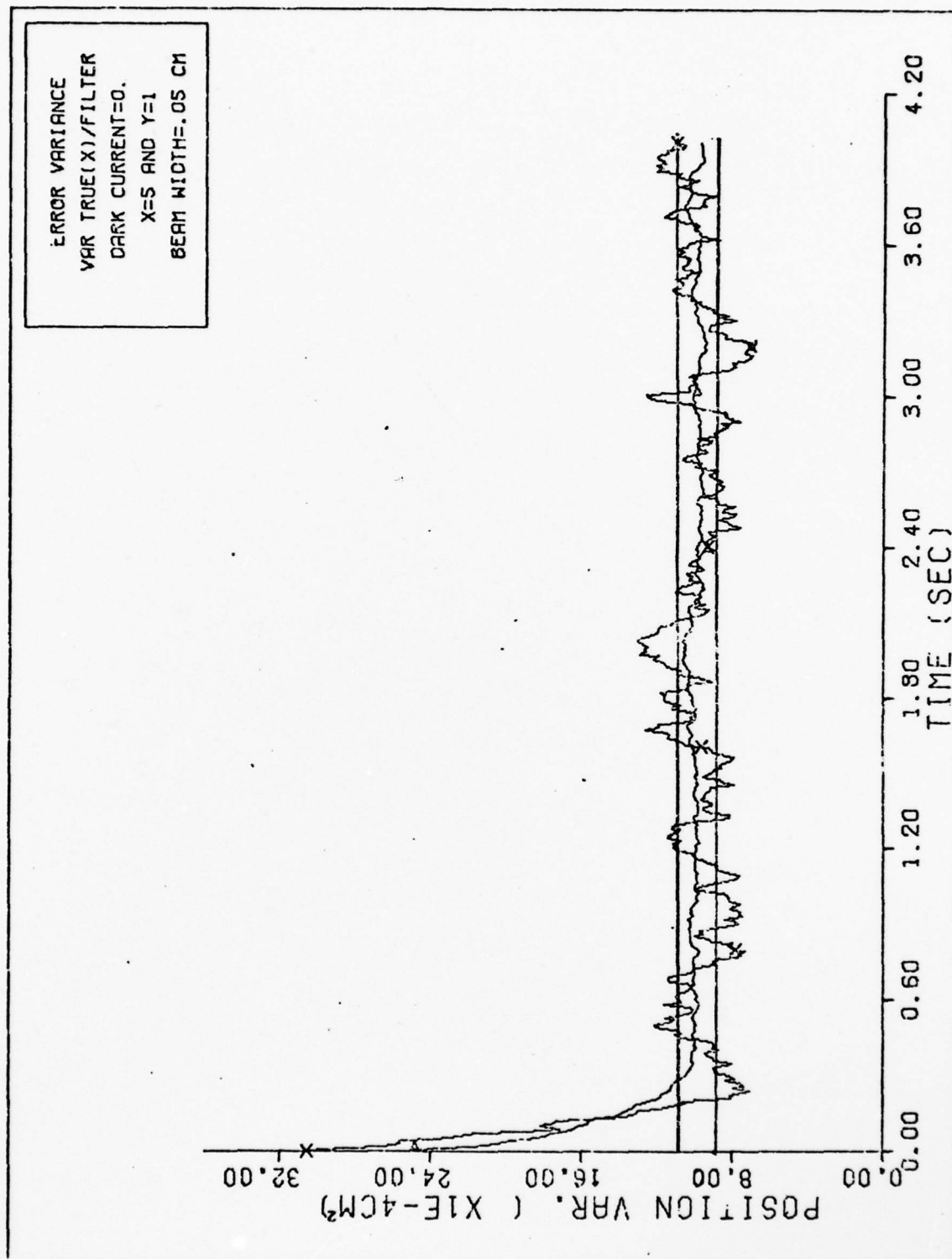


Figure 12e X-POSITION VARIANCES  
(100 SAMPLE RUNS)

### Binomial Method (without dark current)

For the Binomial Method, it was mentioned in the previous chapter that simultaneous events can be generated at the sample period,  $\Delta t$ . This situation would occur often if the observation area,  $\Delta t \Delta \lambda$ , is not sufficiently small. In addition, a low rate function,  $\lambda(t, r)$ , is selected to observe the propagation of the conditional mean and variance of the Snyder Filter and to reduce the amount of computer resources by this method. During this part of the study, it is found that simultaneous events did occur even for a rate function of 10 events per second with a sample period of 0.01 second. For  $X=5$ , simultaneous events occurred on the average of two to three times per sample run. To avoid this problem, a software routine is developed to randomly pick one of two simultaneous events. Note that this routine ruins the statistical properties of the point process.

Figs. (13a, 14a) and (13b, 14b) are plots of the sample error and sample filter variance, respectively, for the parameters  $X=5$  and  $Y=1$ . Note on the time axis of each plot are the event times. In Figs. (13a) and (14a), the errors decrease as events appear frequently in time (as expected). Similarly, in Figs. (13b) and (14b), the conditional variance is updated at the event times, otherwise the variance grows in time when an event is not observed. Note, the filter variance is "driven" to a smaller value as more events appear frequently in time. If the filter does not observe many measurements, the filter will weigh the next measurement heavily, driving the filter variance to a lower value. If many previous measurements appear frequently in time, this implies

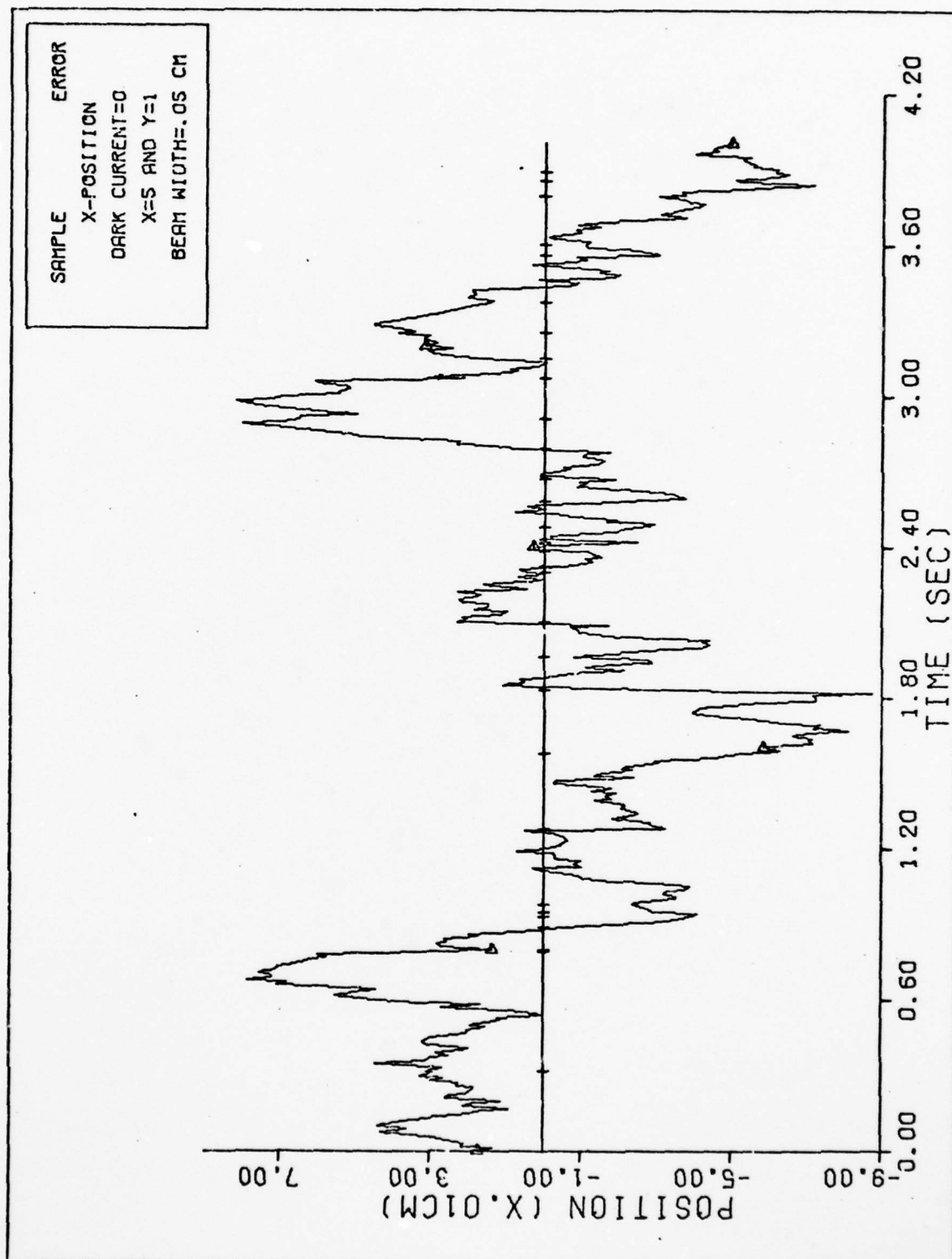


Figure 13a X-POSITION



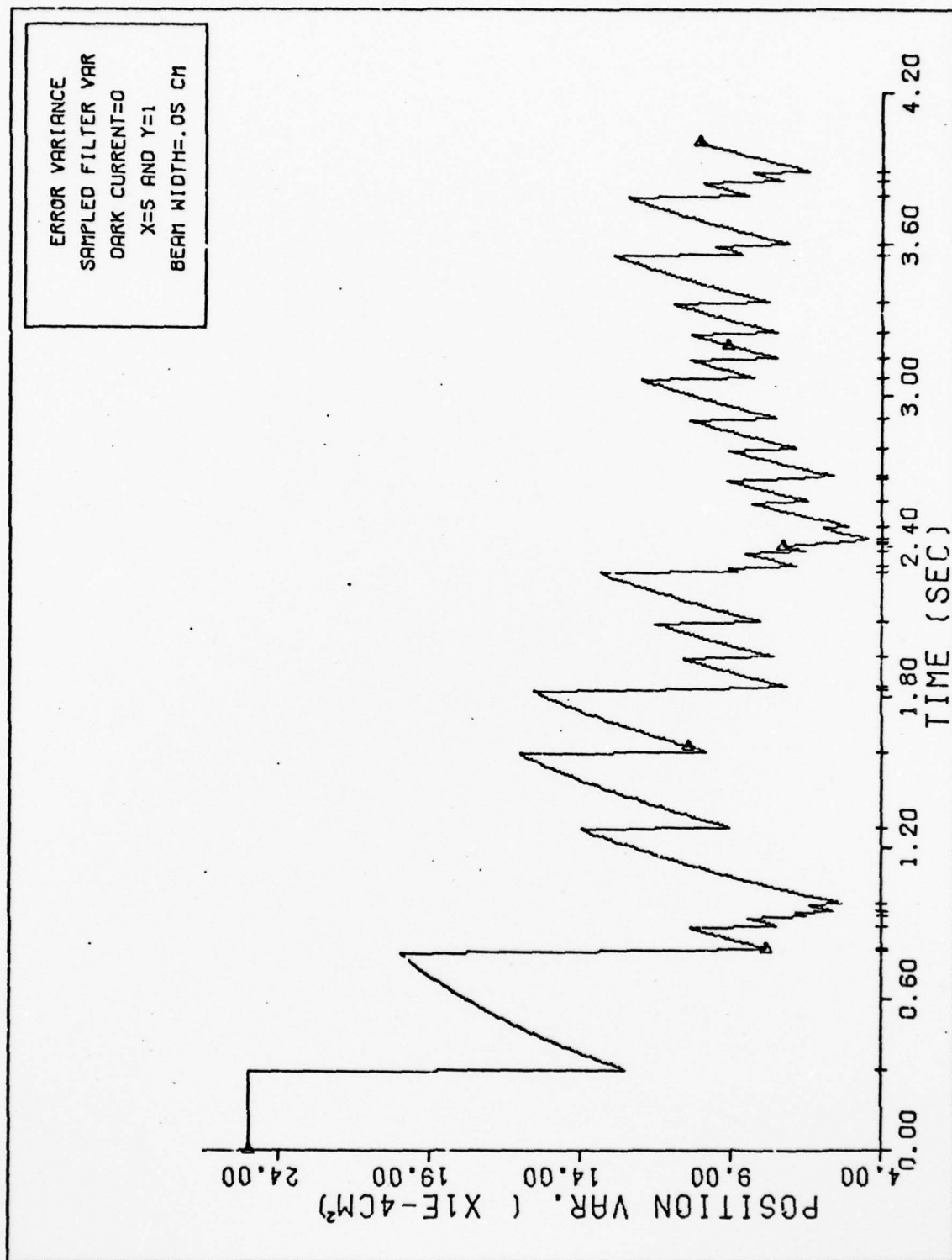


Figure 13b X-POSITION FILTER VARIANCE

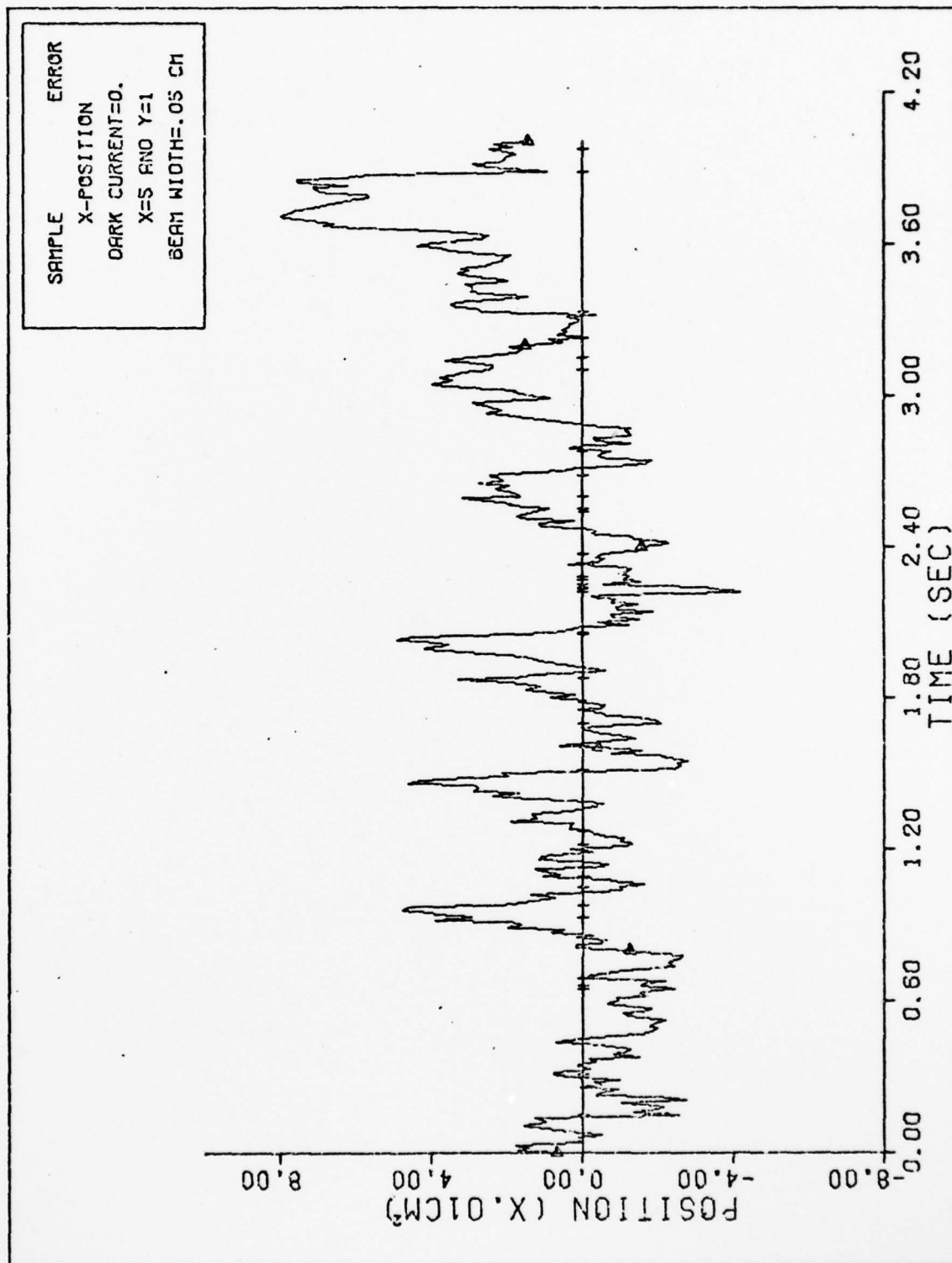


Figure 14a X-POSITION

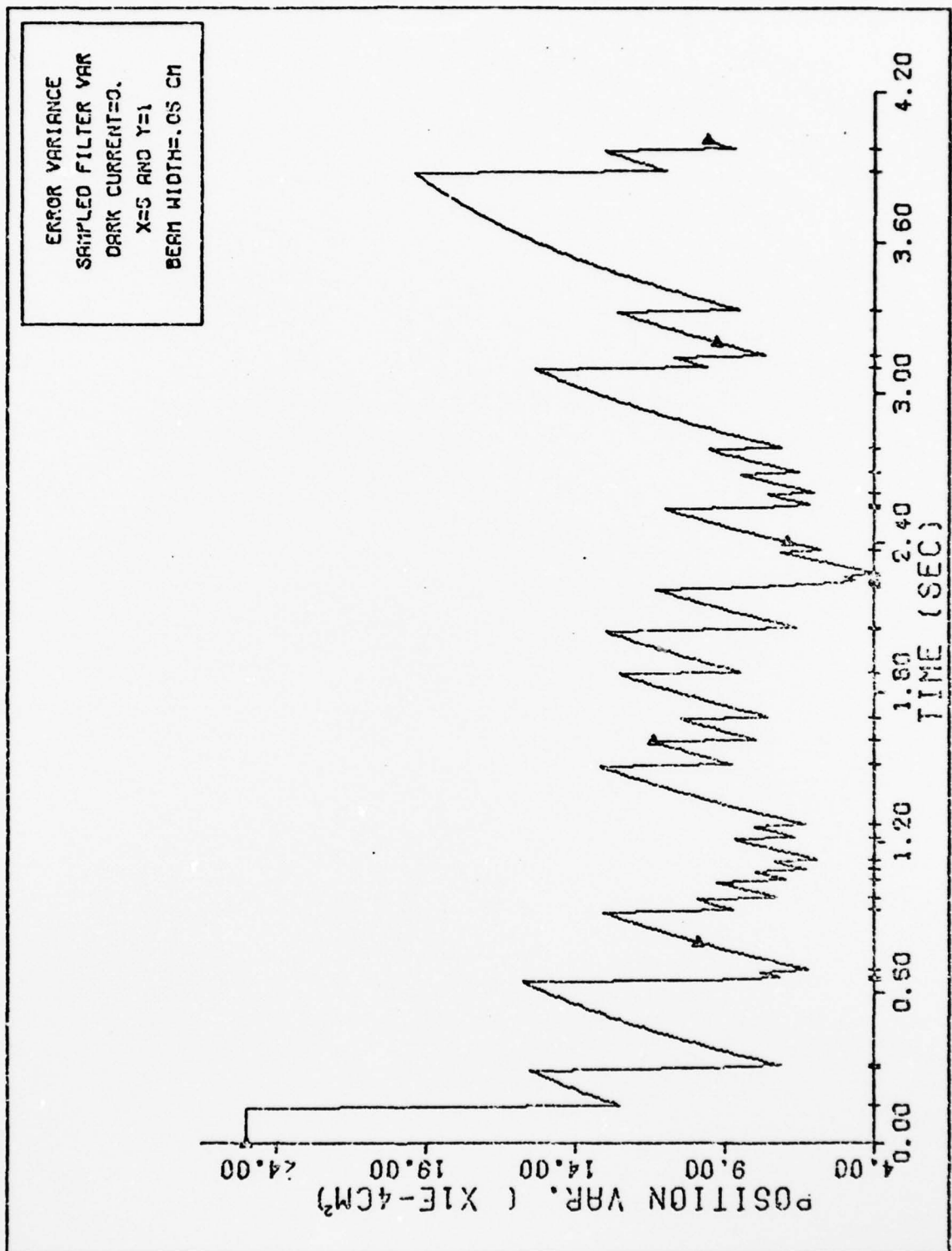


Figure 14b X-POSITION FILTER VARIANCE

a smaller filter growth in the variance, and the next measurement will have a lower weighting.

For this research, the coherence time,  $\tau_c$ , of the spot is one second; for  $X=5$ , the term  $\frac{nI_0}{nf_0}\sqrt{2\pi}\sigma$  in Eq. (63) is equal to 10 events per second. This is the average rate function of the Gaussian spot, after integrating  $\lambda_g(t,r)$ , defined in Eq. (14), over the detector length which approximates an infinite detector length with respect to the Gaussian beam. It is well known for a poisson process that the mean and variance of the counting process  $N(t)$ , defined in Appendix A, are respectively  $E[N(t)] = \iint_0^T \lambda(\alpha,\beta) d\alpha d\beta$  and  $VAR[N(t)] = \iint_0^T \lambda(\alpha,\beta) d\alpha d\beta$ . It then follows for  $T=4$  that  $\lambda_g(t,r)$  can be expressed as

$$\begin{aligned} \lambda_g(t,r) &= \left[ \frac{nI_0}{nf_0}\sqrt{2\pi}\sigma \right] \left[ \frac{1}{\sqrt{2\pi}\sigma} \exp\left(\frac{-(r-x(t))^2}{2\sigma^2}\right) \right] \\ &= \frac{10}{\sqrt{2\pi}\sigma} \exp\left(\frac{-(r-x(t))^2}{2\sigma^2}\right) \end{aligned} \quad (64)$$

so that  $E[N(t)]=40$  events with standard deviation of 6.3 events. In Figs. (13) and (14), the number of events for this particular case are 34 and 36 events, respectively. Also, in these sample runs, simultaneous events did not occur. To the second moment level, these results indicate some validity in the Binomial Method in generating the point process observations in time and space.

Finally, the test cases for this method are plotted in Figs. (15) through (17); note the different scales on each plot. As expected, increasing  $Y$  (the spot's jitter normalized

AD-A064 737

AIR FORCE INST OF TECH WRIGHT-PATTERSON AFB OHIO SCH--ETC F/G 17/8  
FUNDAMENTAL LIMITATIONS OF OPTICAL TRACKERS.(U)

DEC 78 J M SANTIAGO

AFIT/GEO/EE/78-4

UNCLASSIFIED

NL

2 OF 2  
AD  
AO 64737

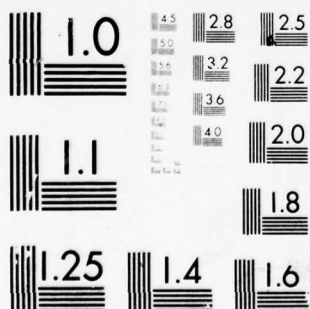


END  
DATE  
FILMED

4-79  
DDC



6473



MICROCOPY RESOLUTION TEST CHART  
NATIONAL BUREAU OF STANDARDS-1963-A

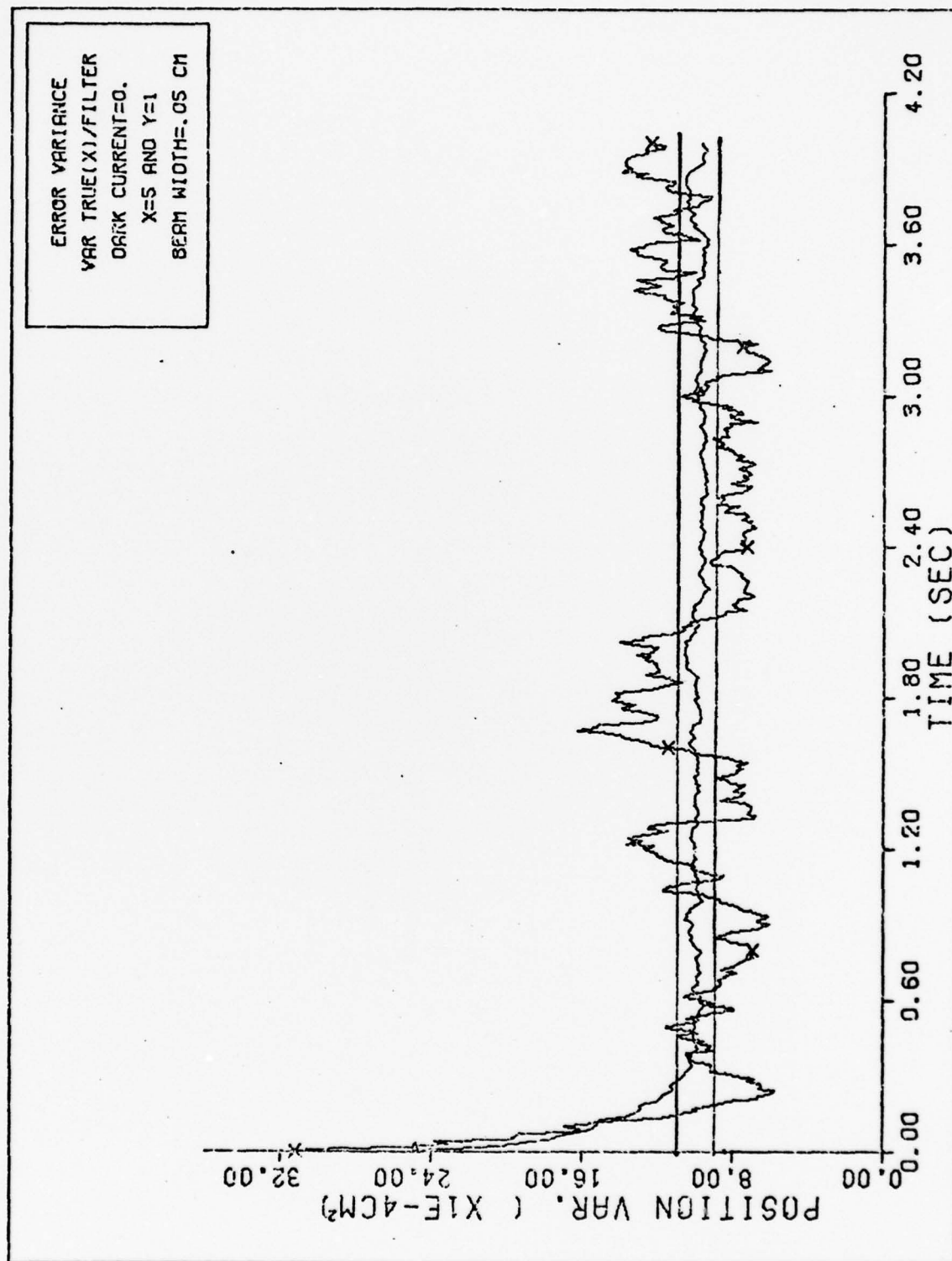


Figure 15 X-POSITION VARIANCES

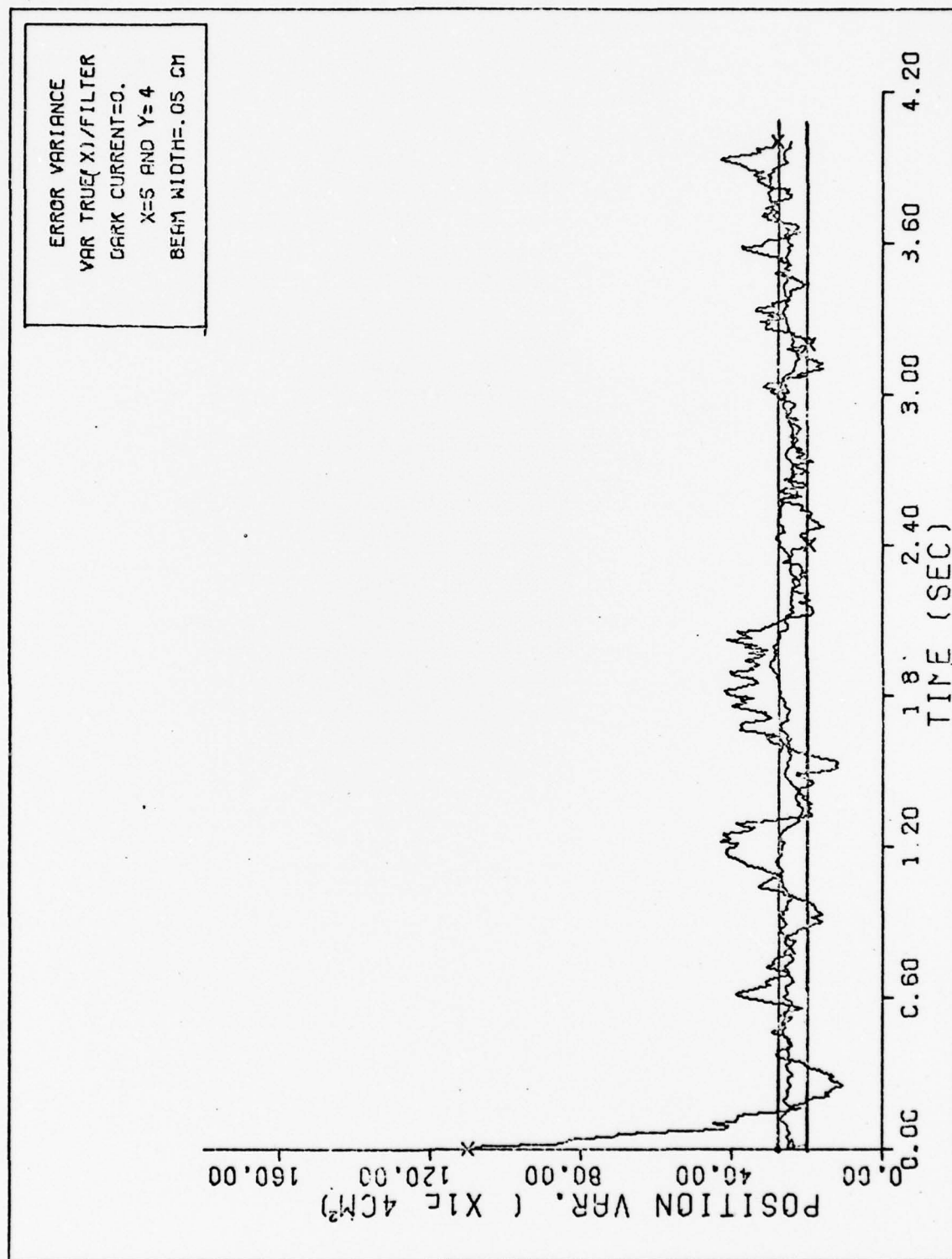


Figure 16 X-POSITION VARIANCES

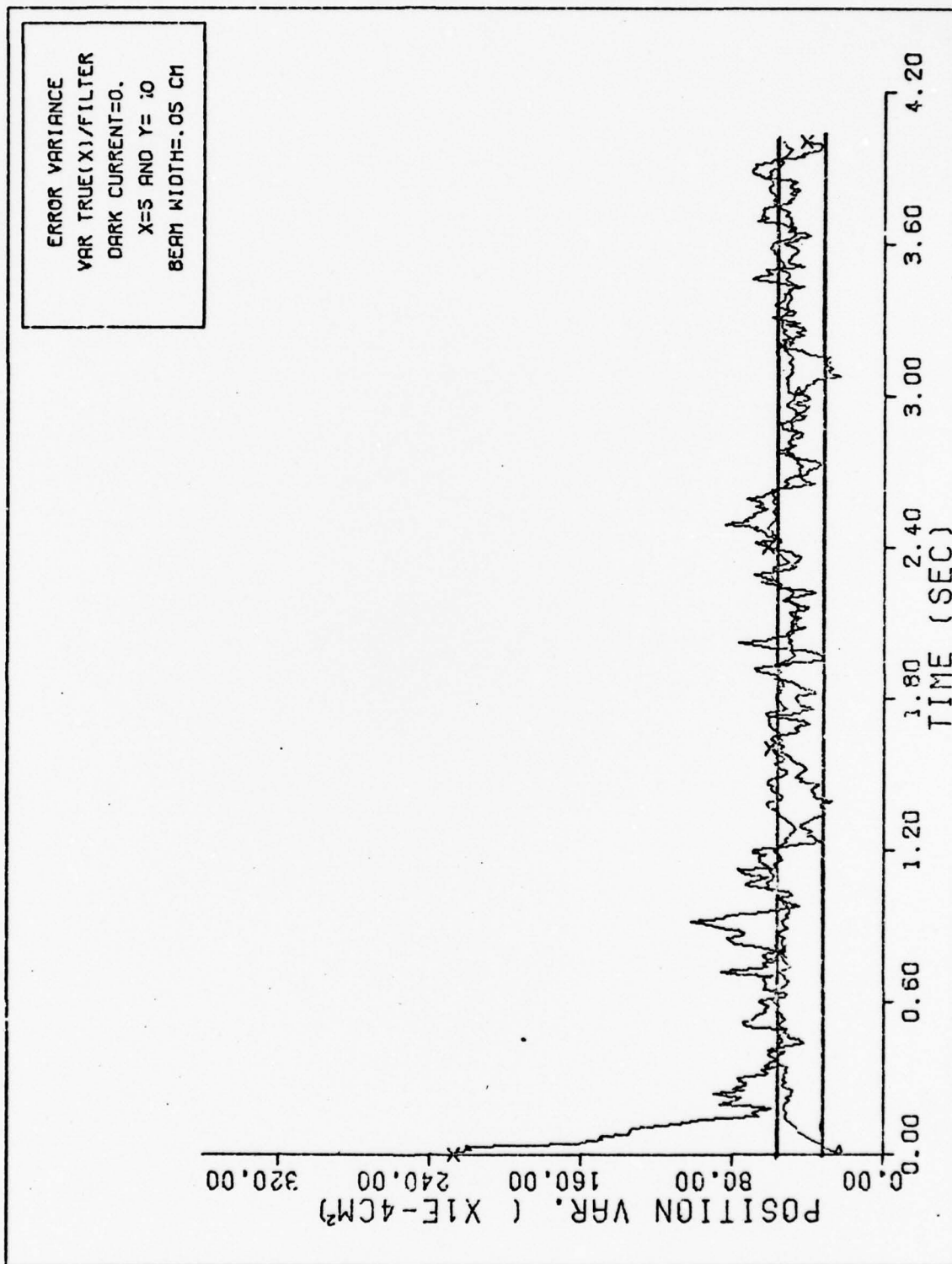


Figure 17 X-POSITION VARIANCES

by the square of the beam width) increases the error variances - implying poorer performance. Even when the filter is initialized with its state estimate not equal to the true position of maximum intensity (i.e., initialize from non-zero initial conditions), the plot in Fig. (18) shows that the error process is zero-mean. This is expected since the conditional estimate of  $\hat{x}(t)$  is unbiased and  $x(t)$  has zero mean.

#### Conditional Method (without dark current)

Shown in Fig. (19) is a sample of the error process and the filter variance generated by the Snyder Filter for the set of parameters,  $X=20$  and  $Y=1$ . From these plots, it is evident that the measurements of event locations at the event times are important in minimizing the filter's error and uncertainty. As shown in Fig. (19a), the errors are within one beam width; and in Fig. (19b), there is little filter variance growth as events appear frequently in time (as seen in the Binomial Method).

For the test cases in Table 2, it is desirable to choose values of the sample and average filter variances at selected time points. For each case, these variance points are plotted with the upper and lower bound curves. However, it was noted earlier that there are fluctuations in the variances which make it difficult to select these points. A "time-average" technique is used to select and to plot these points easily. This technique is depicted in Fig. (20). In this case, a fixed time interval, that is chosen to be much greater than the sample period, contains time points that are equally spaced. Corresponding



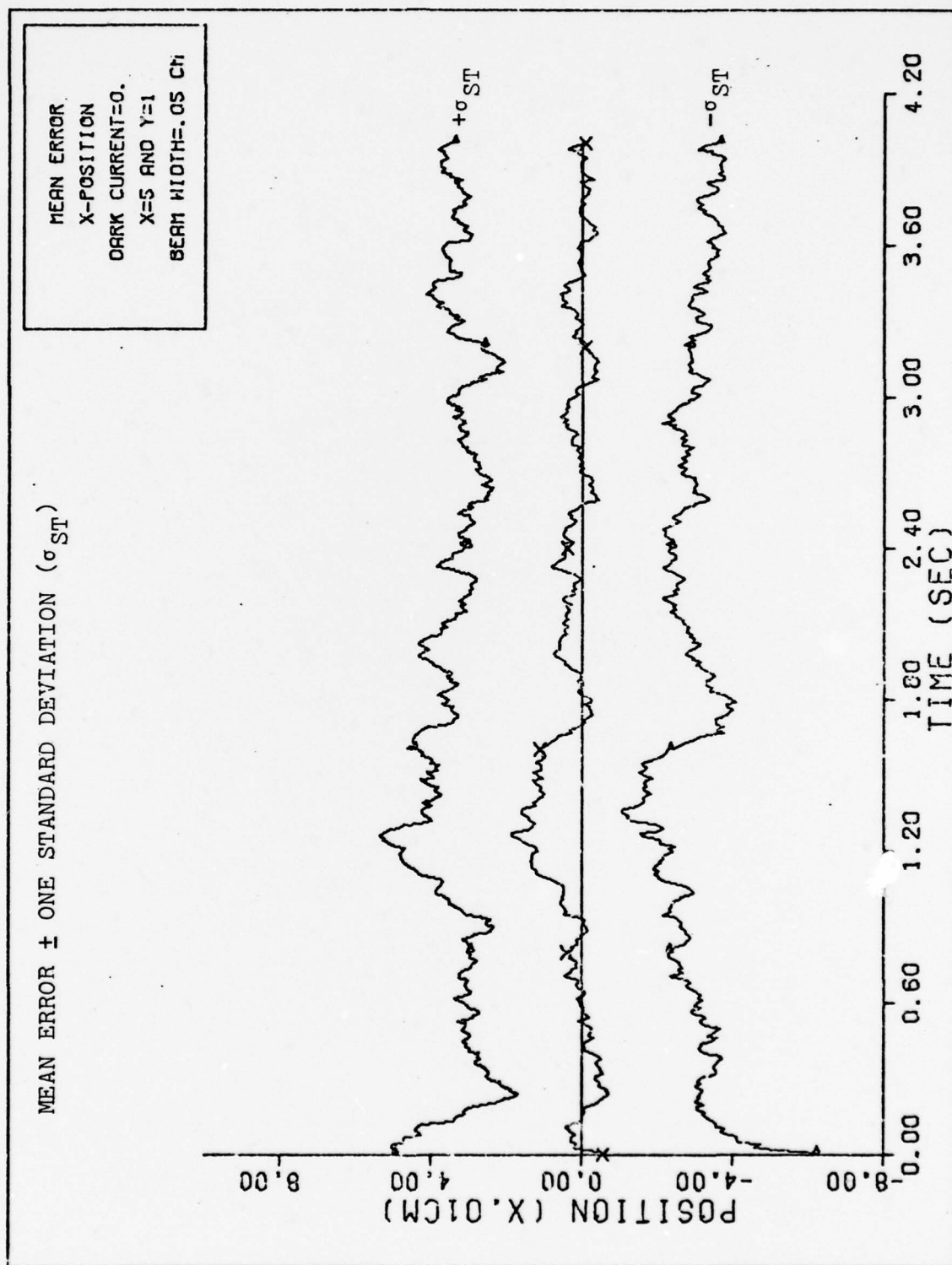


Figure 18 X-POSITION

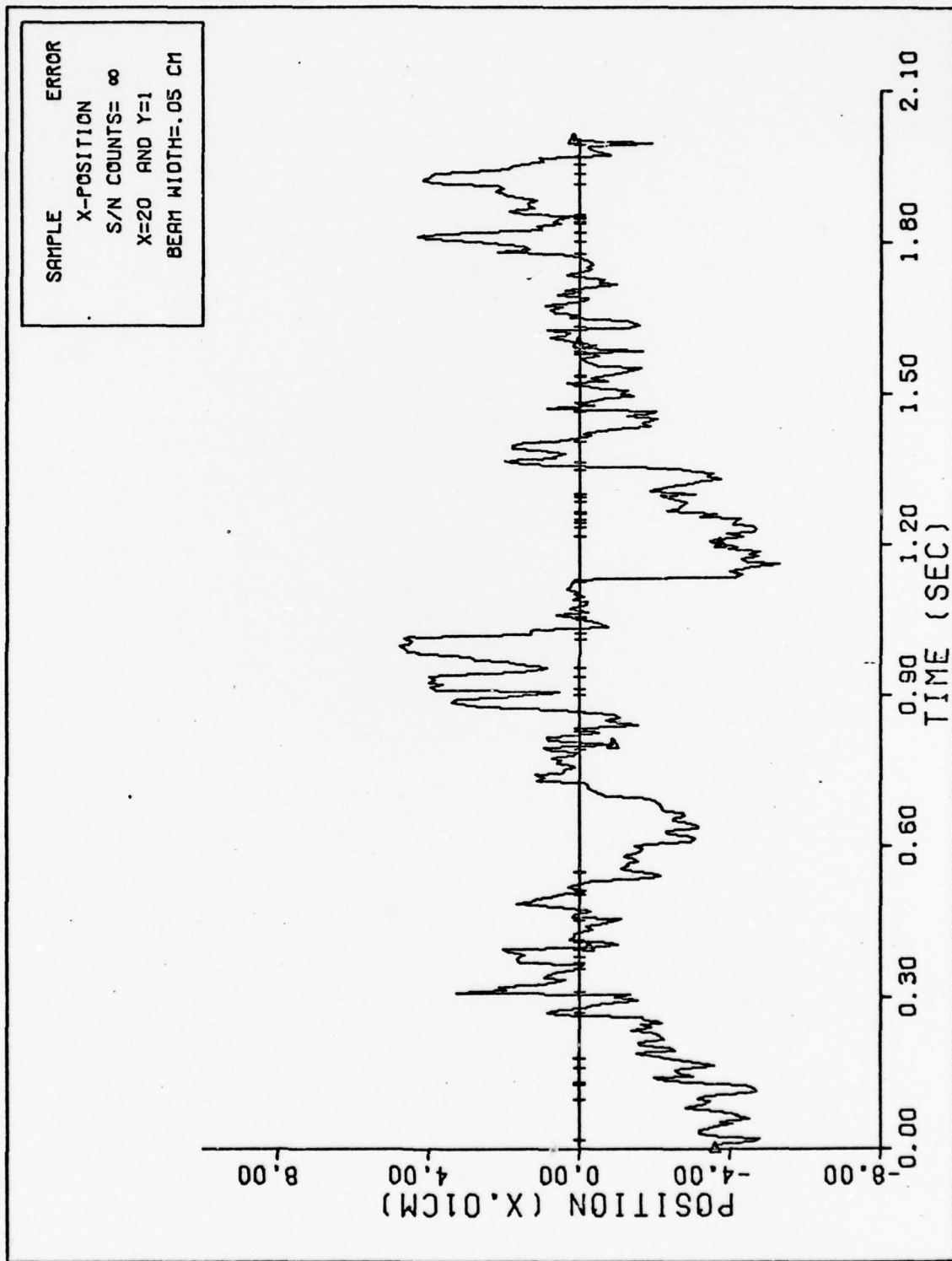


Figure 19a X-POSITION

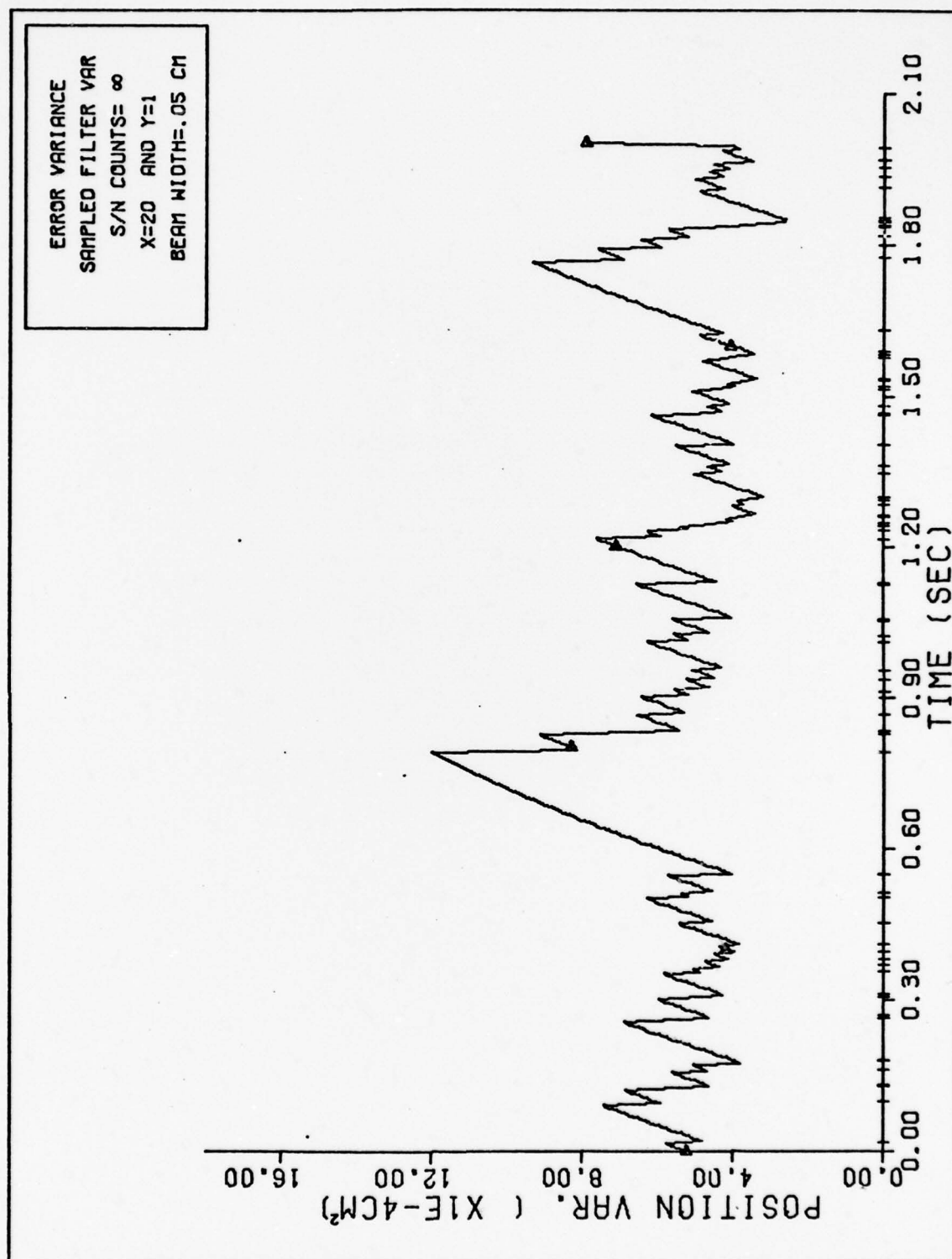


Figure 19b X-POSITION FILTER VARIANCE

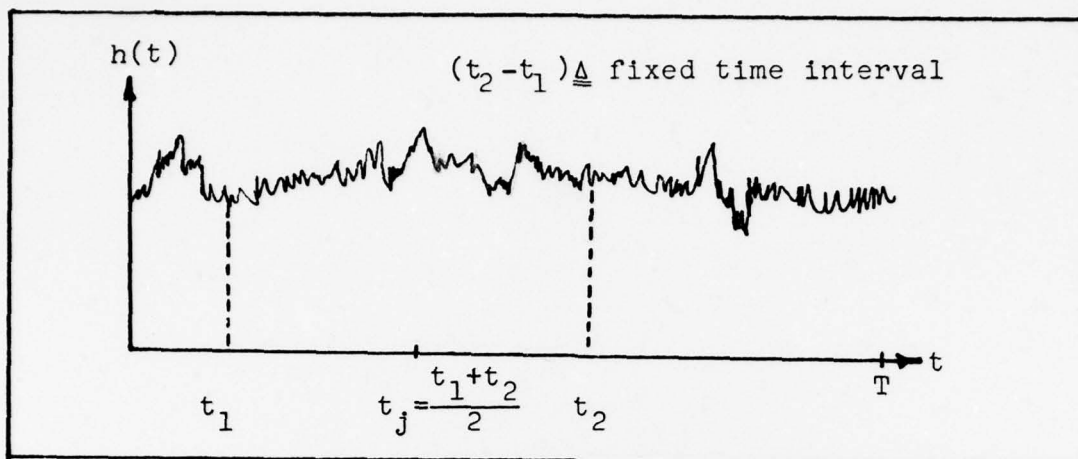


Figure 20 "Time-average" Technique ( $h(t)$  denotes time history of either true or filter variance calculated from sample statistics)

to each time point are the values of the variances. These values are then summed, and the resulting sum is divided by the number of points in that fixed interval. This final value will then be used to denote the value of the variance at the midpoint of the fixed time interval. This time interval "runs" across the time axis to calculate these "time-average" values until the end of the observation time,  $T$ .

With this technique, the sample and average filter variances are listed in Table 3 at the time point,  $t_j = 1.5$  second. These values are plotted with the upper and lower bound curves in Figs. (21). The time point,  $t_j = 1.5$  second, is chosen after examining the plots, similar to plots in Fig. (22), for each case which indicates steady-state is reached. Note that the values of the true and filter variances are close to the upper bounds, which seems reasonable, since the values of  $X=1$ ,  $X=5$ ,  $Y=1$ , and  $Y=5$  are relatively poor conditions for good tracking performance.

Performance Parameter		Normalized Bounds on MSE		Normalized Simulation Values	
X	Y	$\frac{P^*}{\sigma^2}$	$\frac{P^*}{\sigma^2}$	True Variance	Filter Variance
5.0	0.5	0.232	0.250	0.233	0.251
5.0	1.0	0.358	0.408	0.388	0.406
5.0	5.0	0.905	1.305	1.340	1.270
5.0	10.0	1.320	2.240	2.370	2.180
1.0	0.5	0.366	0.390	0.340	0.389
1.0	1.0	0.618	0.707	0.621	0.703
1.0	5.0	1.790	2.870	2.570	2.845
1.0	10.0	2.900	5.420	4.900	5.380
0.5	5.0	2.320	3.590	4.200	3.490
10.0	5.0	0.659	0.880	0.935	0.854
15.0	5.0	0.545	0.698	0.670	0.654
20.0	5.0	0.496	0.542	0.592	0.558
0.5	1.0	0.732	0.816	0.898	0.803
10.0	1.0	0.270	0.302	0.319	0.298
15.0	1.0	0.227	0.250	0.243	0.242
20.0	1.0	0.200	0.218	0.222	0.212

Table 3. Test Cases for Conditional Method  
(without dark current)



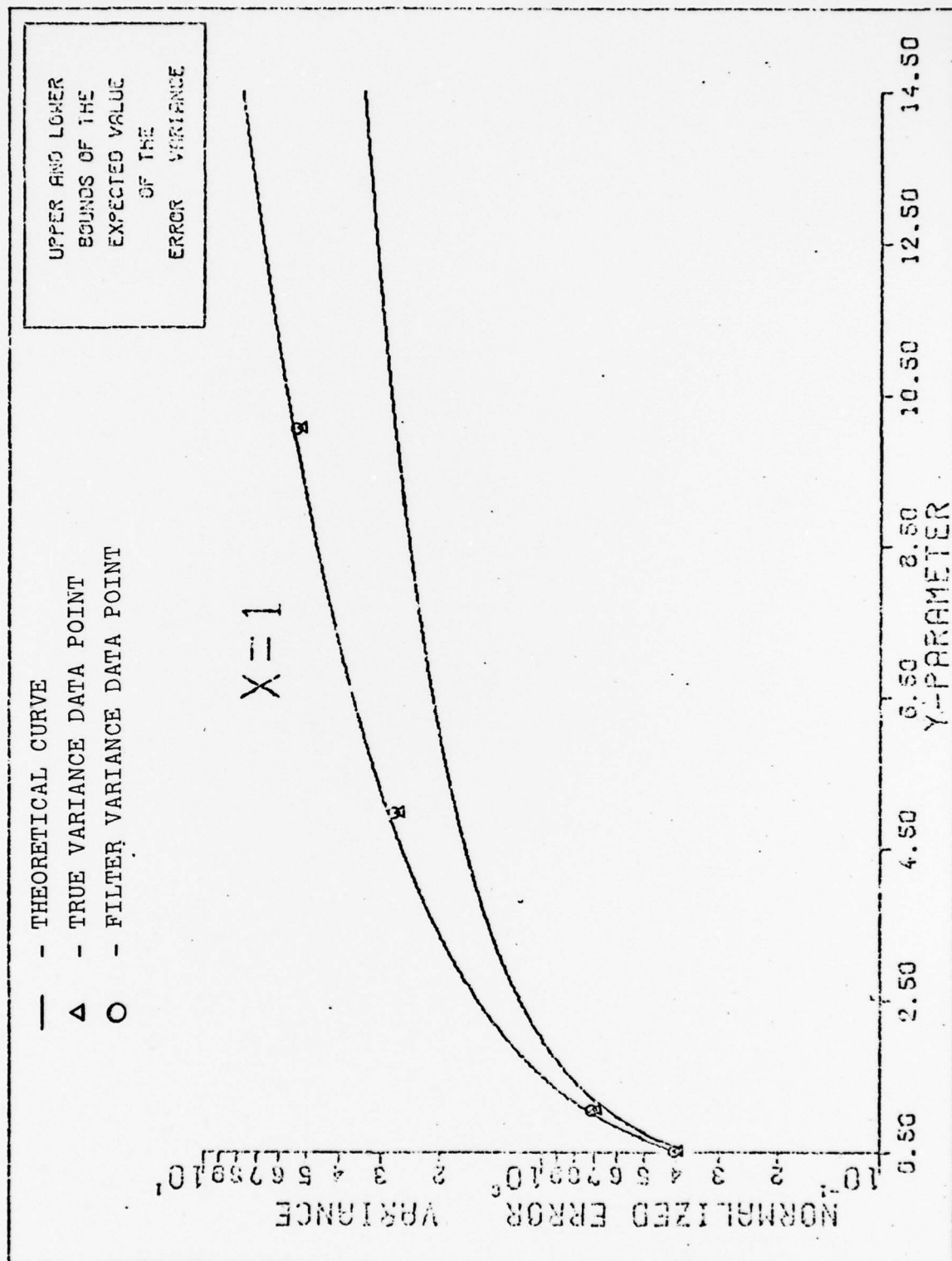


Figure 21a Simulation Values of True and Filter Variances

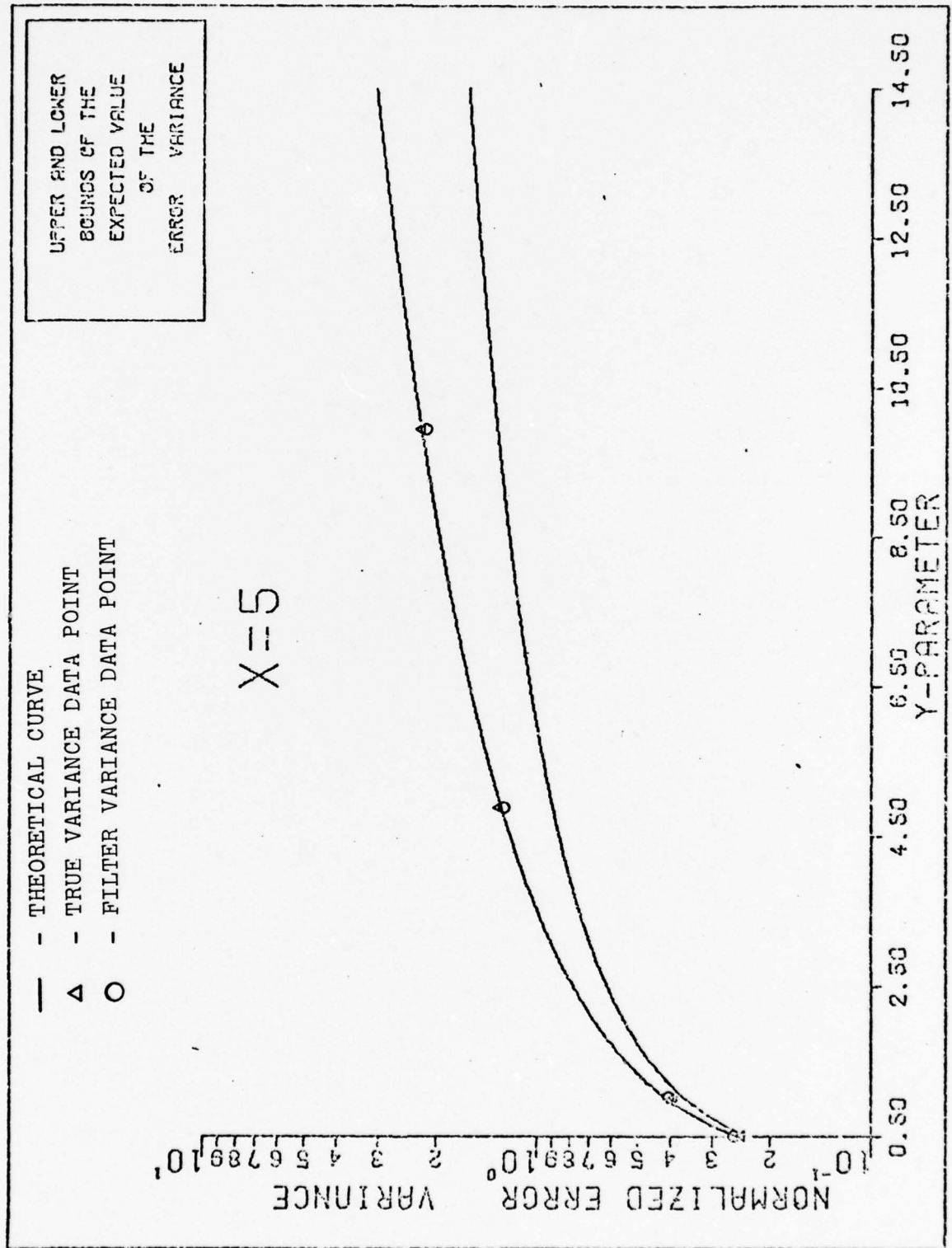


Figure 21b Simulation Values of True and Filter Variances

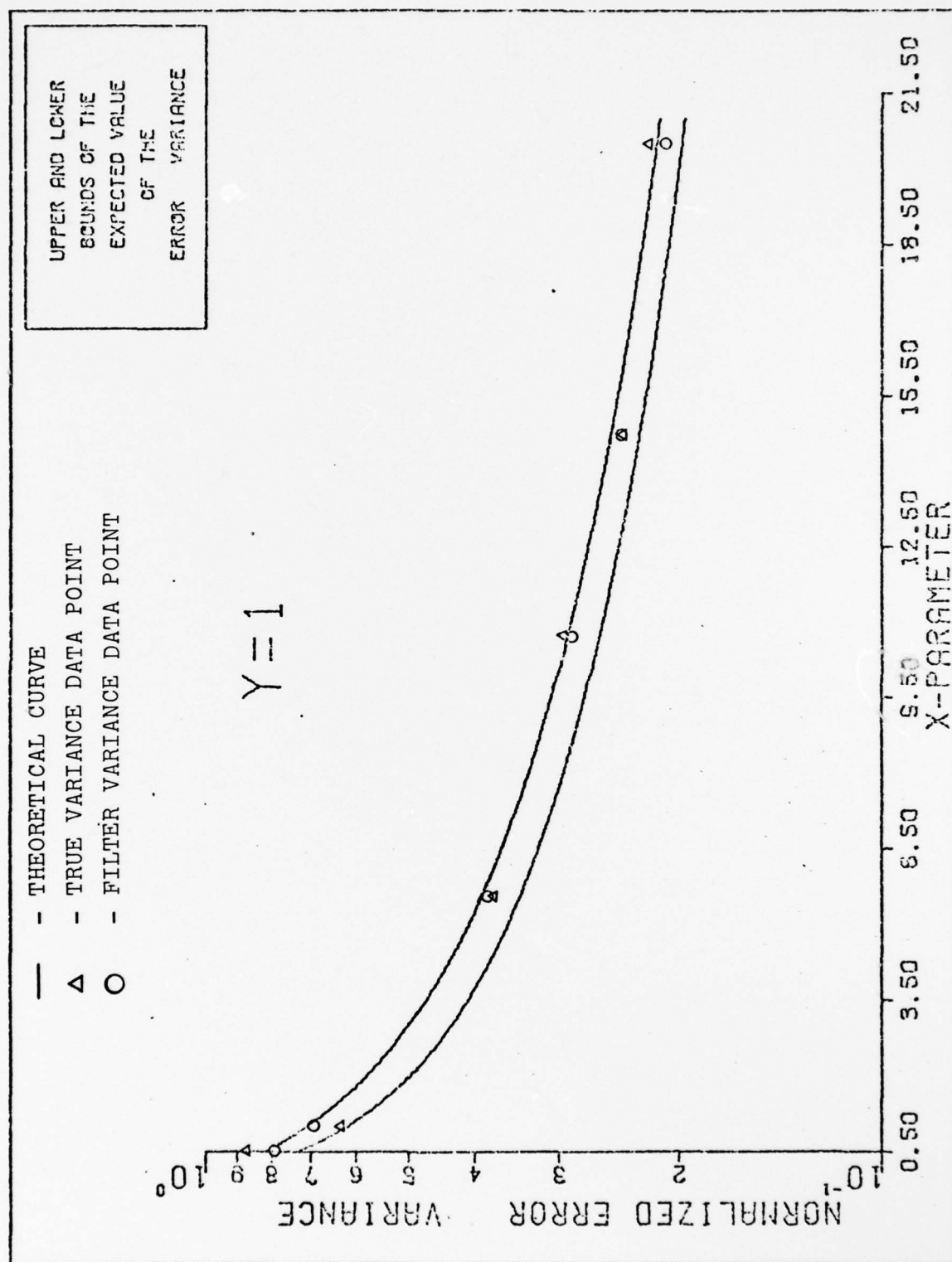


Figure 21c Simulation Values of True and Filter Variances

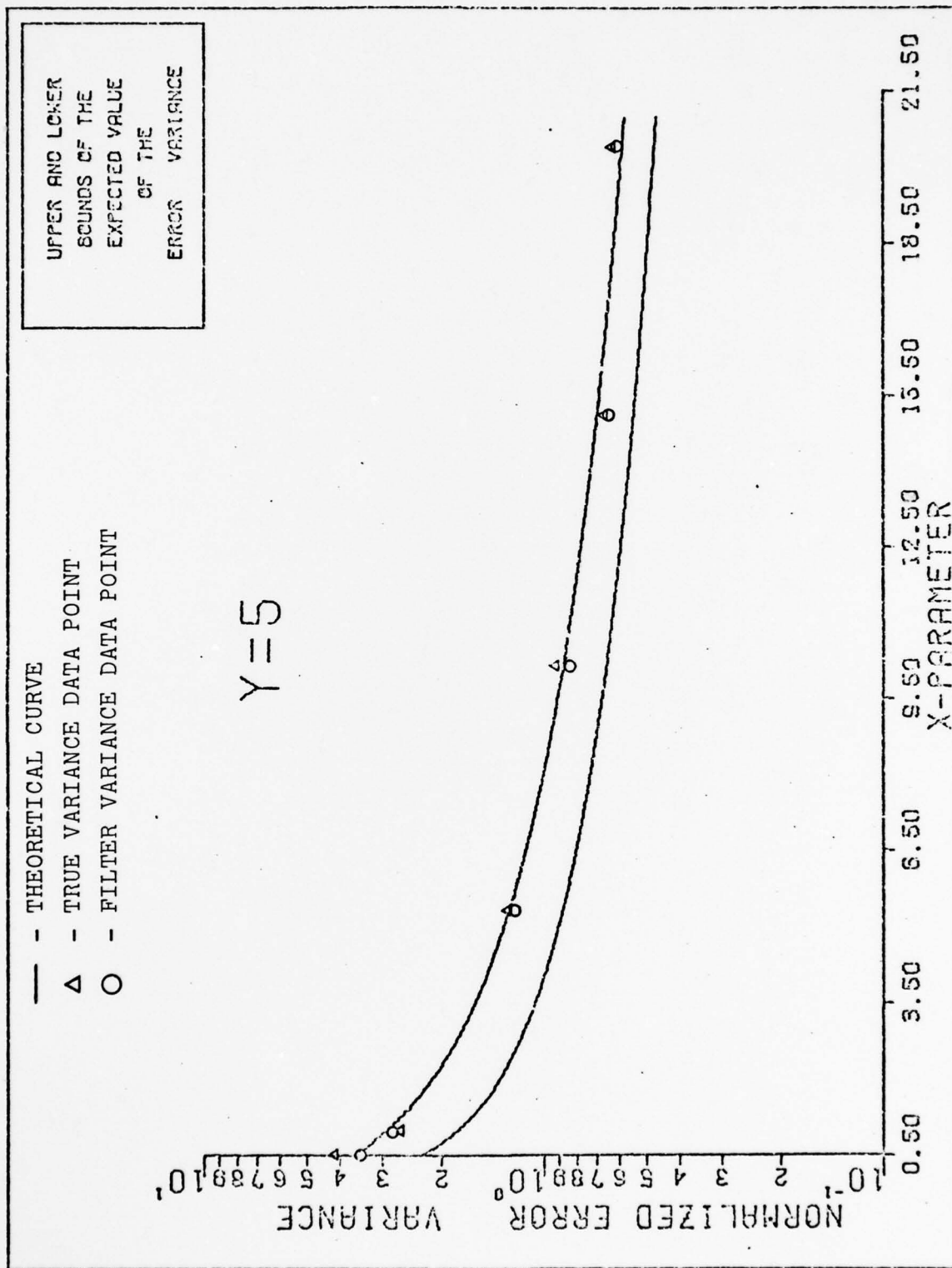


Figure 21d Simulation Values of True and Filter Variances

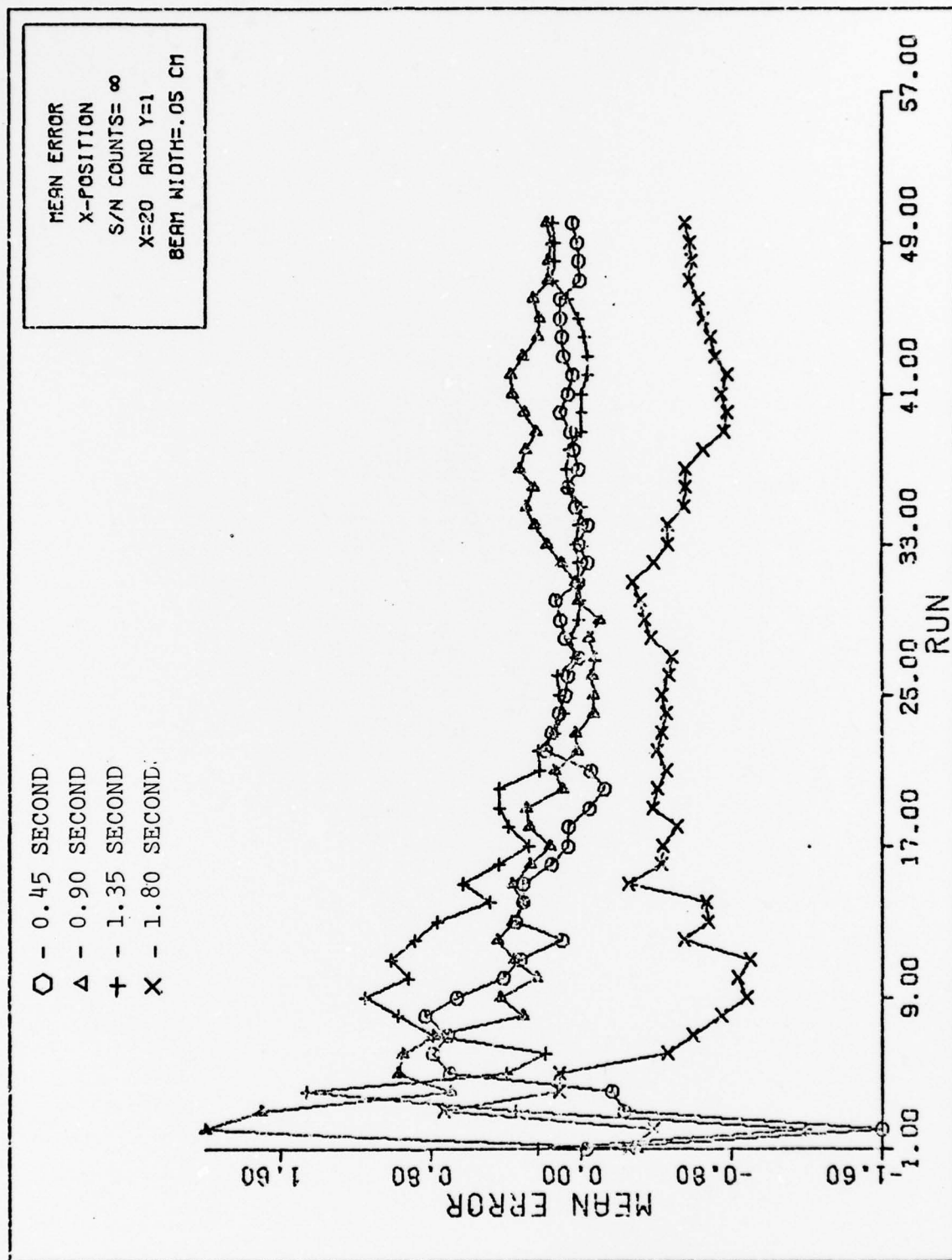


Figure 22a MEAN CONVERGENCE



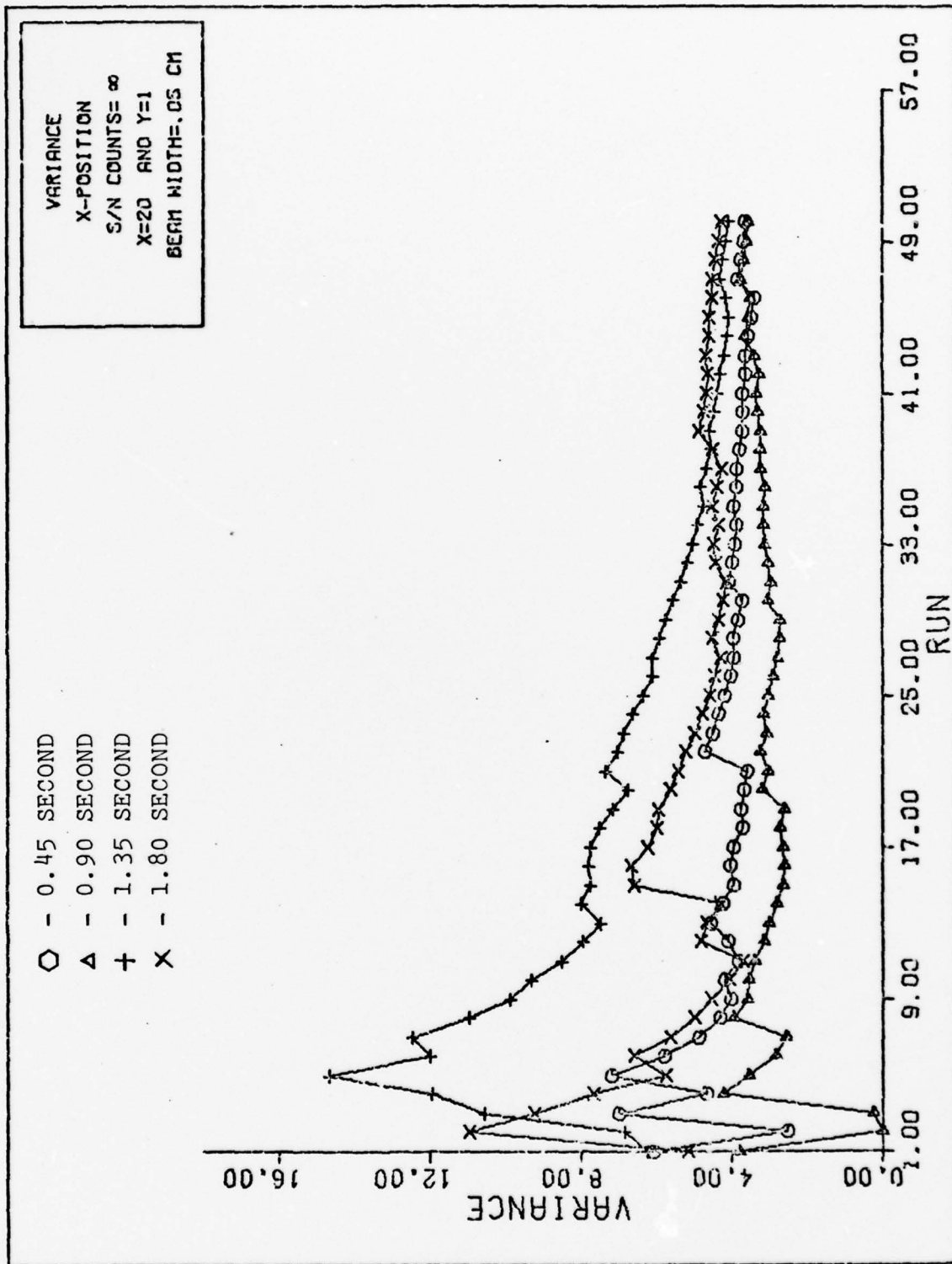


Figure 22b VARIANCE CONVERGENCE

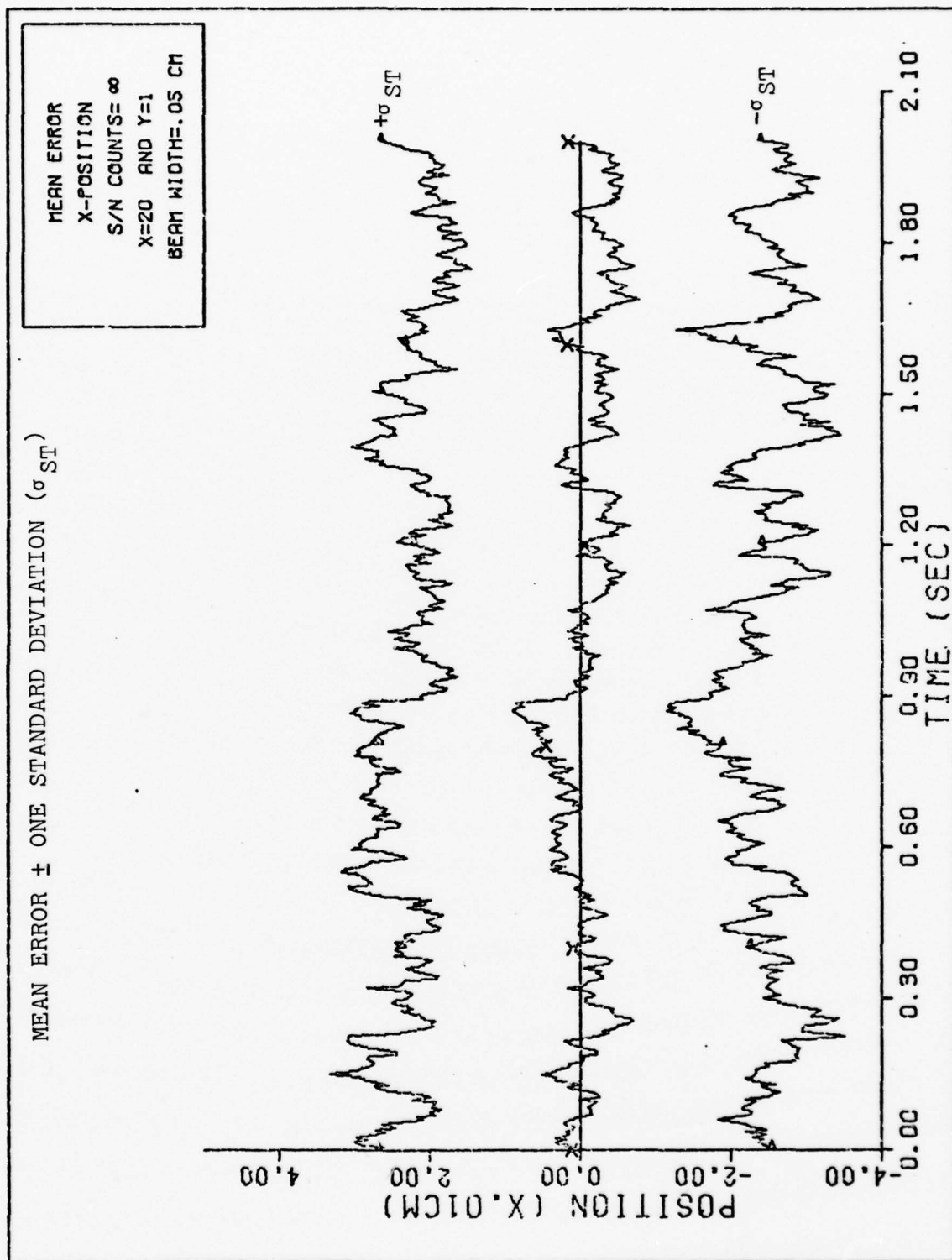


Figure 22c X-POSITION

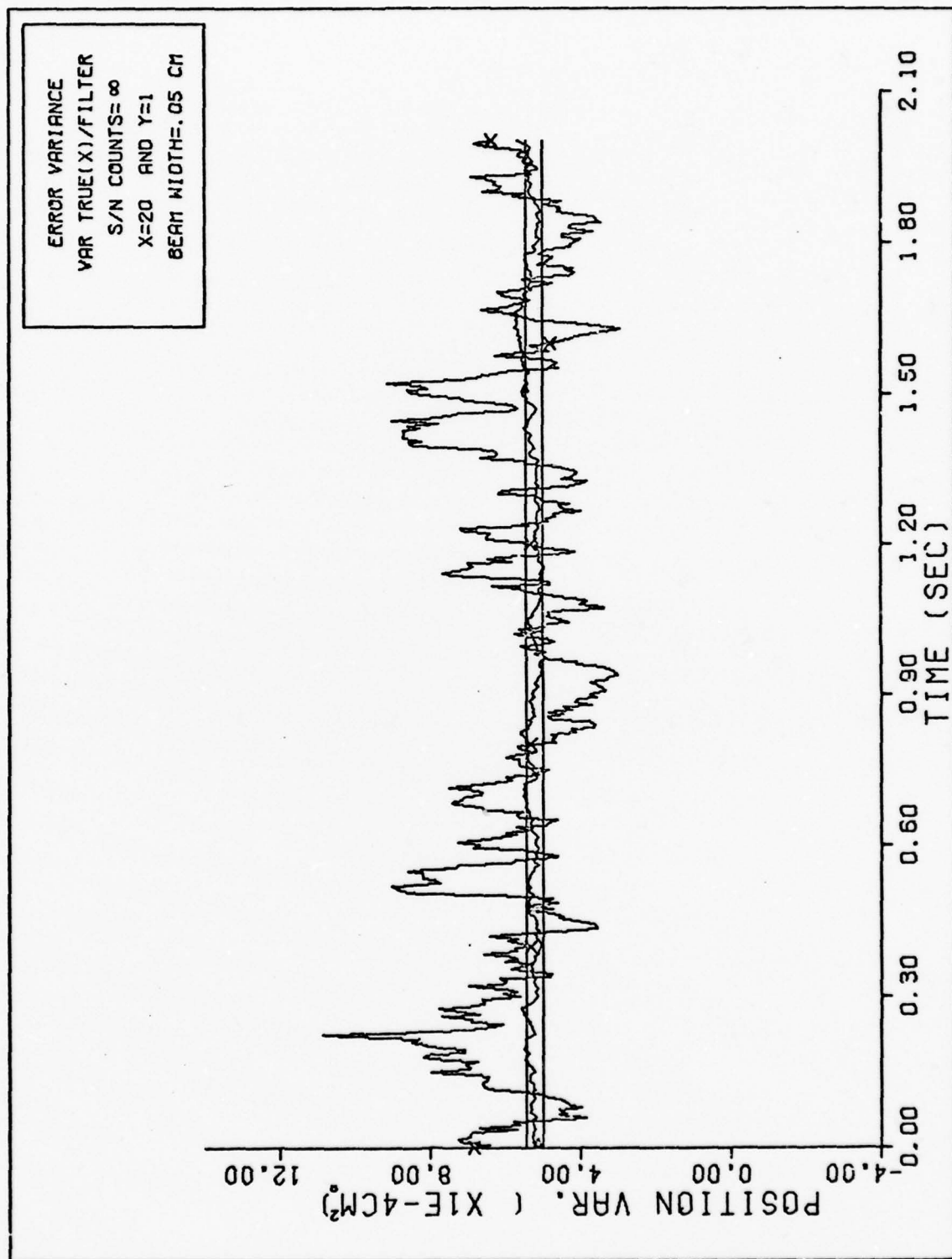


Figure 22d X-POSITION VARIANCES

That is, these results indicate that actual performance can be described by the upper bound on MSE.

Two issues should be of concern when plotting these values. One is that the filter performance must be in steady state, and the other is that the number of sample runs in the simulation must be large enough to yield some confidence of inferring information from the error variance generated by either sample statistics or averaging of filter outputs. Hence, a particular case is chosen to extend the simulation time to 40 seconds; the results in Fig. (23) indicate that steady state is reached in one second. Then the issue again is of confidence in the values of the true variances which can be increased by performing more simulation runs; because of time constraints, fifty simulations remain unchanged. To illustrate that the number of simulation runs is not appropriate in all cases, refer to plots in Fig. (22). For this particular case,  $X=20$  and  $Y=1$ , the mean error is not converging to a definite value.

In summary, it appears that the upper bound describes the actual performance of the Snyder Filter for few signal counts per coherence time.

#### Conditional Method (with dark current)

Particular cases were selected to examine the effects of dark current and to determine the filter's sensitivity in performance as it processes these noise measurements. The results of this analysis is that, for average signal-to-noise counts ratio of 500, the filter was very sensitive to dark distributed measurements. The results are plotted in Figs. (24) through

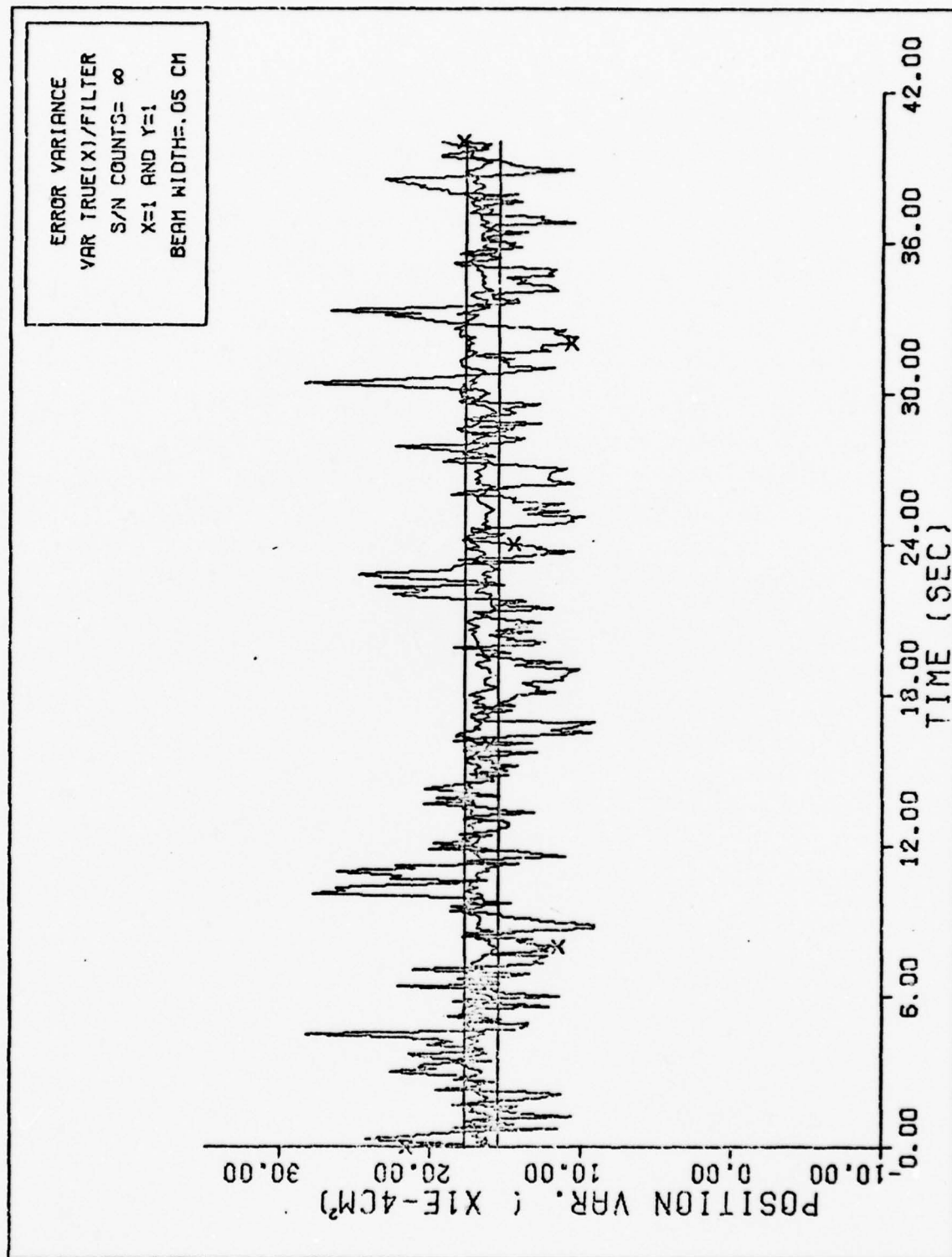


Figure 23a X-POSITION VARIANCES



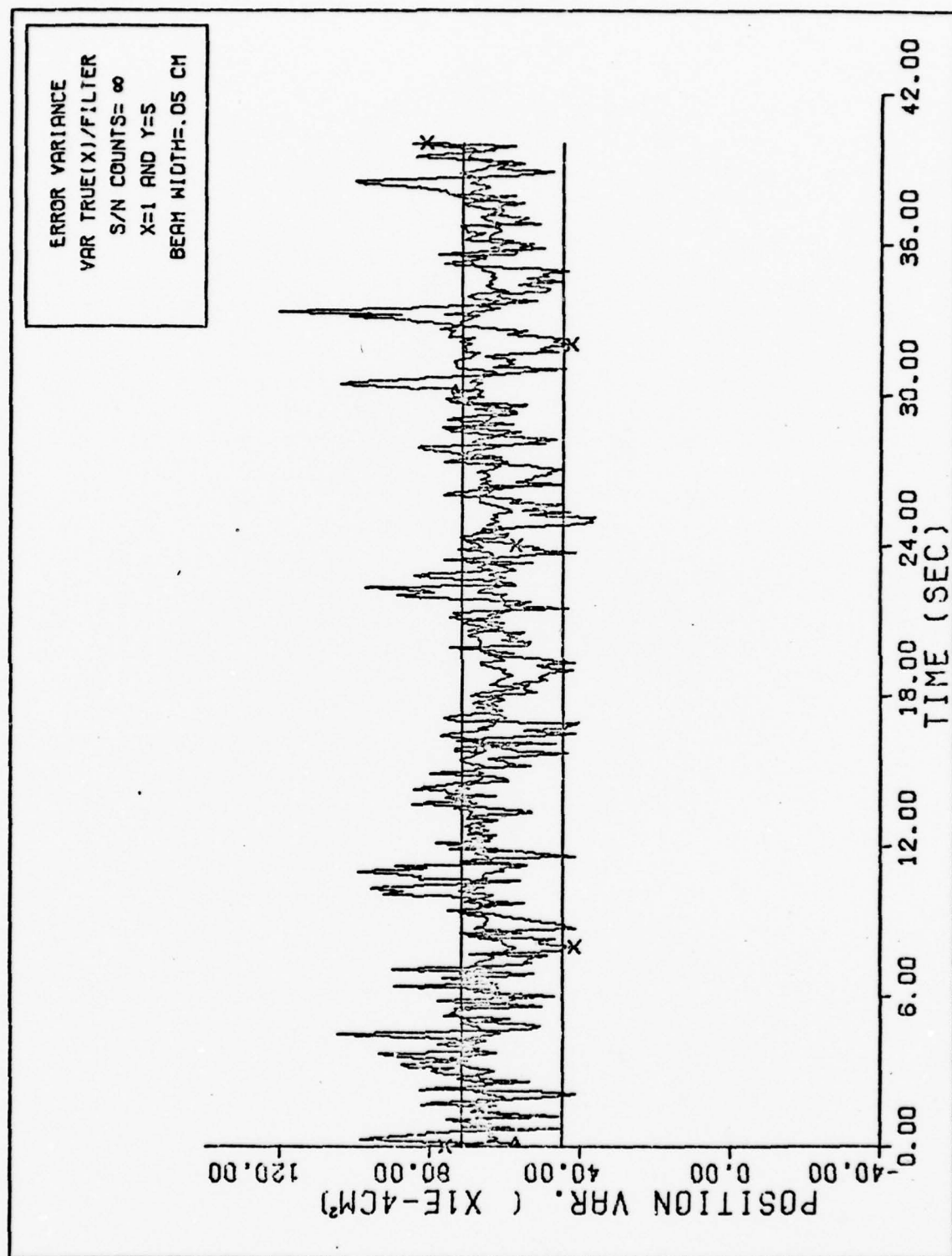


Figure 23b X-POSITION VARIANCES

(28) for different cases, as indicated by the figures. From these plots, it is clearly shown that the filter performs poorly if it processes even one dark measurement. Note that the plots in these figures are not close to ensemble average statistics. That is, to obtain the sample variance, it will require a substantial amount of additional sample runs. Again, the confidence in the sample statistics is an issue. On the other hand, these results do provide insight into the sensitivity of the Snyder Filter to dark measurements. However, to evaluate individual effects of dark current, Figs. (24a, 24b), (25a, 25b), (26a, 26b), and (28a, 28b) are used to determine which sample runs contain dark measurements. Thus, Figs. (29a, 30a, 31a, 32a) and (29b, 30b, 31b, 32b) are plots of the sample errors and sample filter variance, respectively. Figs. (29) and (30) are for average signal-to-noise counts ratio of 500 and 50, respectively, for  $X=5$  and  $Y=1$ . Similarly, Figs. (31) and (32) are for average signal-to-noise counts ratio of 500 and 5, respectively, for  $X=20$  and  $Y=1$ . These results clearly show that the Snyder Filter is very sensitive to dark measurements. Thus, the Snyder Filter cannot distinguish between a dark or signal measurement (i.e., it treats all events as signal).

To enhance filter performance, filter-tuning (in this case, increasing the beam-width) and residual monitoring were considered. In filter tuning, the beam width is increased, which corresponds to weighing the measurements less heavily from the photodetector surface. In other words, the filter is having less confidence in its measurements. Conversely, if

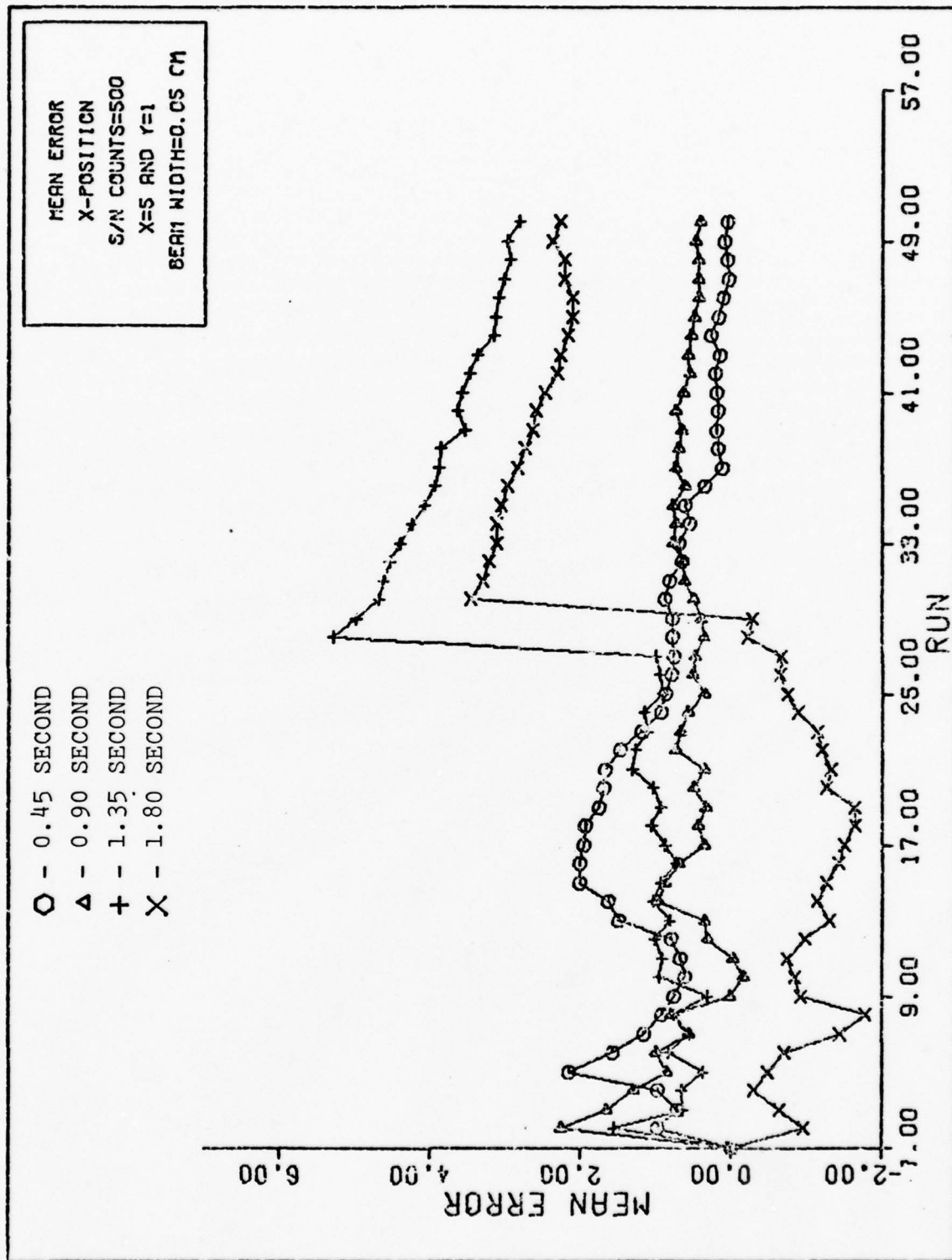


Figure 24a MEAN CONVERGENCE

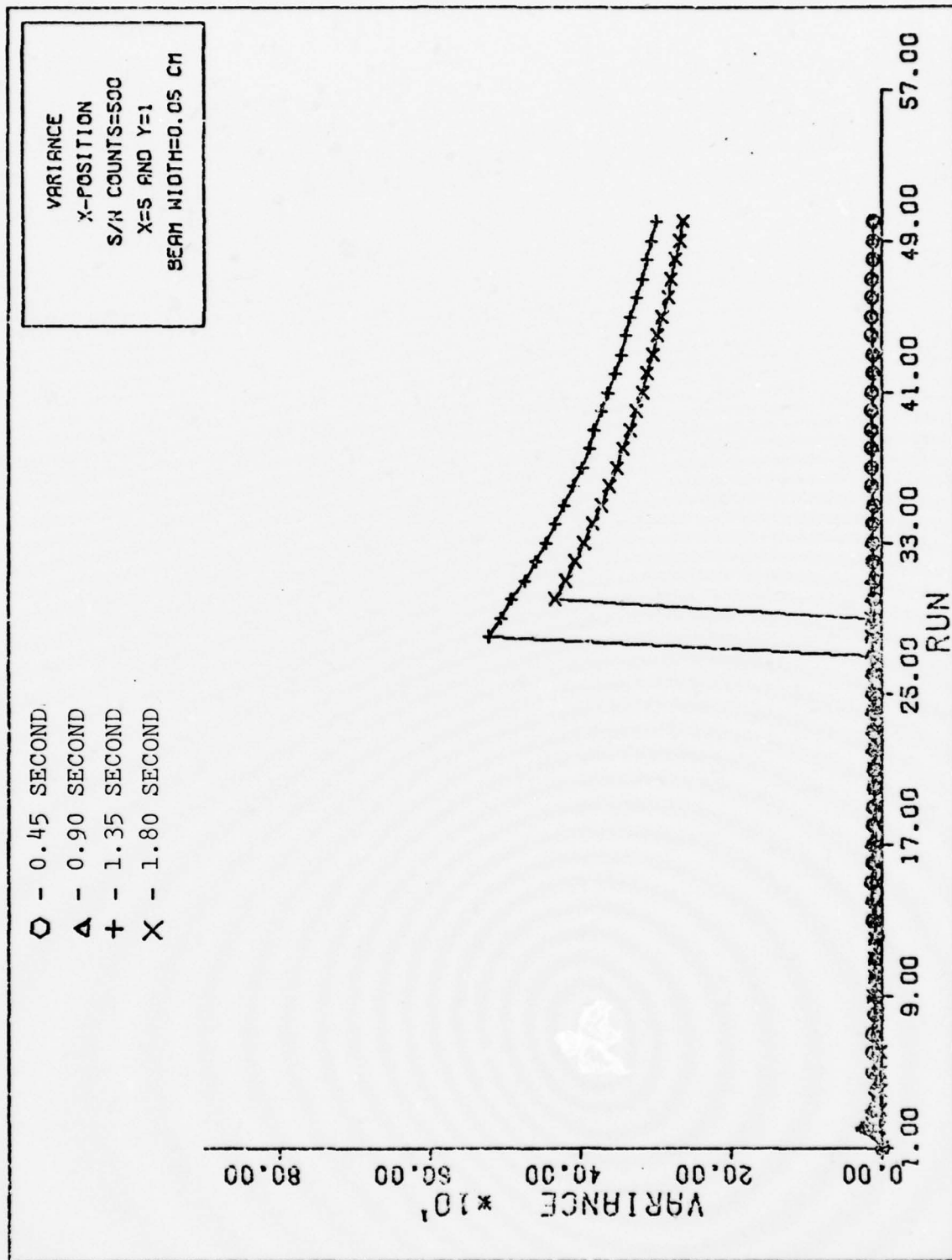


Figure 24b VARIANCE CONVERGENCE

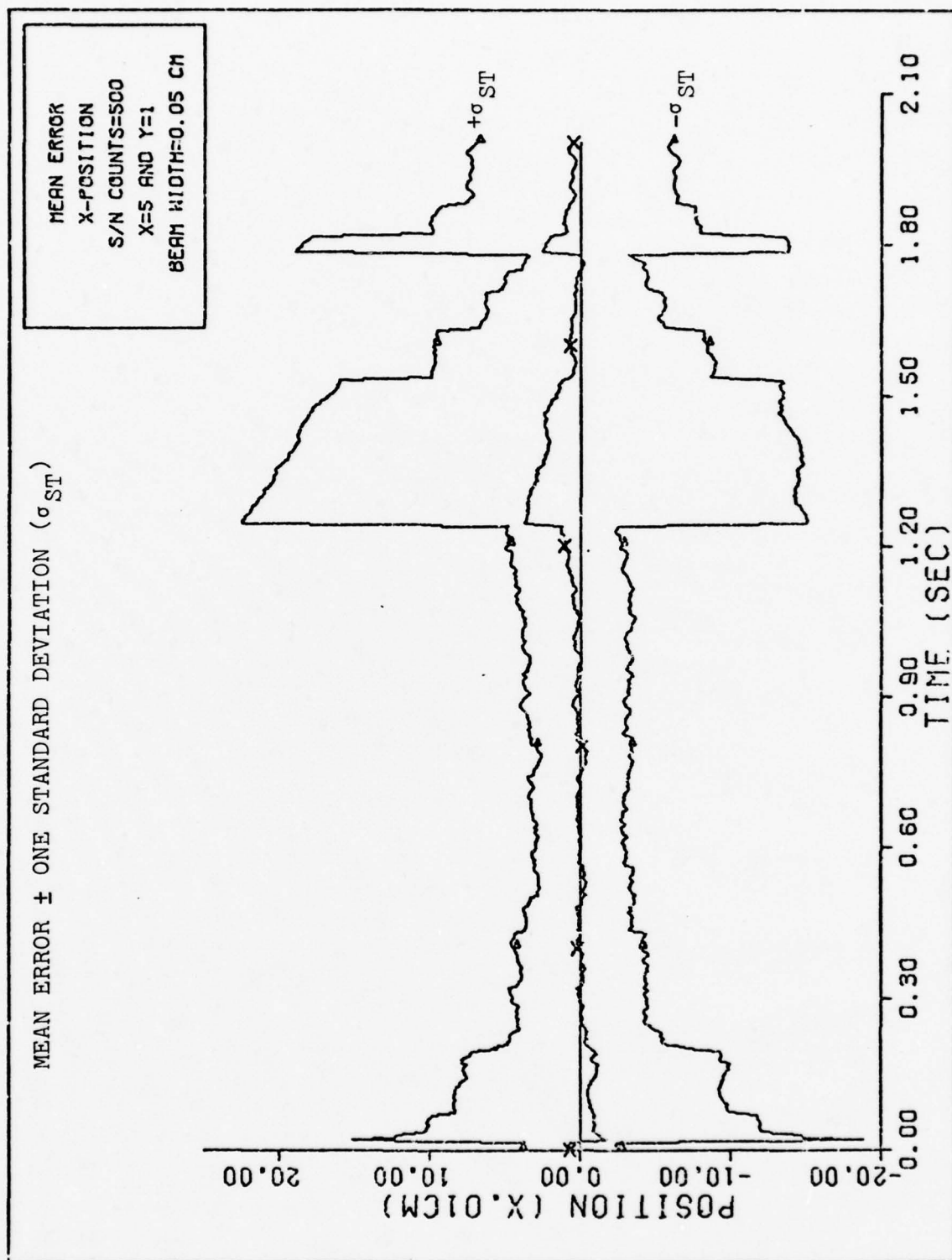


Figure 24c X-POSITION



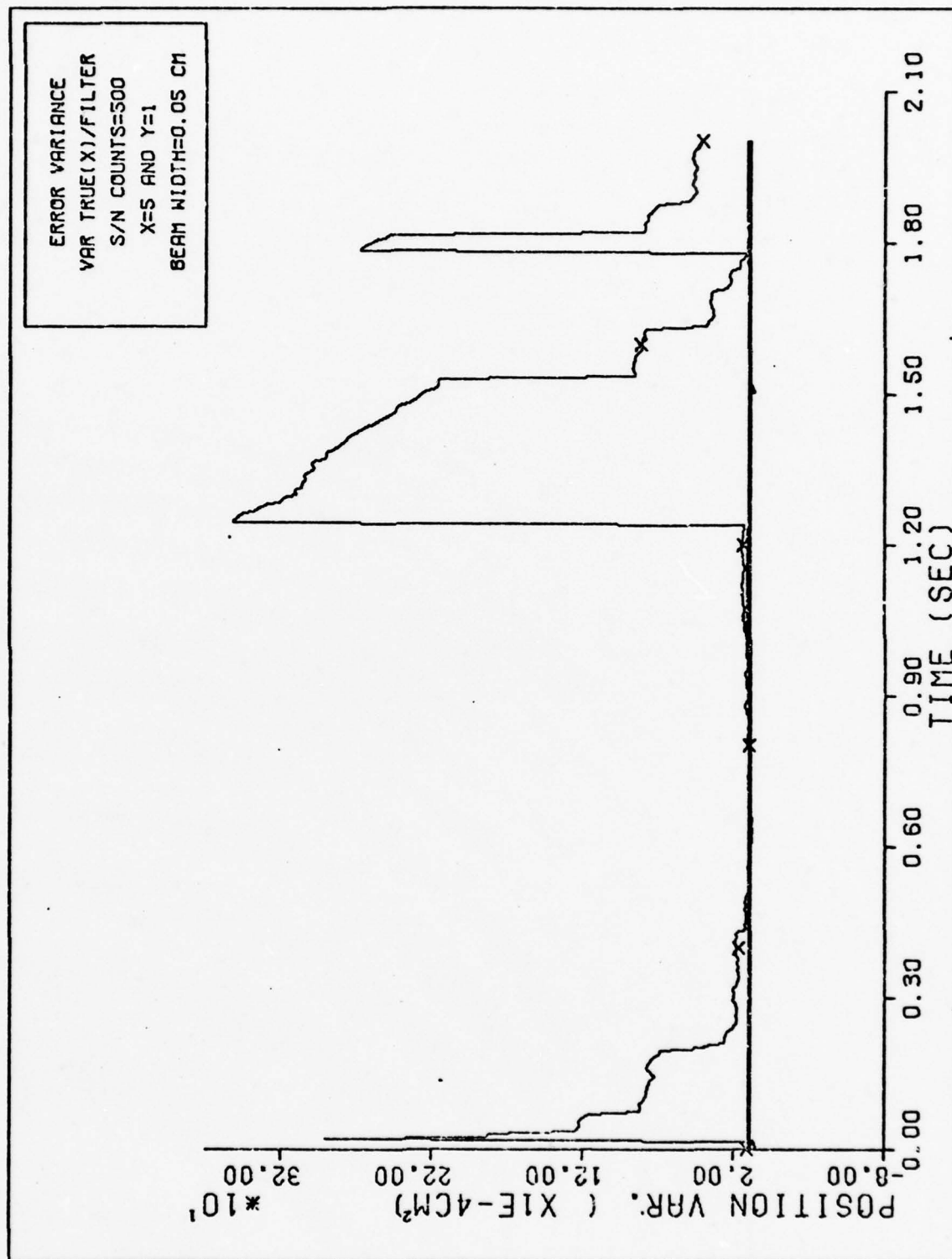


Figure 24d X-POSITION VARIANCES

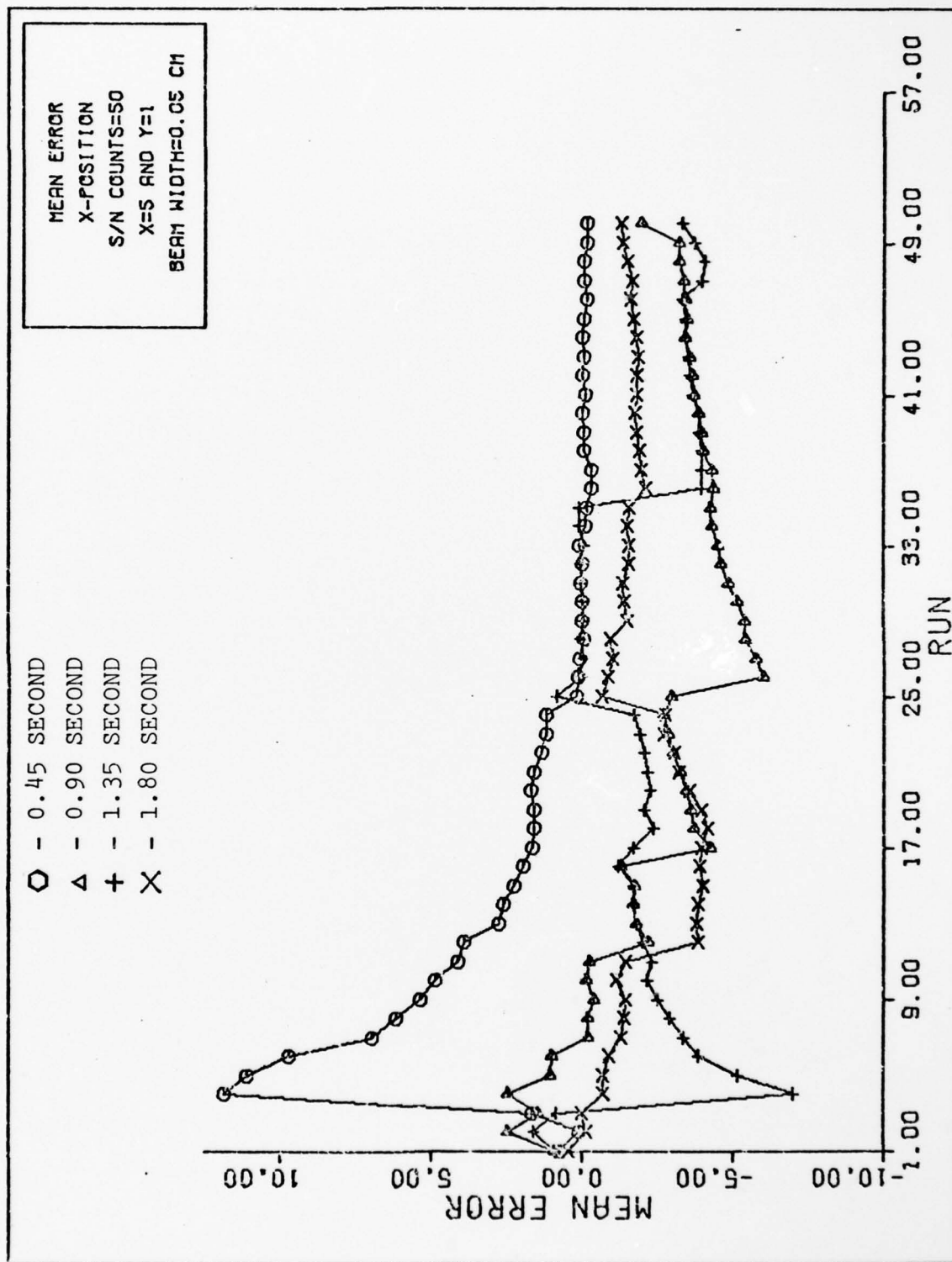


Figure 25a MEAN CONVERGENCE

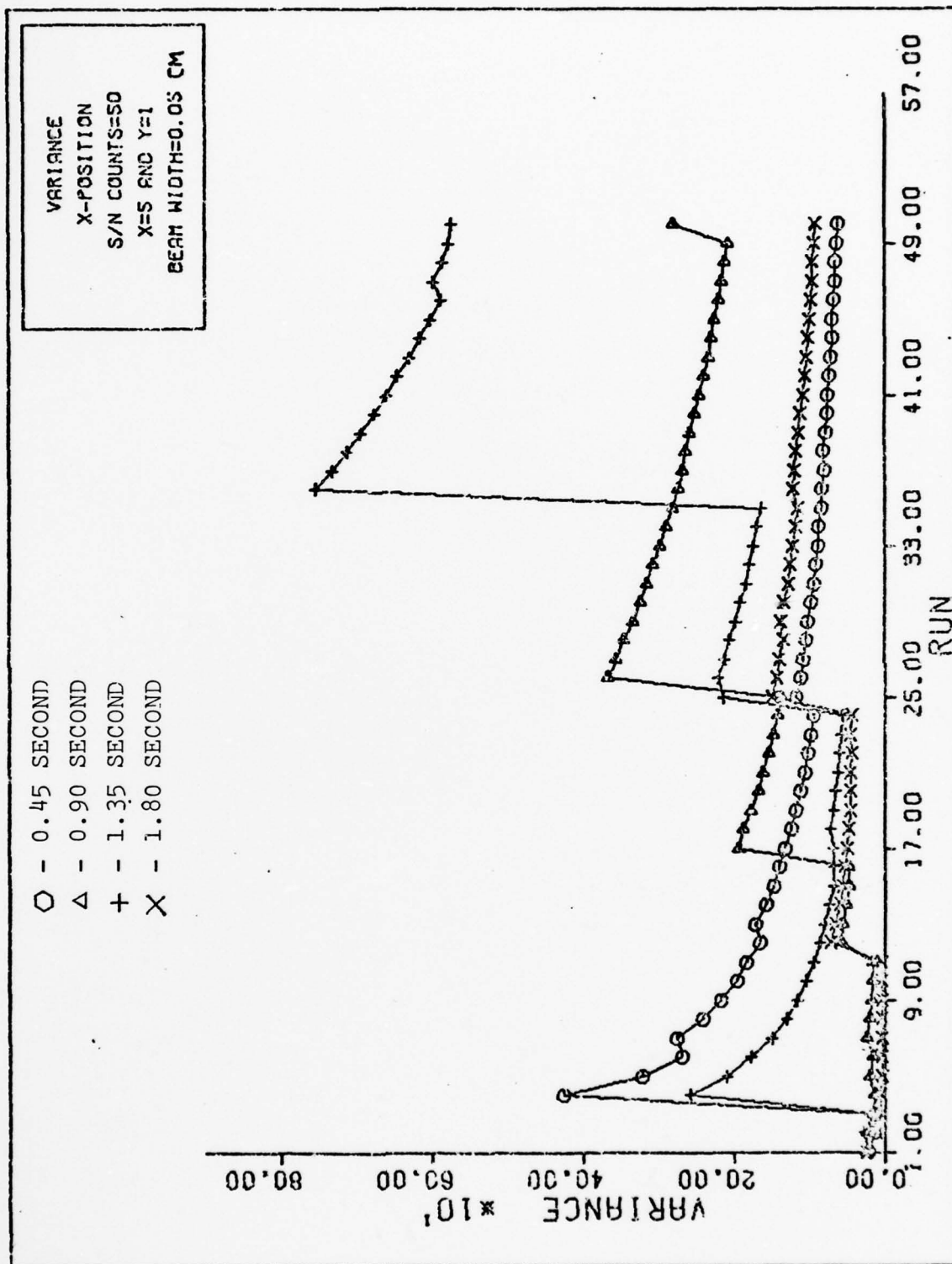


Figure 25b VARIANCE CONVERGENCE

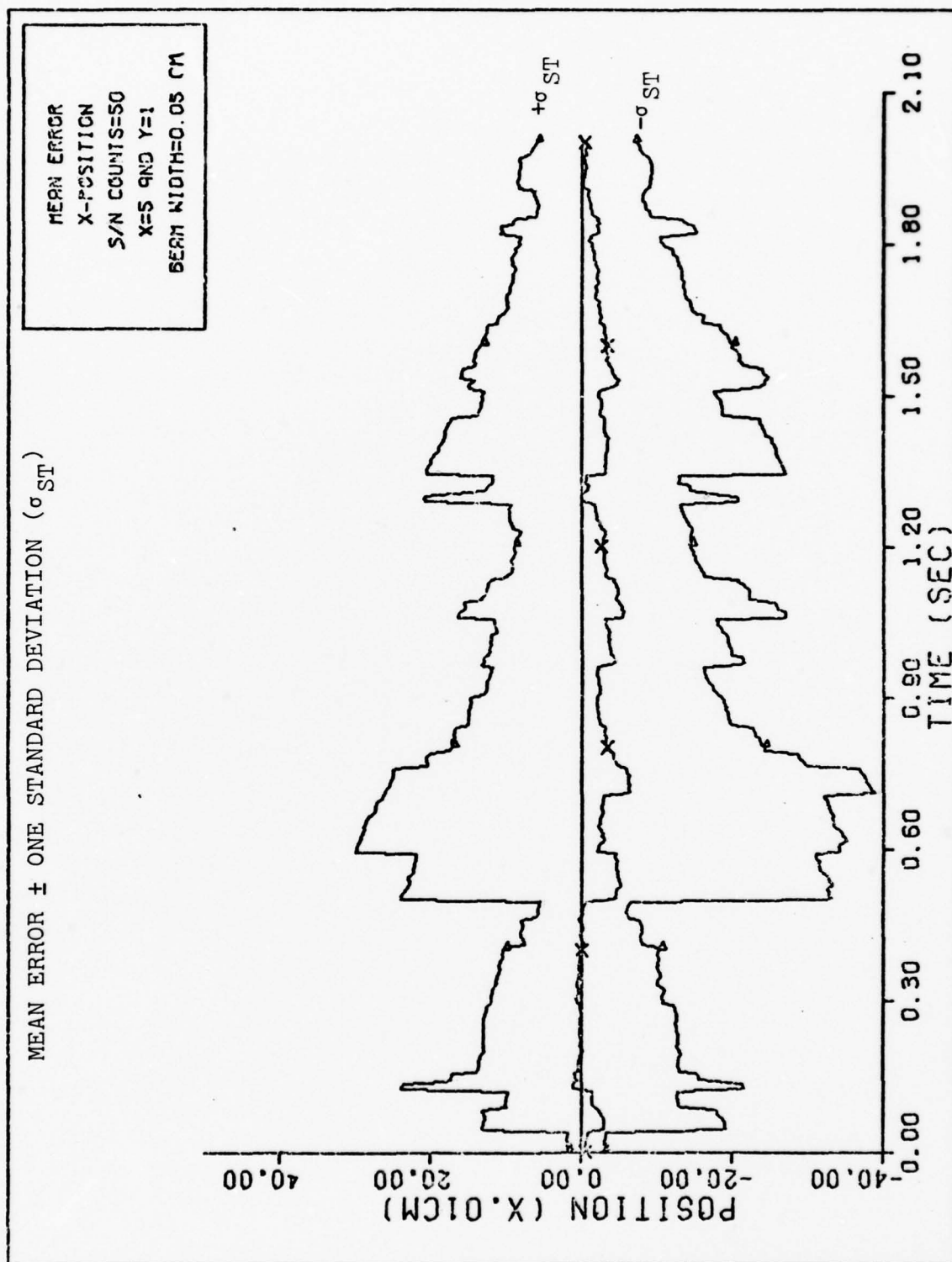


Figure 25c X-POSITION

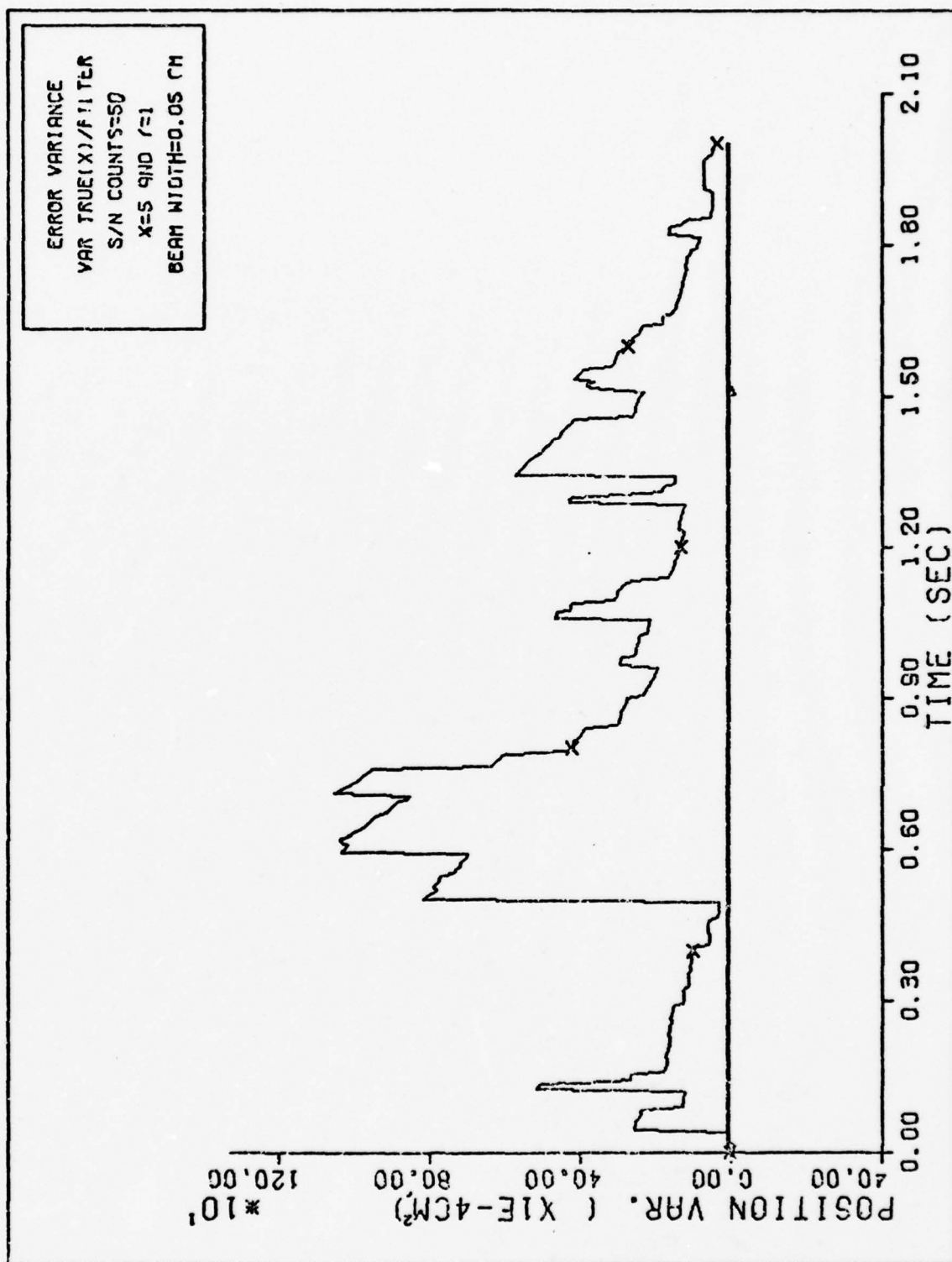


Figure 25d X-POSITION VARIANCES





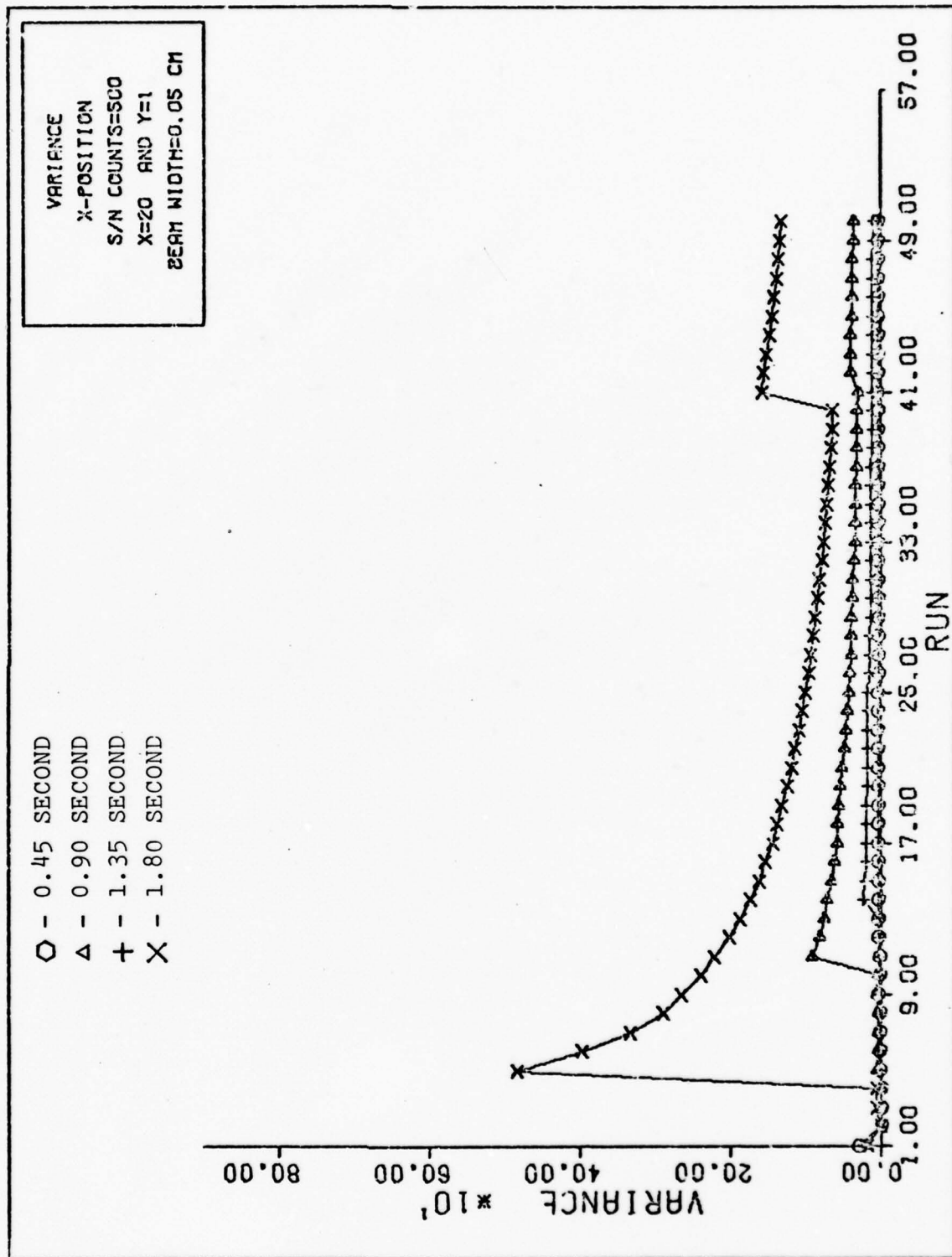


Figure 26b VARIANCE CONVERGENCE

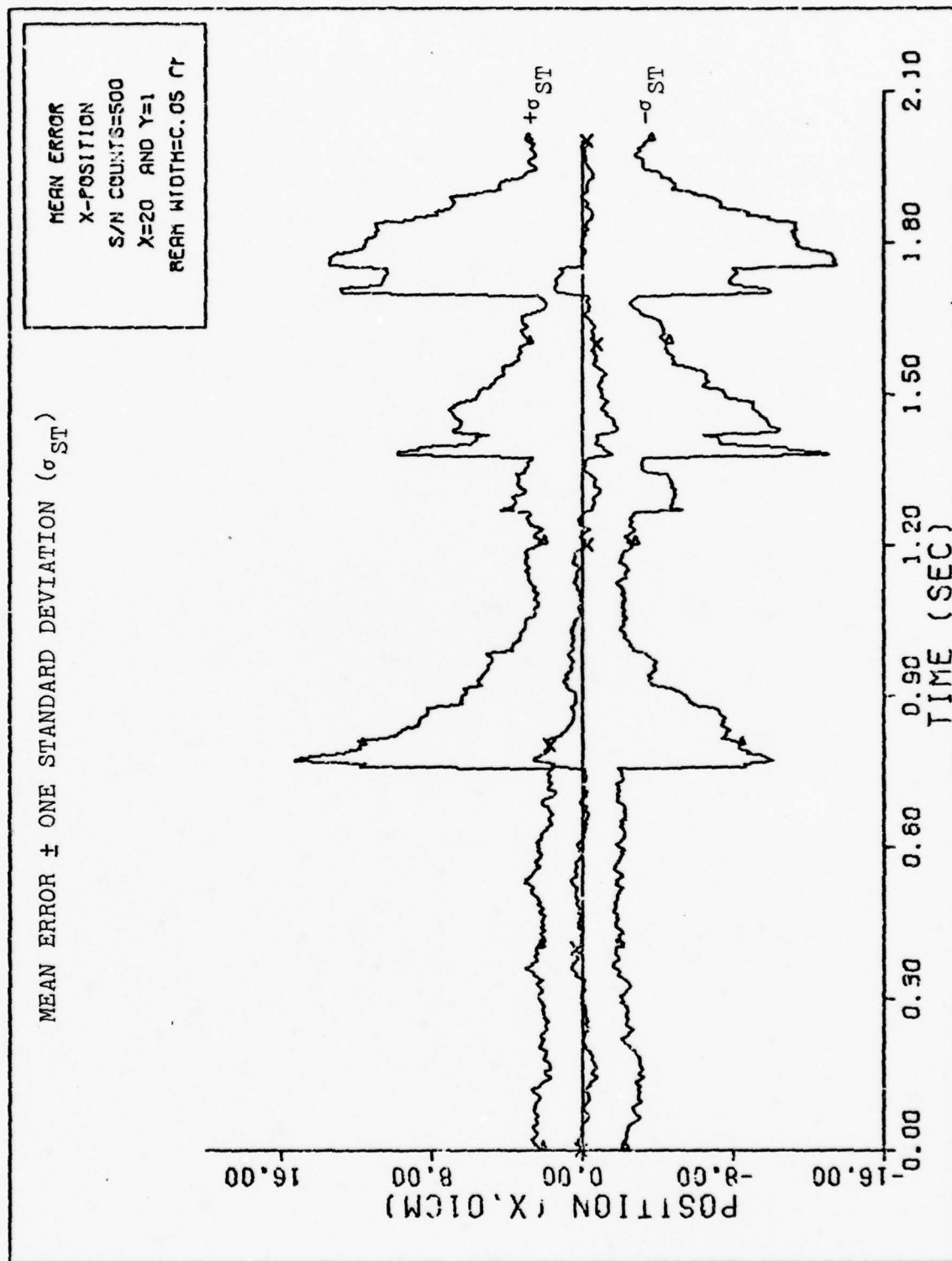


Figure 26c X-POSITION

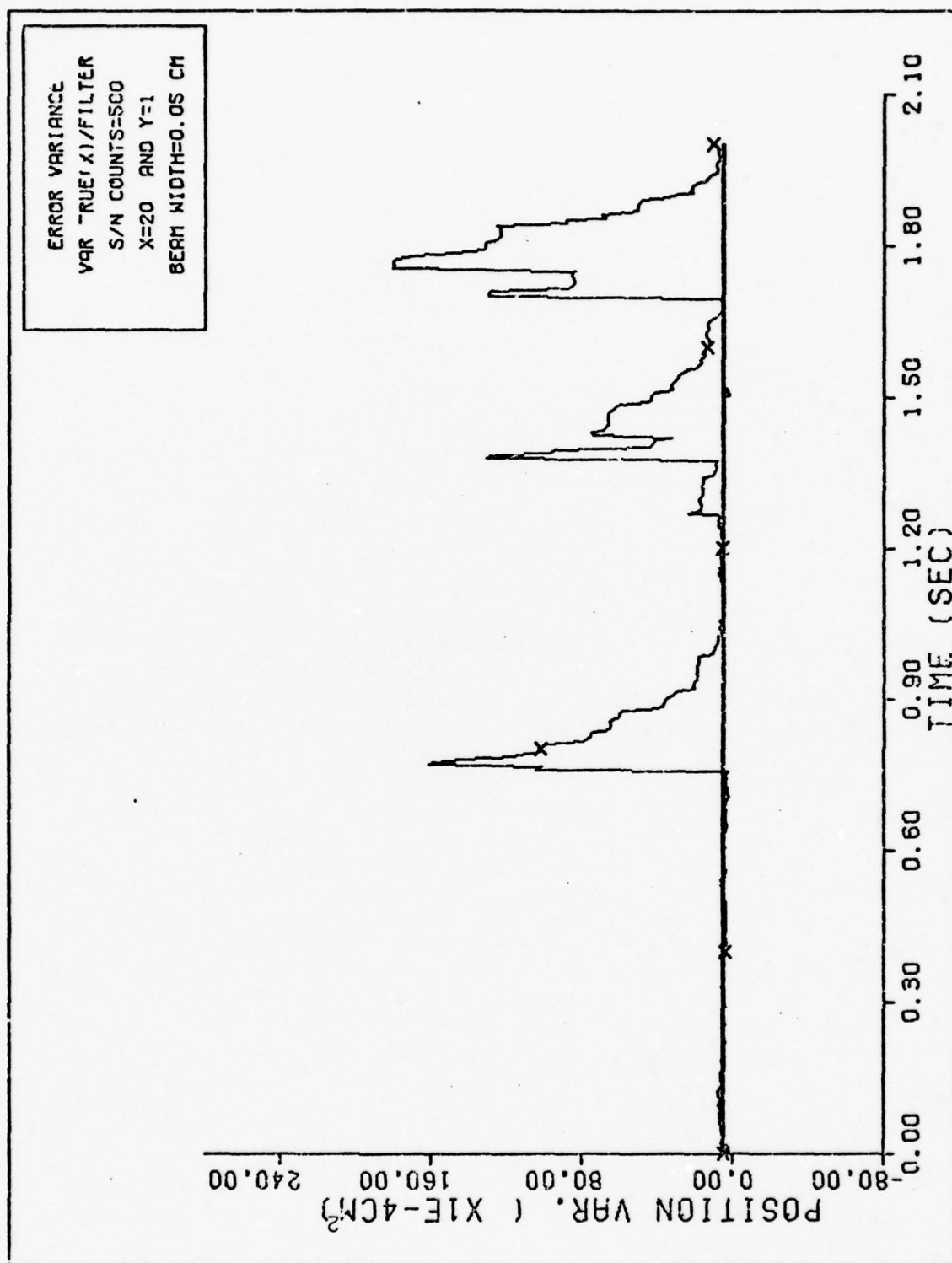


Figure 26d X-POSITION VARIANCES

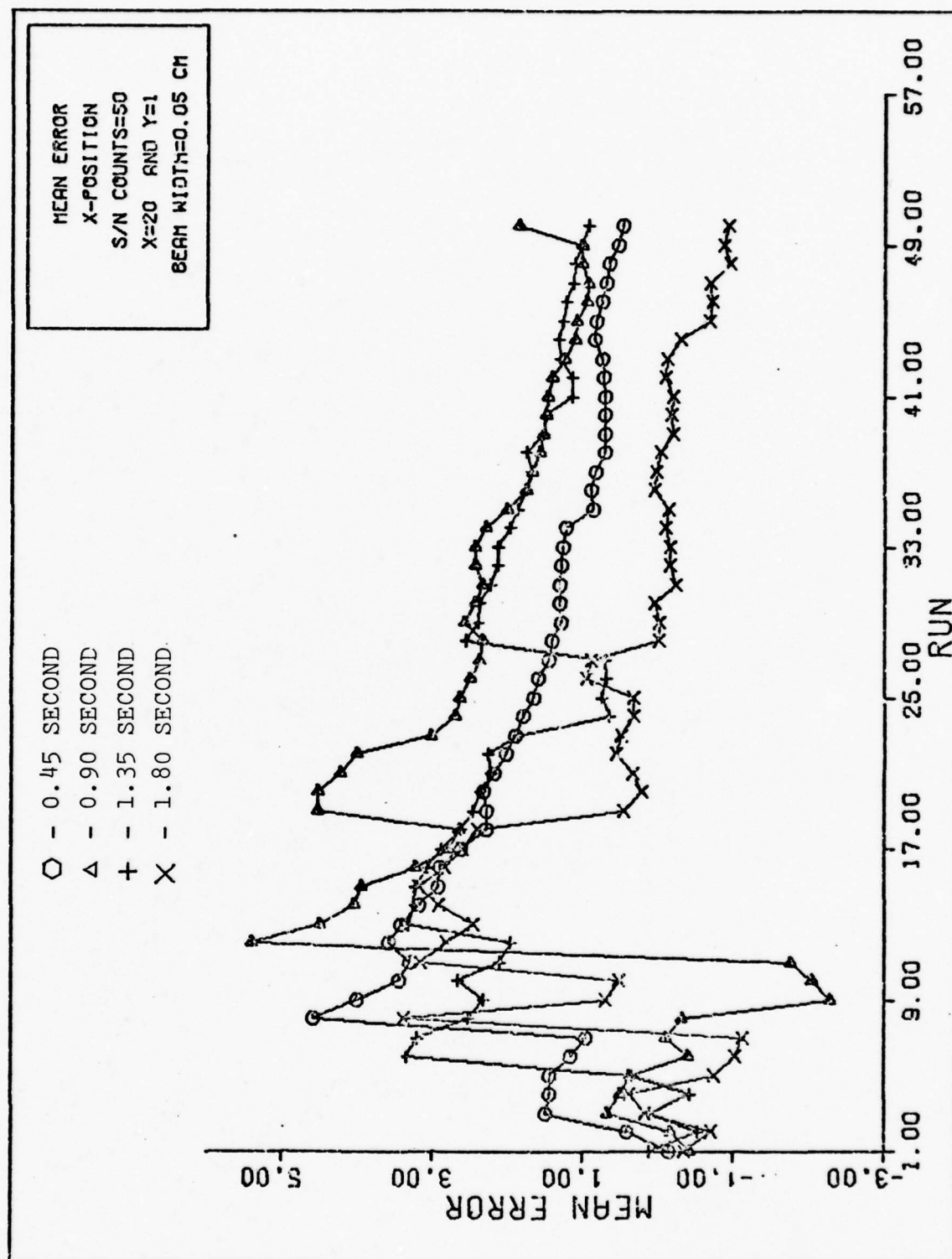


Figure 27a MEAN CONVERGENCE



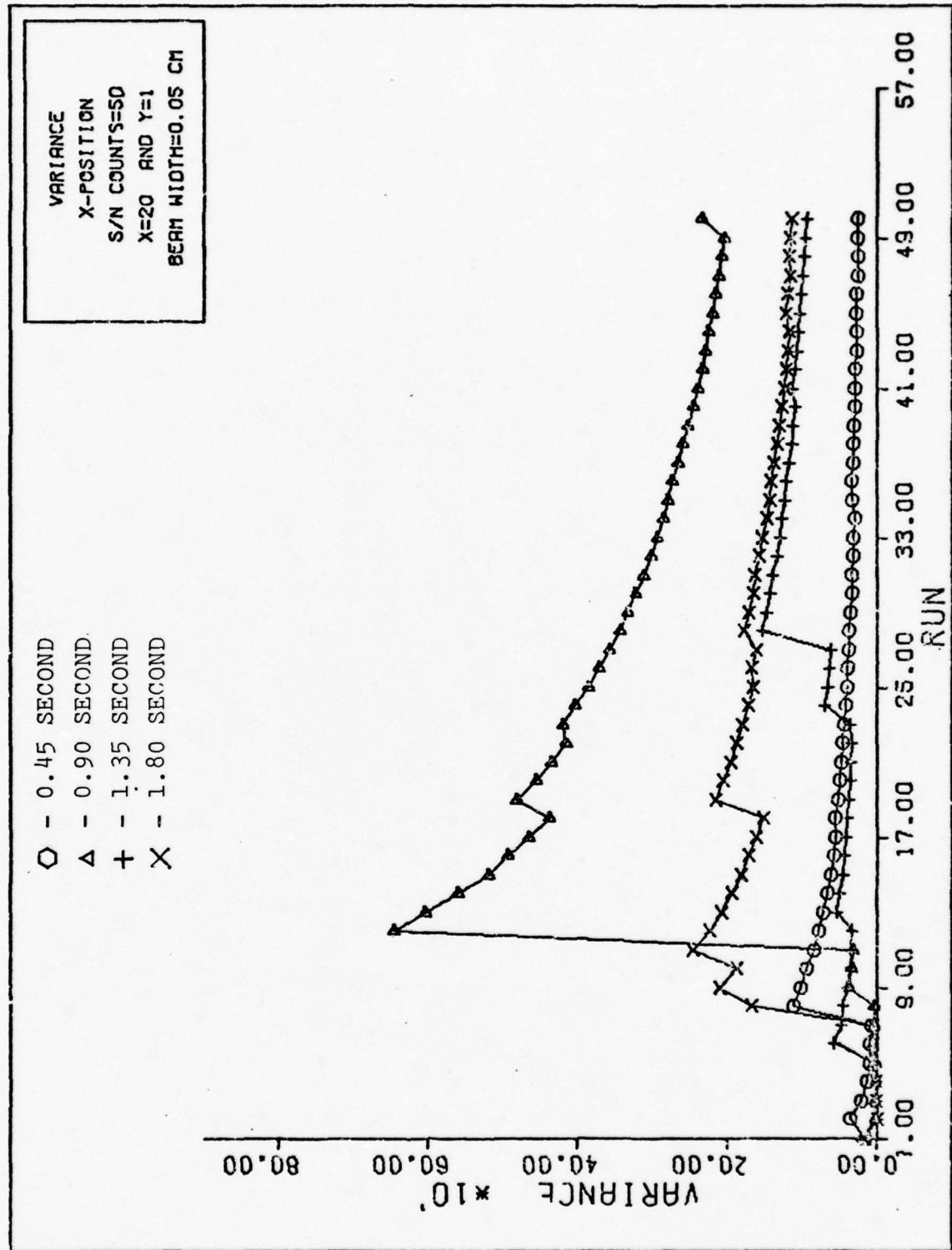


Figure 27b VARIANCE CONVERGENCE

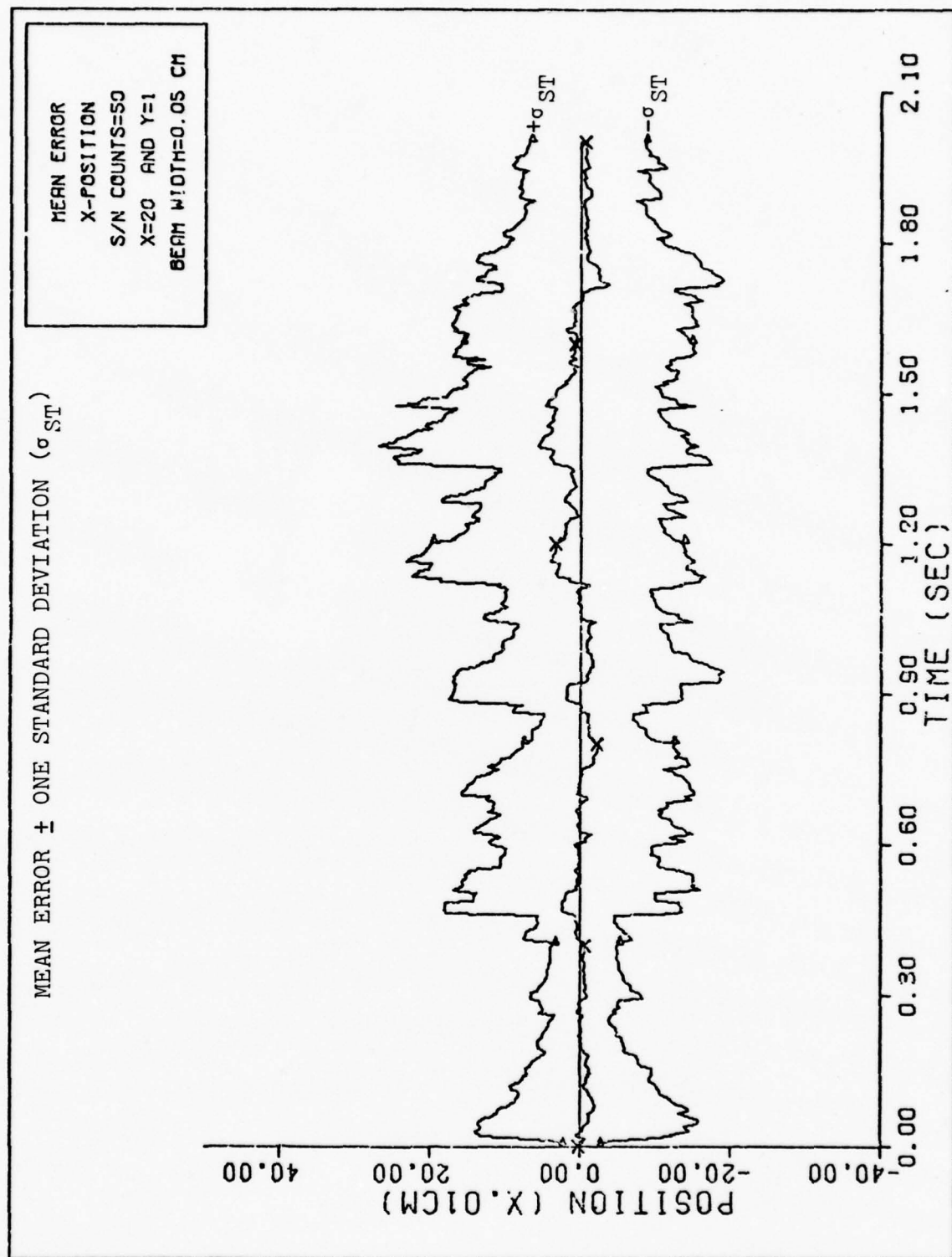


Figure 27c X-POSITION

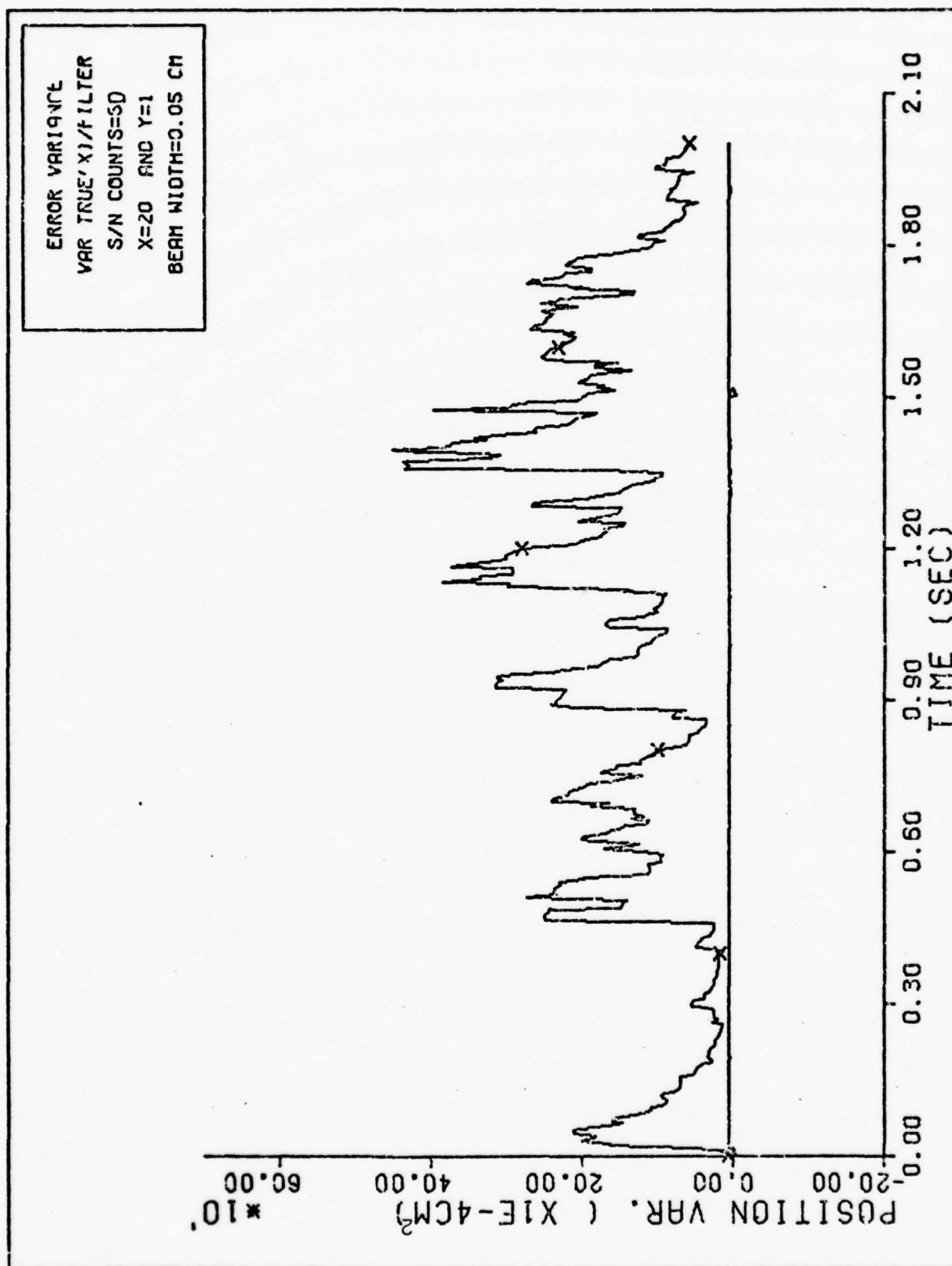


Figure 27d X-POSITION VARIANCES

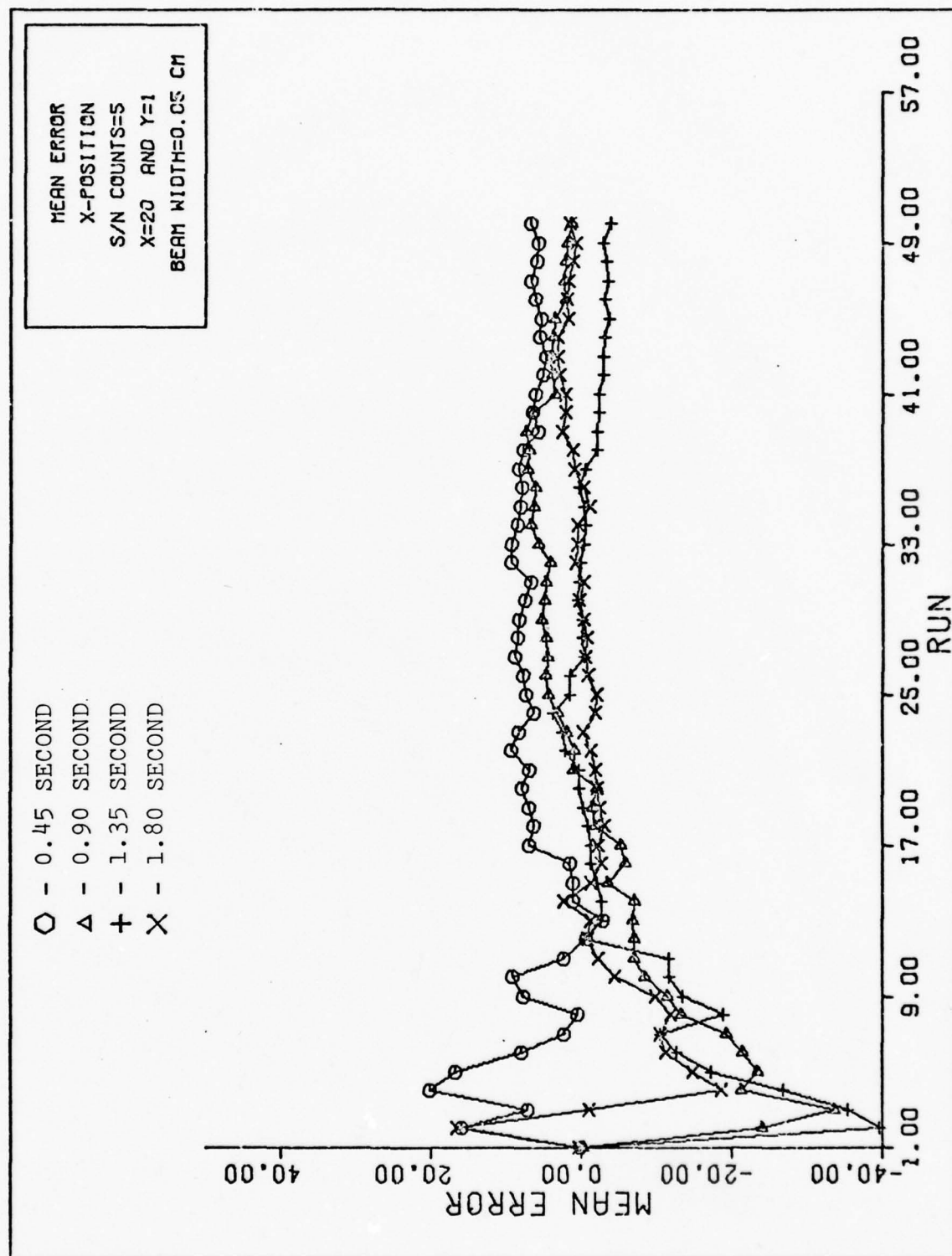


Figure 28a MEAN CONVERGENCE

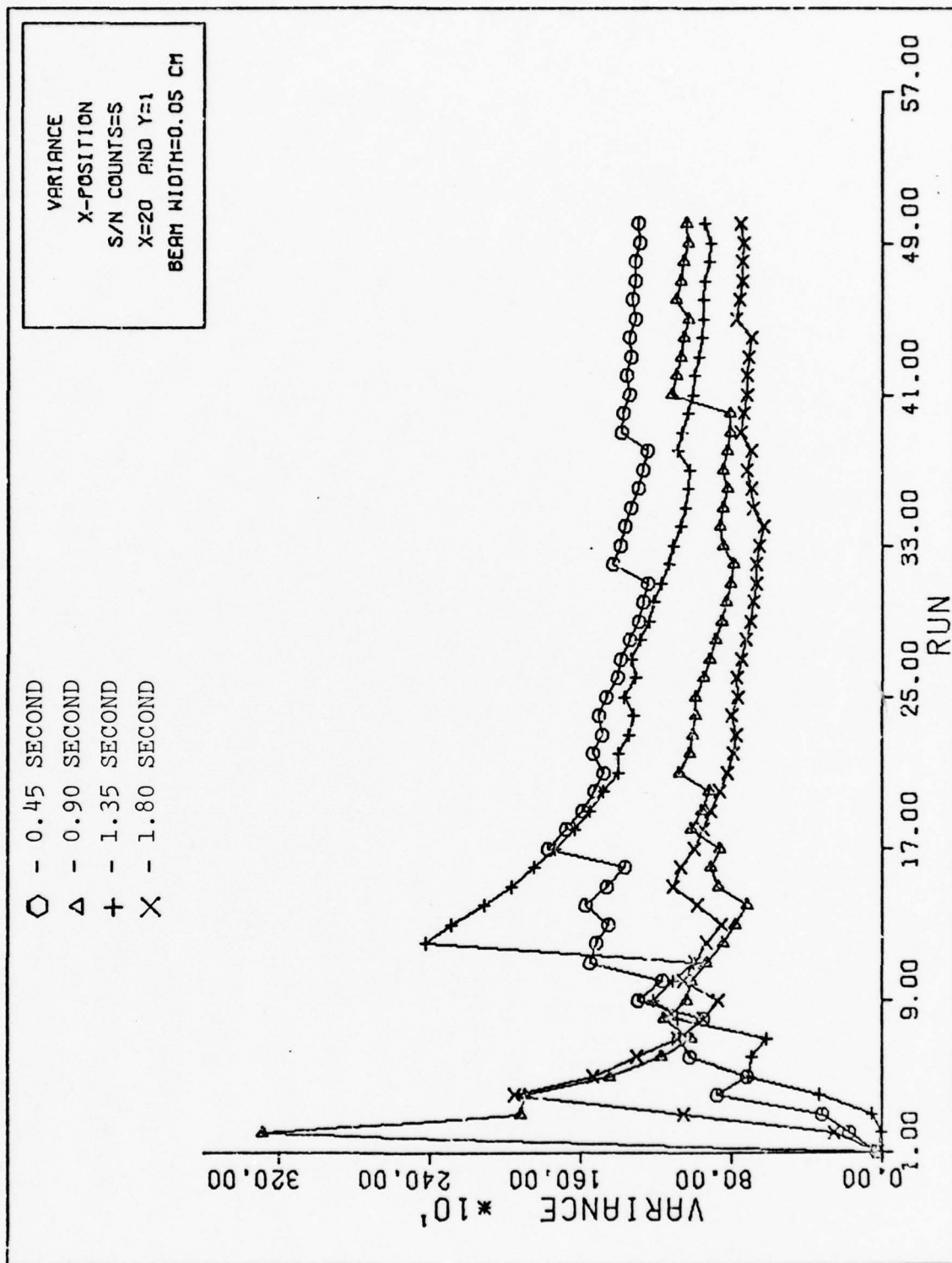


Figure 28b VARIANCE CONVERGENCE



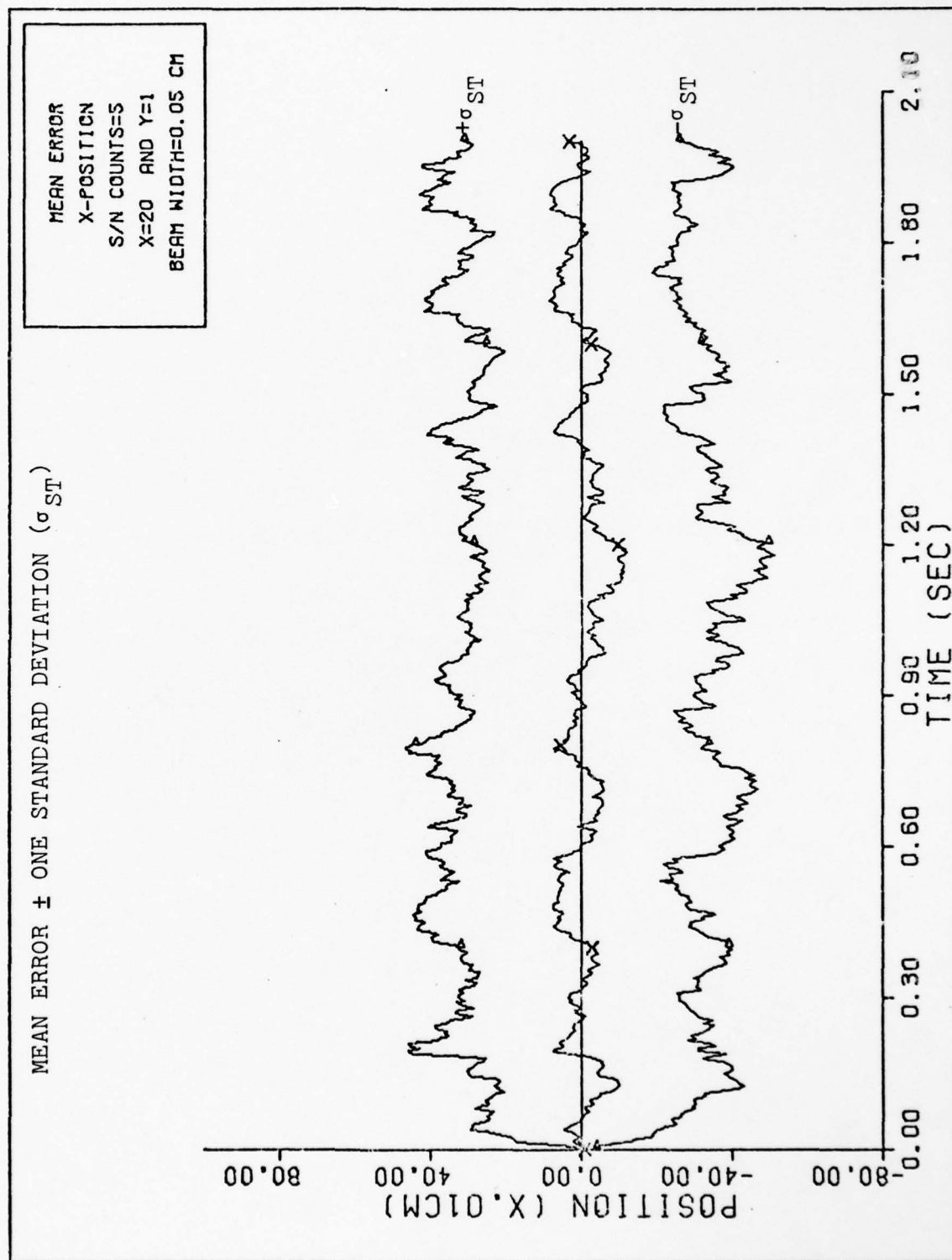


Figure 28c X-POSITION

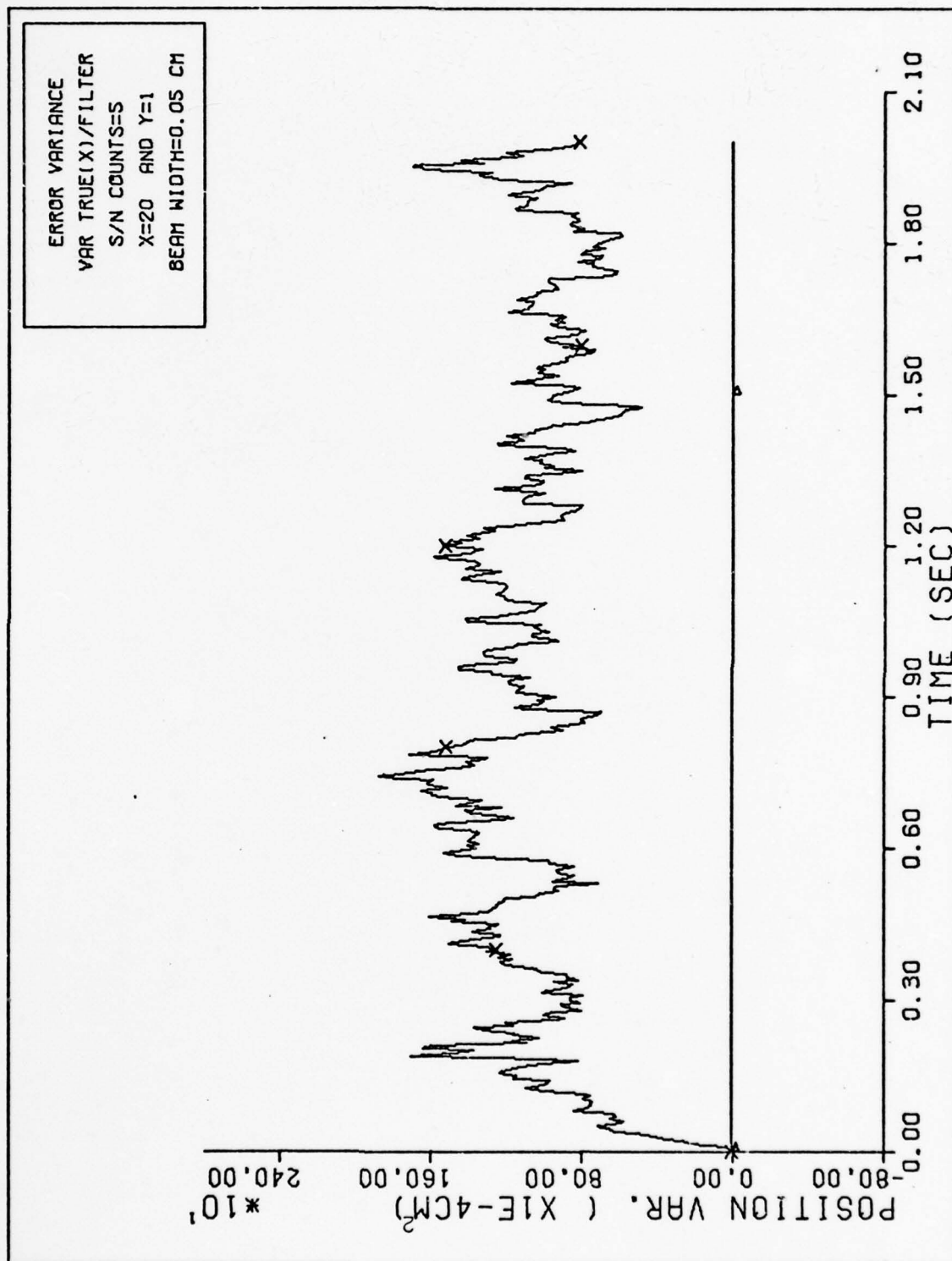


Figure 28d X-POSITION VARIANCES

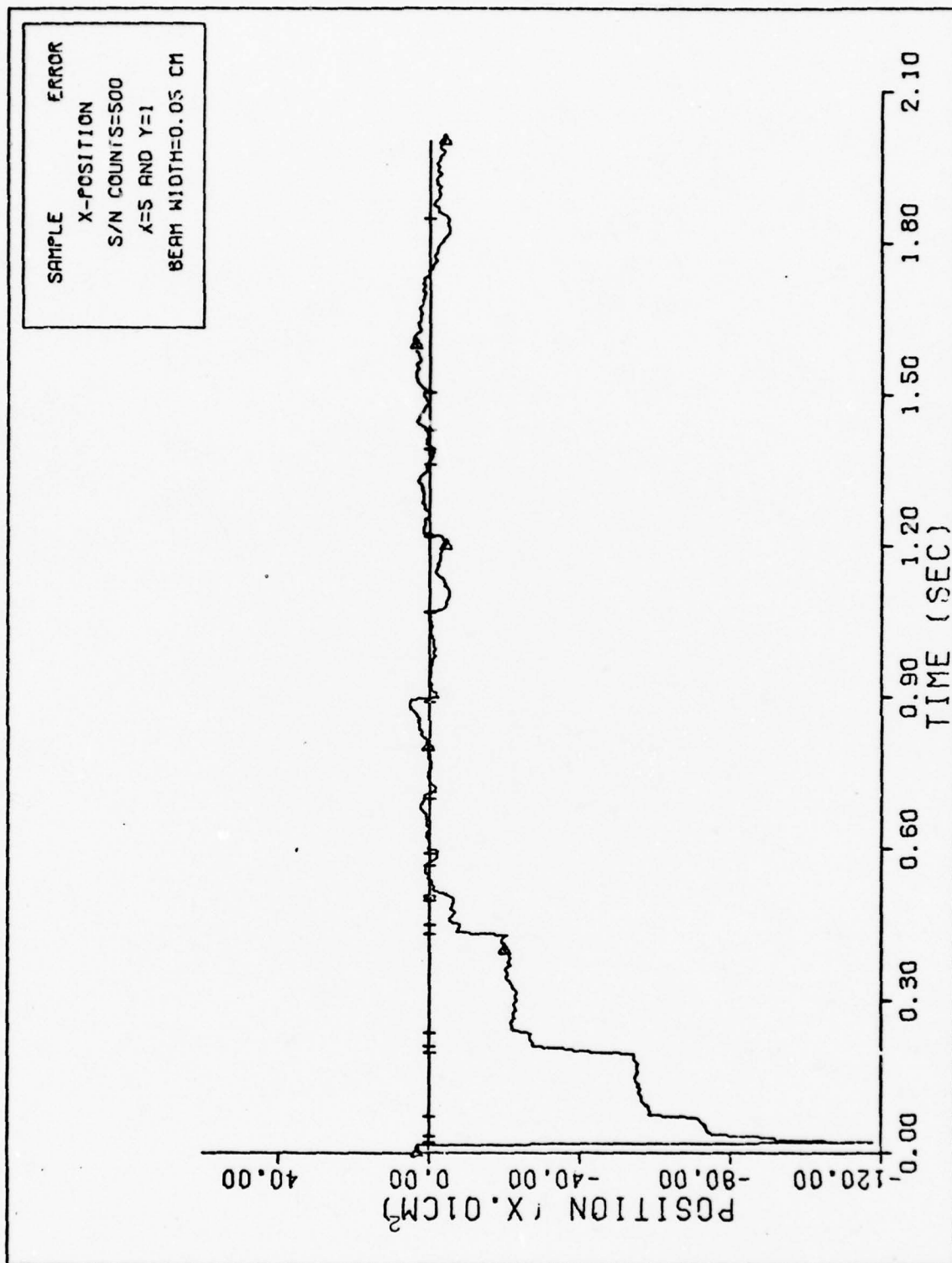


Figure 29a X-POSITION

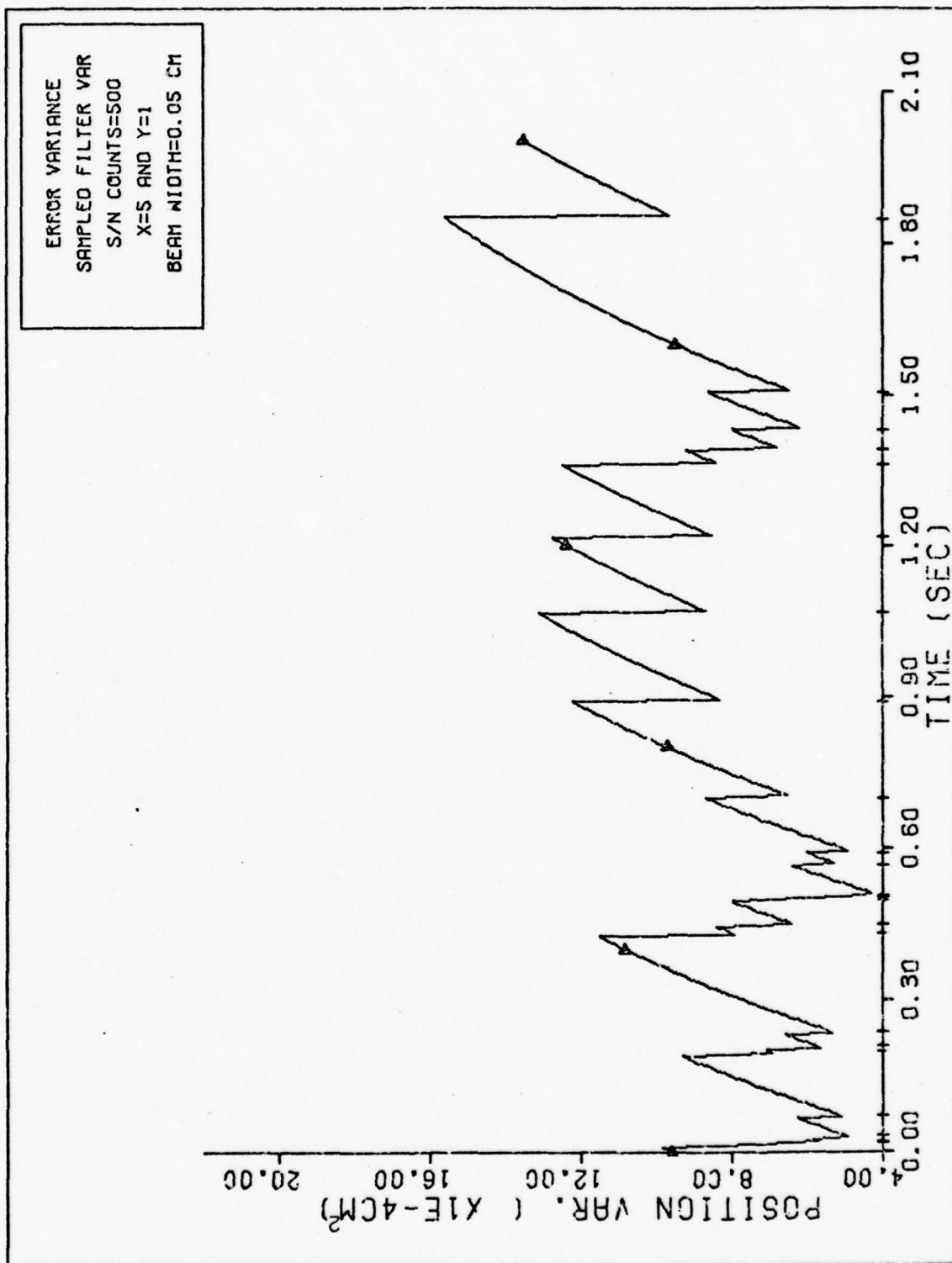


Figure 29b X-POSITION FILTER VARIANCE

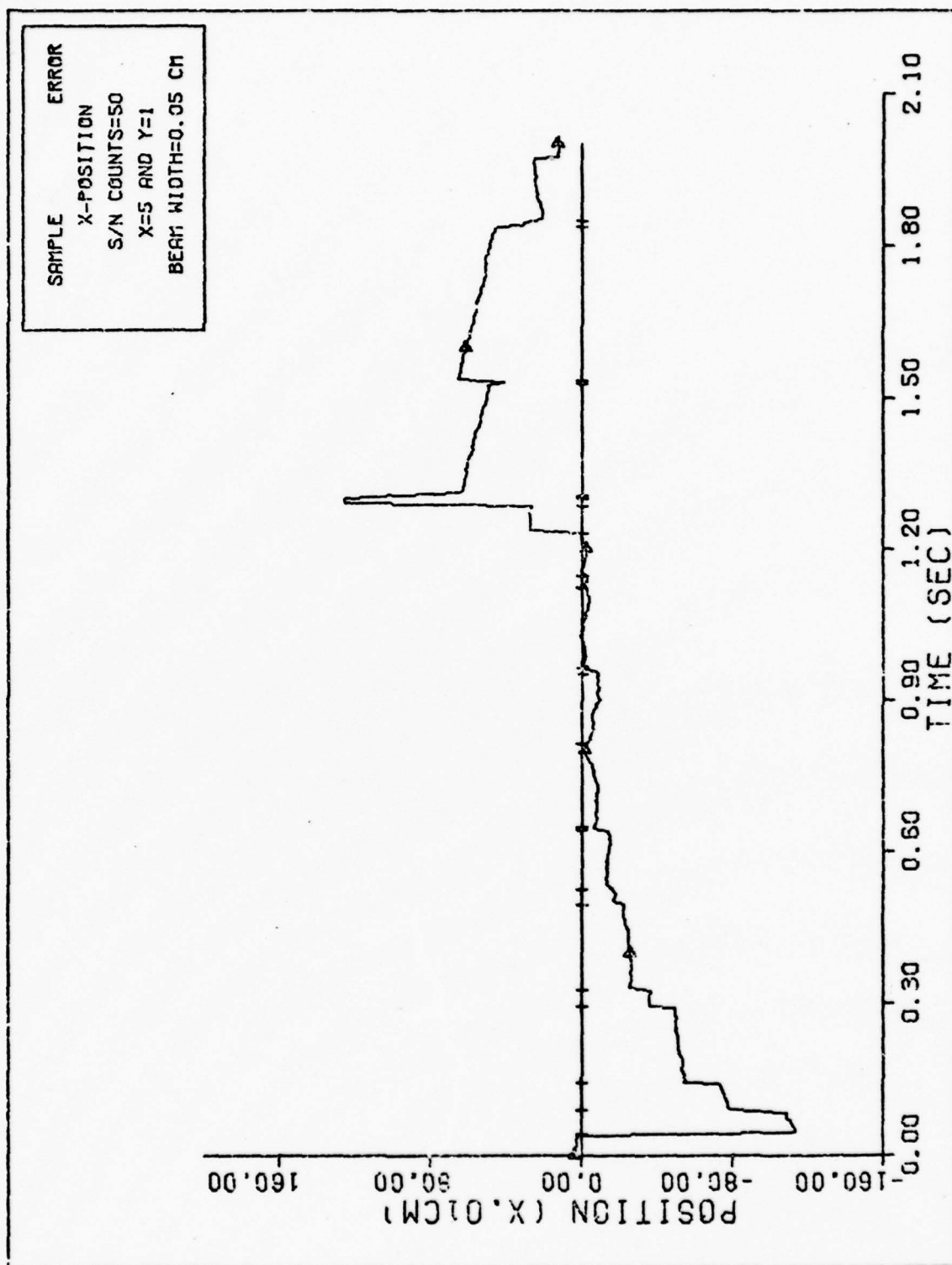


Figure 30a X-POSITION



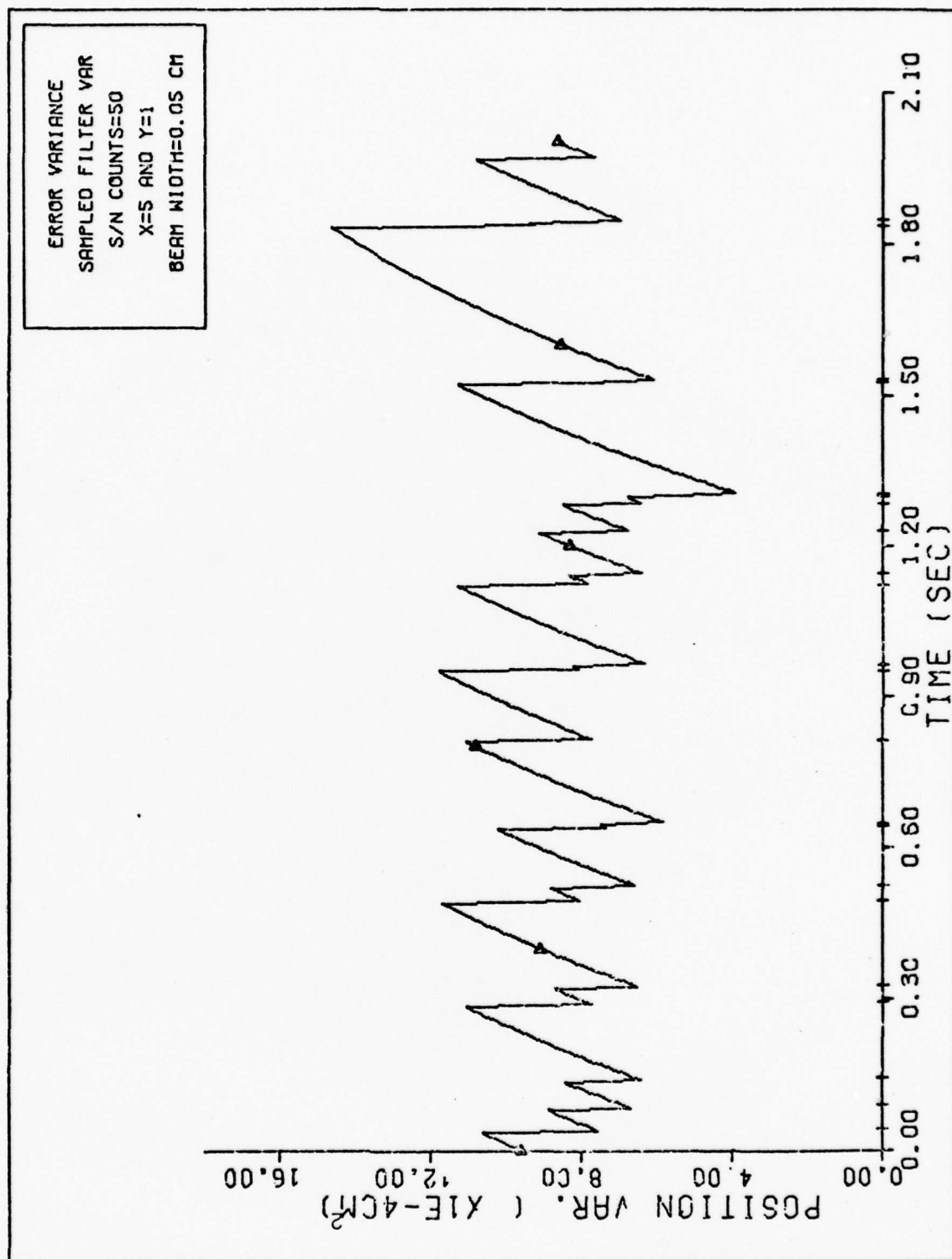


Figure 30b X-POSITION FILTER VARIANCE

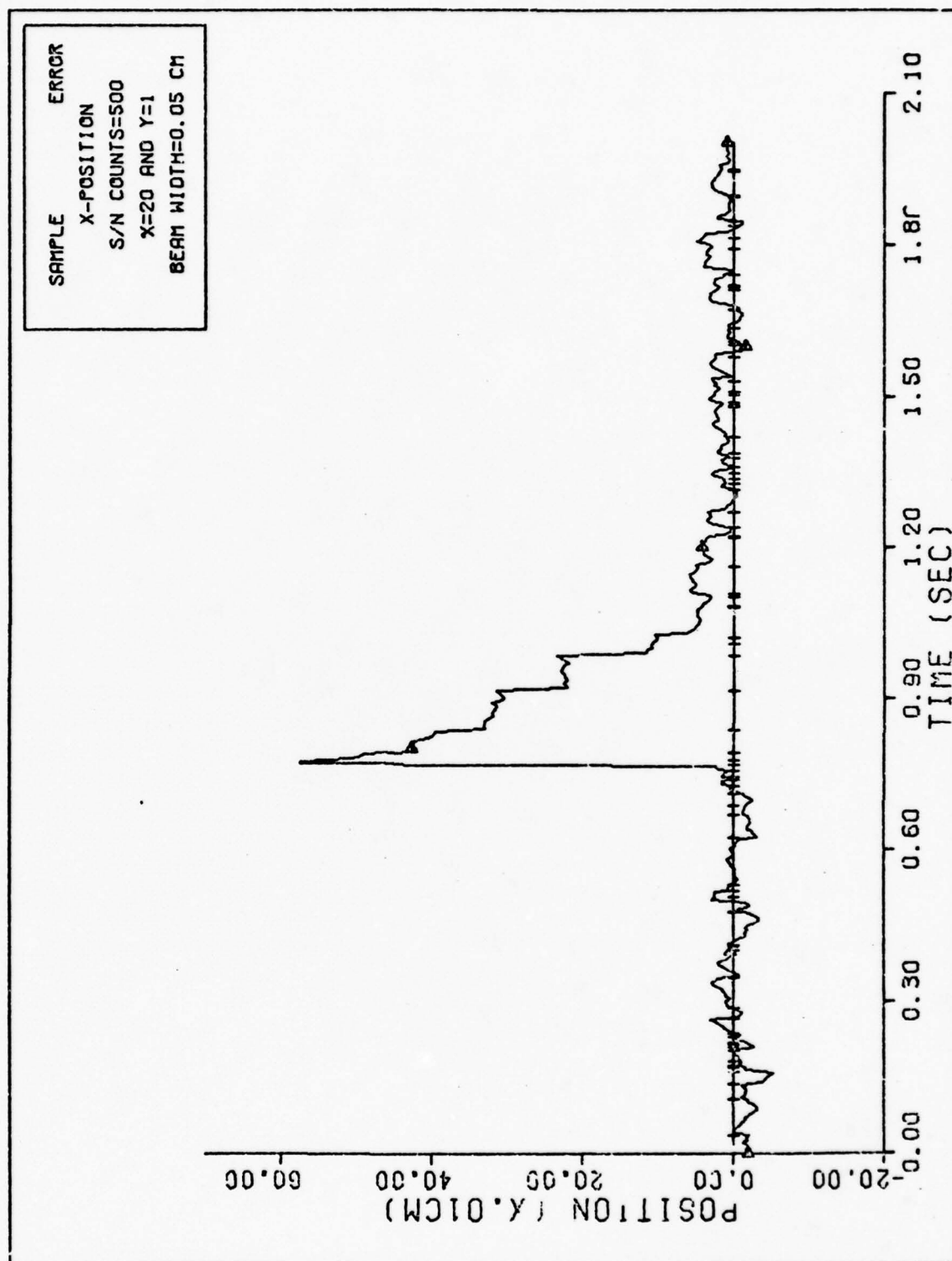


Figure 31a X-POSITION

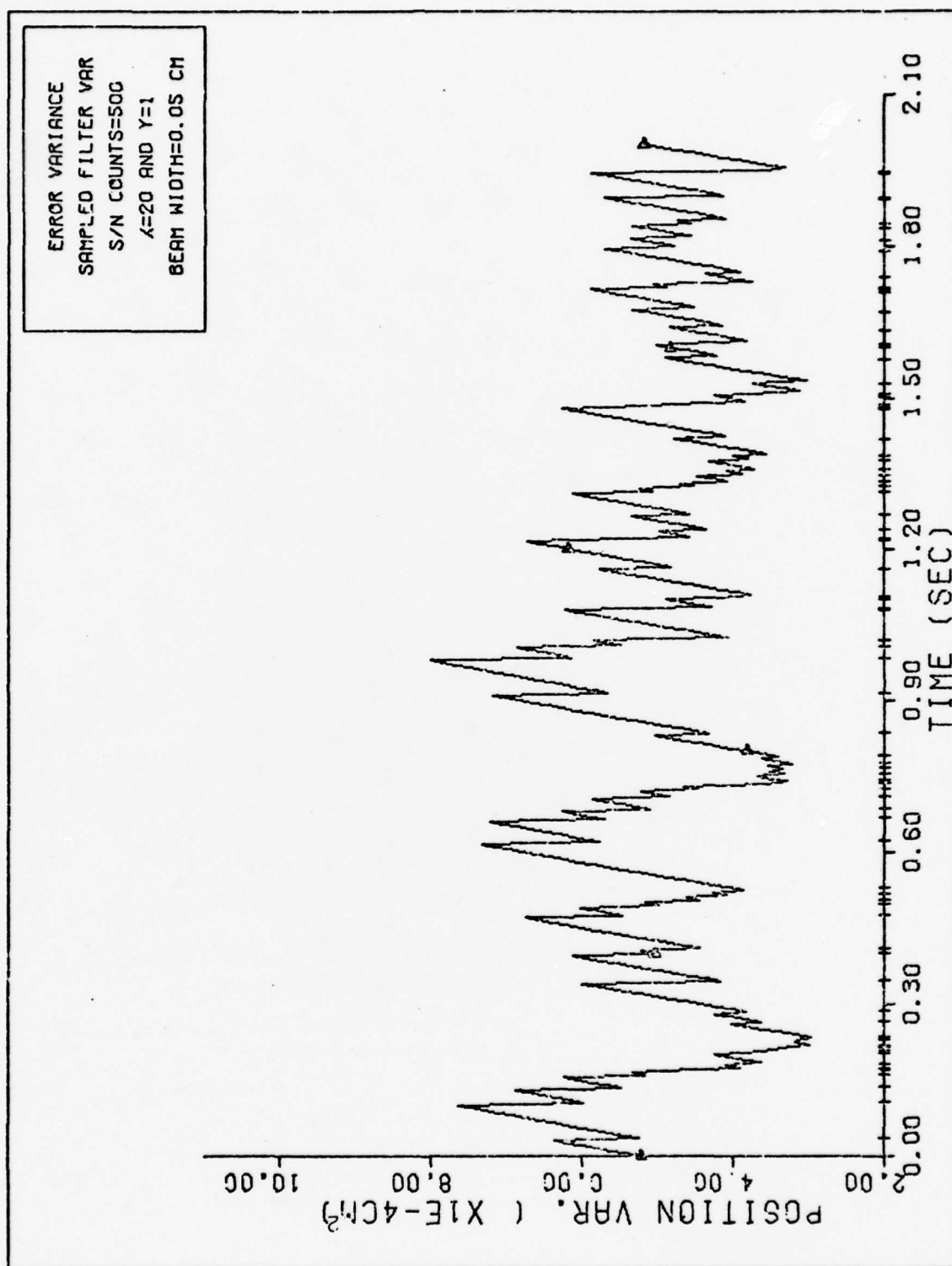


Figure 31b X-POSITION FILTER VARIANCE

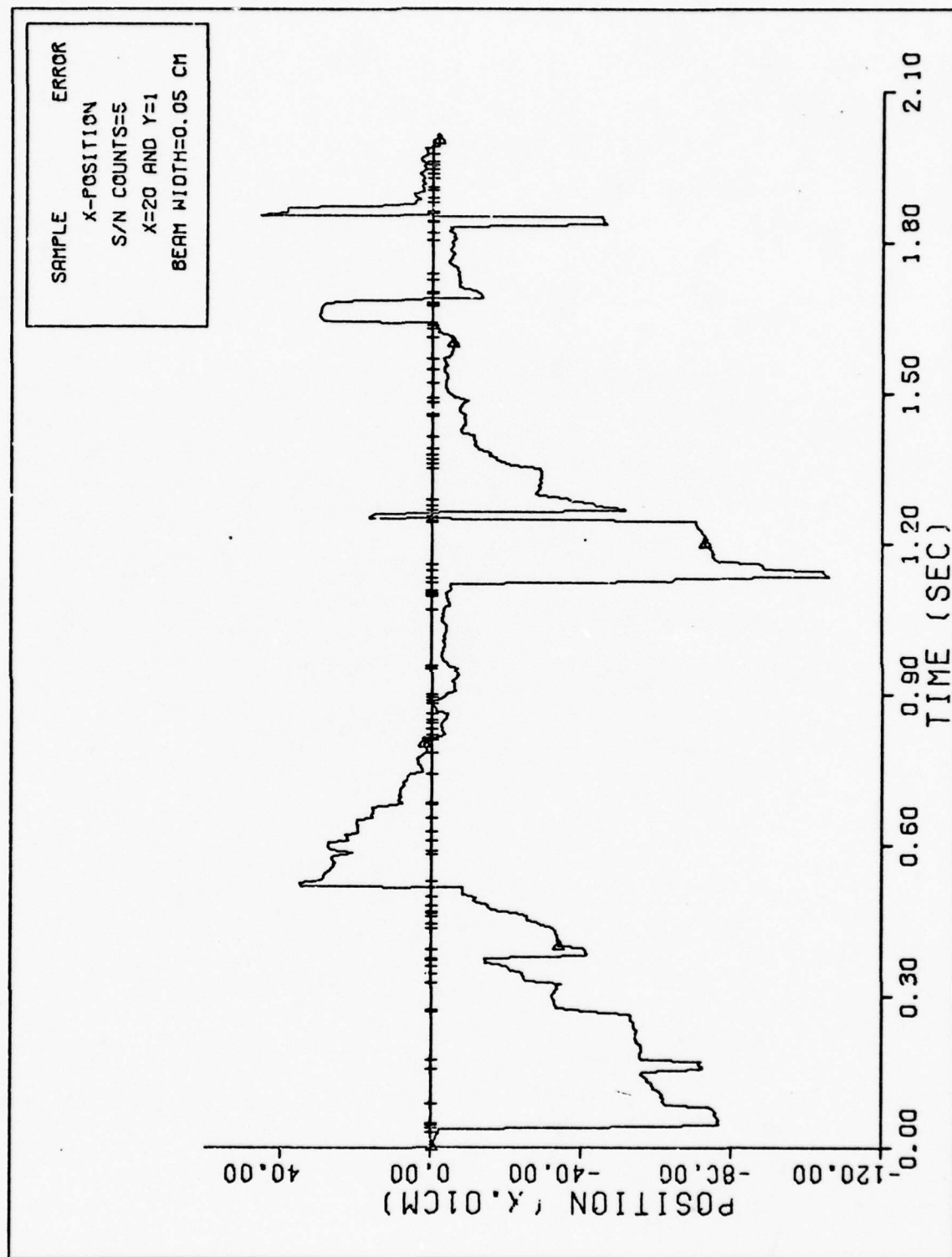


Figure 32a X-POSITION

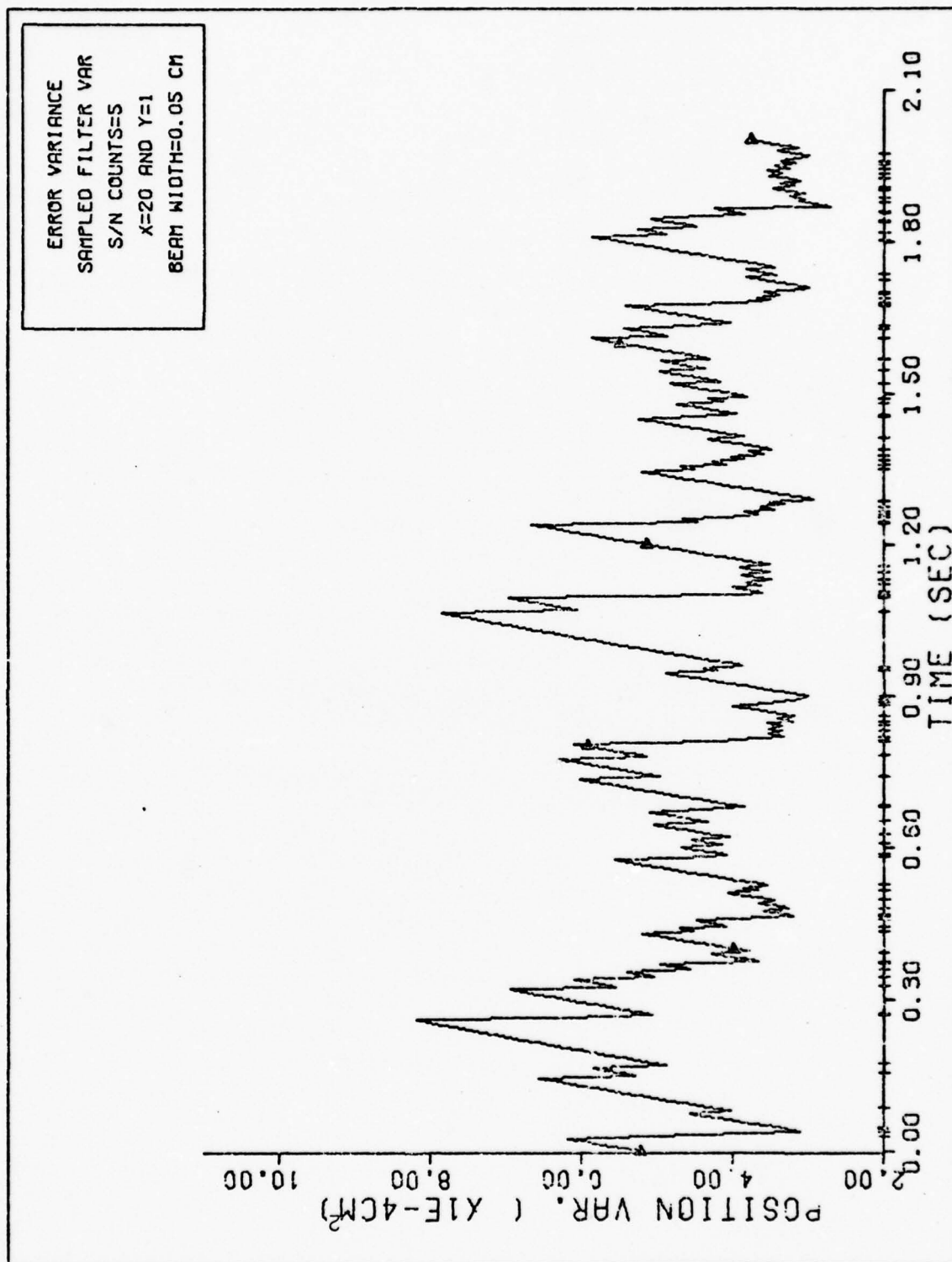


Figure 32b X-POSITION FILTER VARIANCE



the beam width is decreased, which means that the signal events are distributed at locations very near the position of maximum intensity, then the filter should weigh the measurement heavily since there is less "corruption" in the measurements. Recall that the filter assumes the photodetector array is very large; and for dark limited conditions, the dark events can occur anywhere in the array with equal probability. Thus, the beam width must be very wide in order to put less weight in the dark measurements. Since the filter cannot distinguish between a dark or signal event, the signal measurements will also have less weight. In other words, the beam is assumed to be wide in order to "wash" out the dark events; and the signal events are also assumed to be distributed at larger distances from the spot's centroid of maximum intensity. From this discussion, it becomes evident that altering the beam width in order to compensate for the dark events has some problems, especially if the photodetector array is dark current-limited. It would be preferable to try to distinguish signal events from dark events and weigh them properly.

In residual monitoring, the sequence of residuals are monitored in real-time to decide whether the current measurement value can be discarded as a "bad" data point. Consider Eq. (23) which is repeated below as

$$\hat{x}(t_{k+}) = \hat{x}(t_{k-}) + K(t_{k-})[\underbrace{r_k - \hat{x}(t_{k-})}_{\text{residual}}] \quad (65)$$

where  $H(t_k)=1$ . From Eq. (65), a residual is simply the difference between the measurement,  $r_k$ , and the conditional

mean  $\hat{x}(t_k^-)$  of the measurement, conditioned on only the previous history of measurements. Residual monitoring would be used to test for events that are not due to the spot. If the events fail the test, then the filter does not process the dark measurement. Instead, the filter propagates its conditional mean and covariance until it senses another event which passes the test. For this study, if the residual in Eq. (23) is greater than three times the beam width, then the event is discarded. Note that in residual monitoring, there is no need to increase the beam width. In other words, the event locations (due to the spot) have the same distribution about the spot's centroid, as before. Thus, residual monitoring can be exploited effectively for high signal-to-noise counts ratio, since few events will fail the test. Physically, residual monitoring is a better method of compensation than filter tuning in order to handle the dark current effects.

As a rough comparison in performance improvement between the above methods, the square of the mean errors at the sample times are all summed. The results from this method are listed in Tables 3 and 4. The tables indicate that residual monitoring is a better method to handle the dark current effects than altering the beam width. For particular cases, plots of the variances in which these methods are employed are shown in Figs. (33) through (36). These plots show that the Snyder Filter performance can be enhanced substantially through residual monitoring by not processing the dark measurement. As expected, these results correspond to the physical arguments mentioned in previous paragraphs.

Average Signal-to-Noise Counts Ratio	Method of Compensation	Beam Width (x0.01 cm)	Sum of the Square of the Mean Error
$\infty$	None	5.0	207.0
500	None	5.0	555.0
500	Residual Monitoring	5.0	80.2
500	Filter Tuning	7.5	323.0
500	Filter Tuning	10.0	223.0
500	Filter Tuning	15.0	166.0
500	Filter Tuning	20.0	167.0
500	Filter Tuning	30.0	196.0
50	None	5.0	3150.0
50	Residual Monitoring	5.0	66.3
50	Filter Tuning	10.0	1230.0
50	Filter Tuning	20.0	198.0
50	Filter Tuning	40.0	110.0
50	Filter Tuning	20.0	377.0
1	None	5.0	2860.0
1	Residual Monitoring	5.0	33.0
1	Filter Tuning	30.0	350.0
1	Filter Tuning	40.0	70.7

Table 4. Test Cases for X=5 and Y=1  
(with dark current)

Average Signal-to-Noise Counts Ratio	Method of Compensation	Beam Width (x0.01 cm)	Sum of the Square of the Mean Error
$\infty$	None	5.0	42.7
500	None	5.0	171.3
500	Residual Monitoring	5.0	33.6
500	Filter Tuning	6.0	142.4
500	Filter Tuning	7.0	122.3
500	Filter Tuning	8.0	95.1
500	Filter Tuning	10.0	83.7
500	Filter Tuning	20.0	57.8
500	Filter Tuning	30.0	50.9
50	None	5.0	1160.0
50	Residual Monitoring	5.0	41.0
50	Filter Tuning	10.0	423.0
50	Filter Tuning	15.0	208.0
50	Filter Tuning	30.0	97.2
50	Filter Tuning	40.0	105.0
5	None	5.0	8940.0
5	Residual Monitoring	5.0	60.6
5	Filter Tuning	20.0	882.0
5	Filter Tuning	30.0	396.0

Table 5. Test Cases for X=20 and Y=1  
(with dark current)

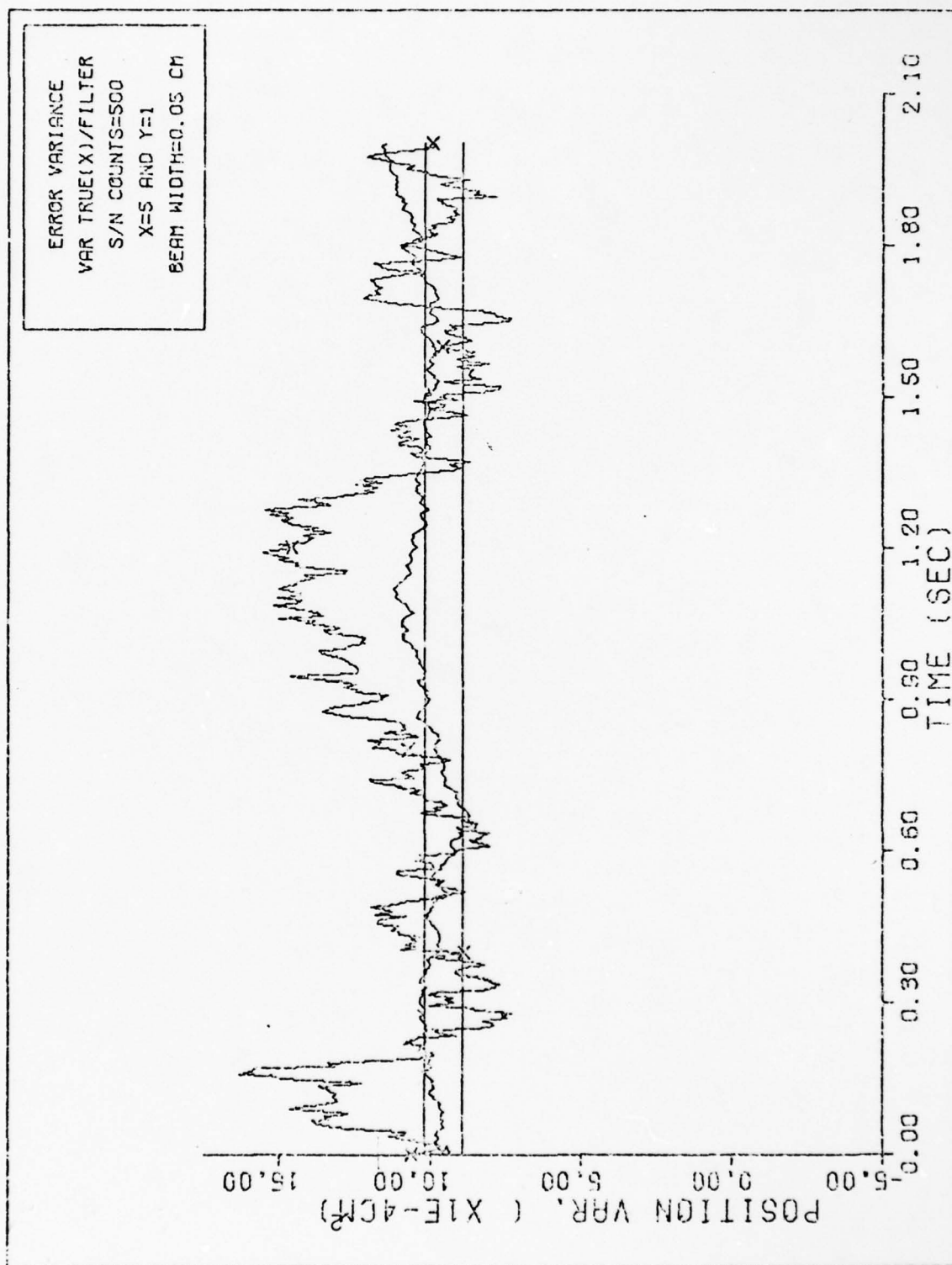


Figure 33a X-POSITION VARIANCES  
(RESIDUAL MONITORING)



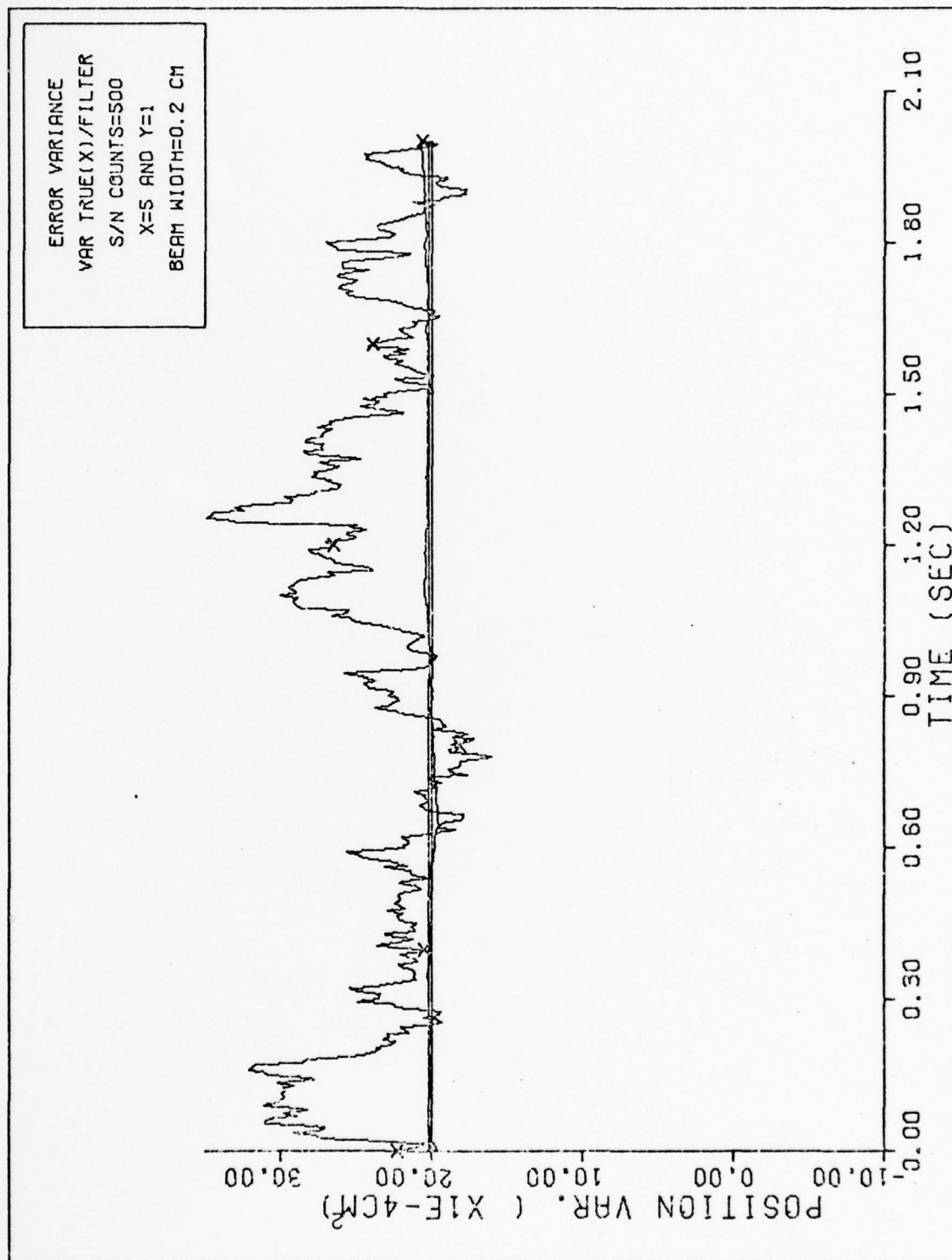


Figure 33b X-POSITION VARIANCES  
(FILTER TUNING)

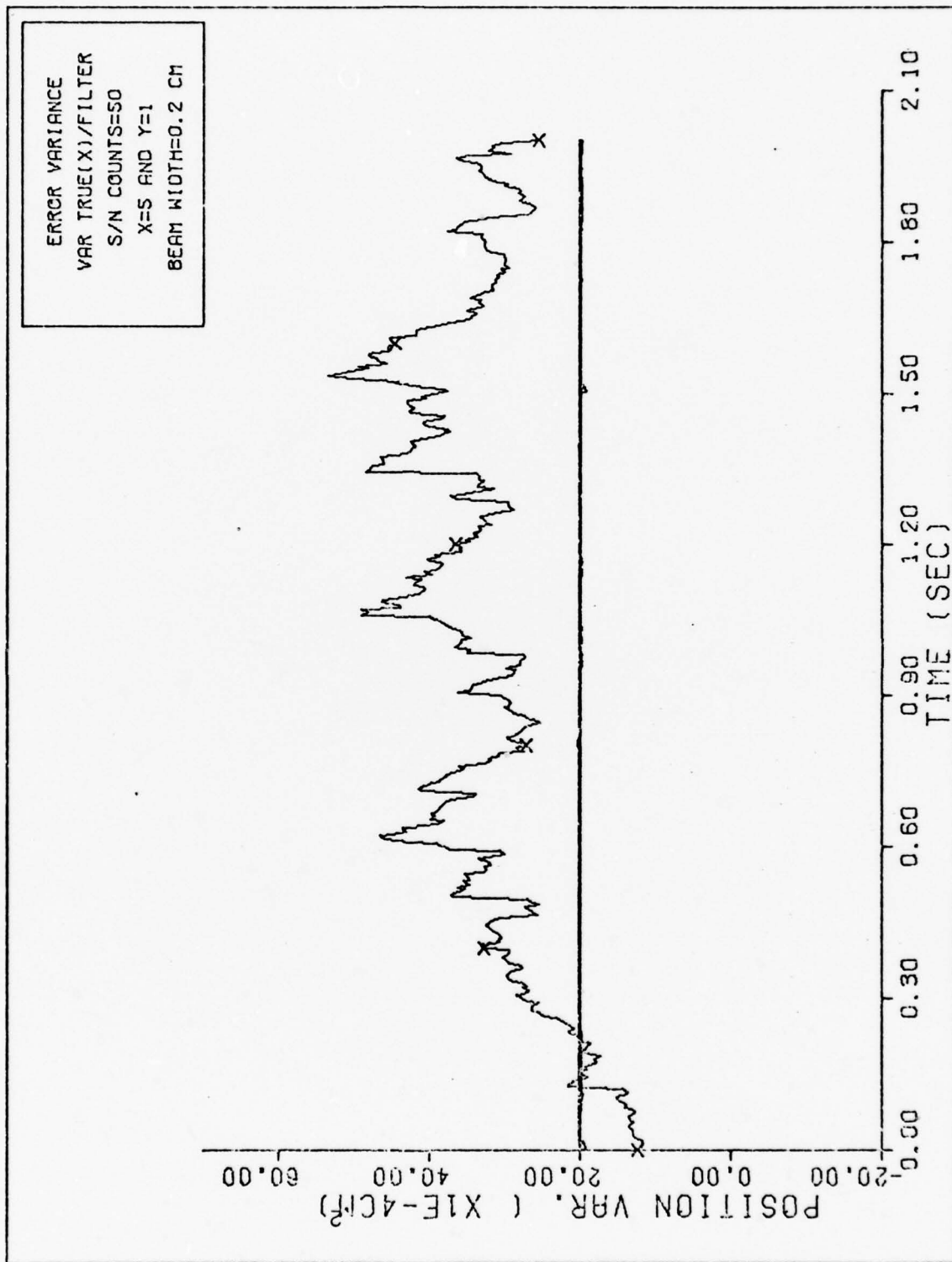


Figure 34b X-POSITION VARIANCES  
(FILTER TUNING)

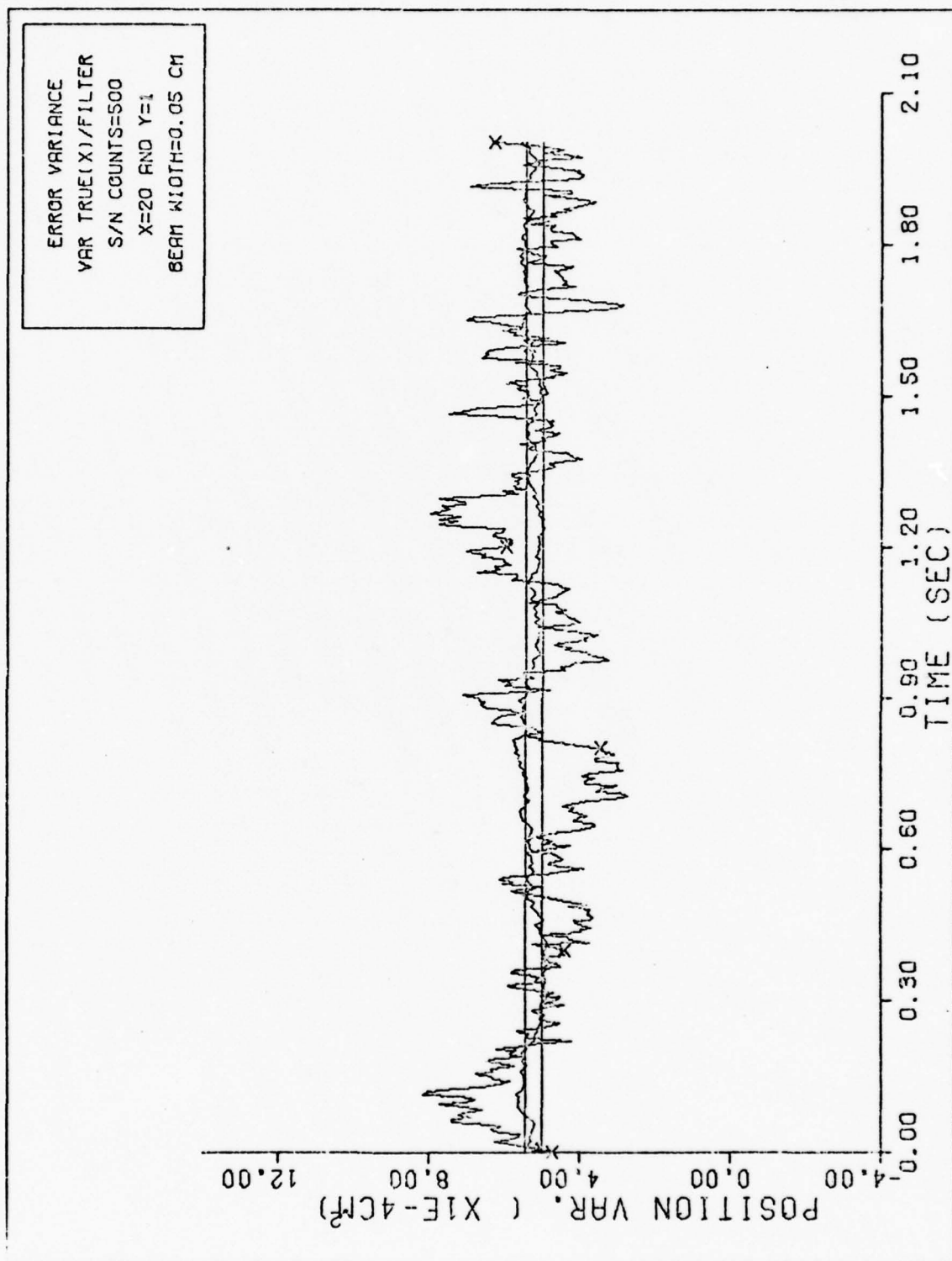


Figure 35a X-POSITION VARIANCES  
 (RESIDUAL MONITORING)

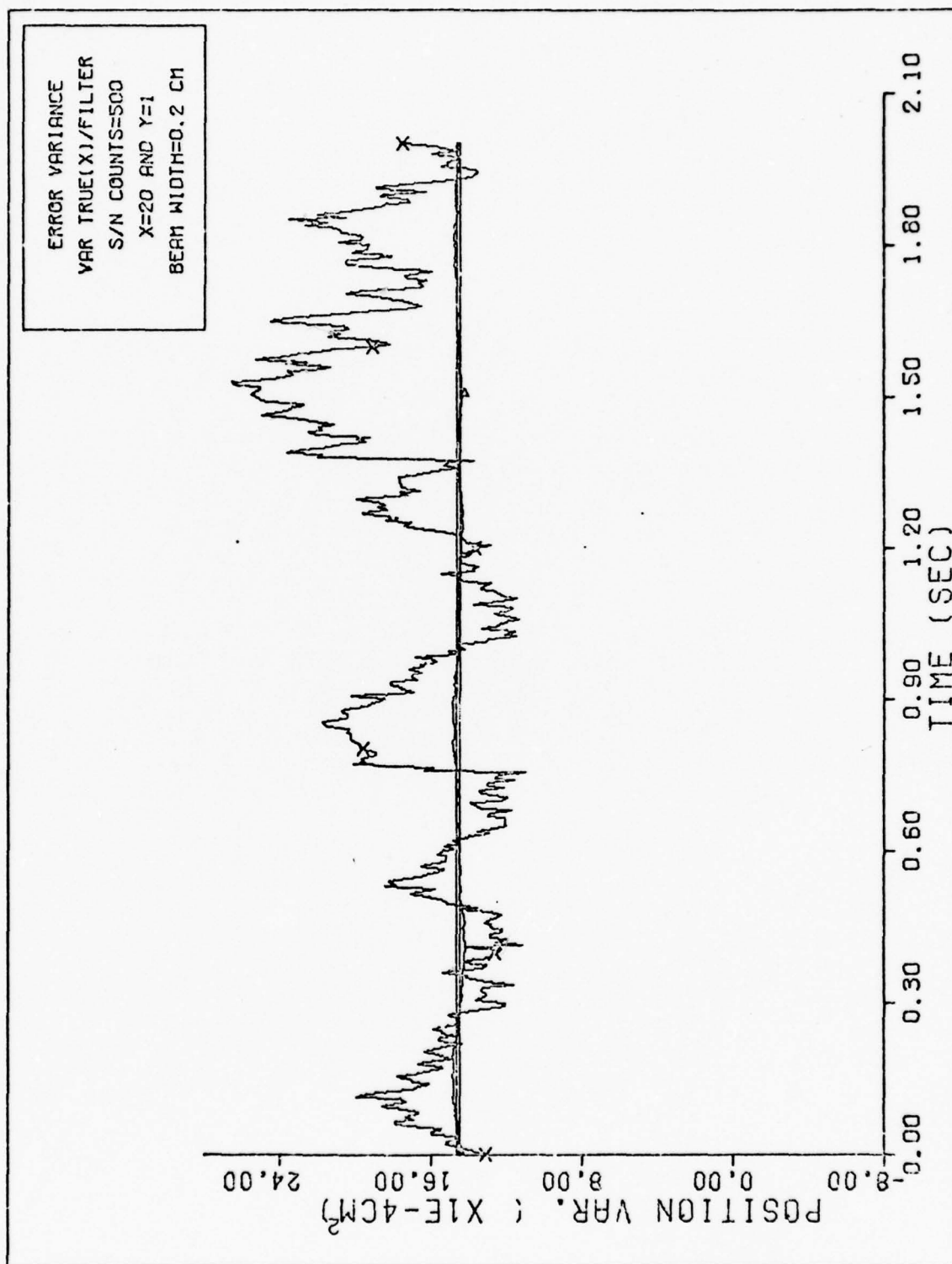


Figure 35b X-POSITION VARIANCES  
(FILTER TUNING)

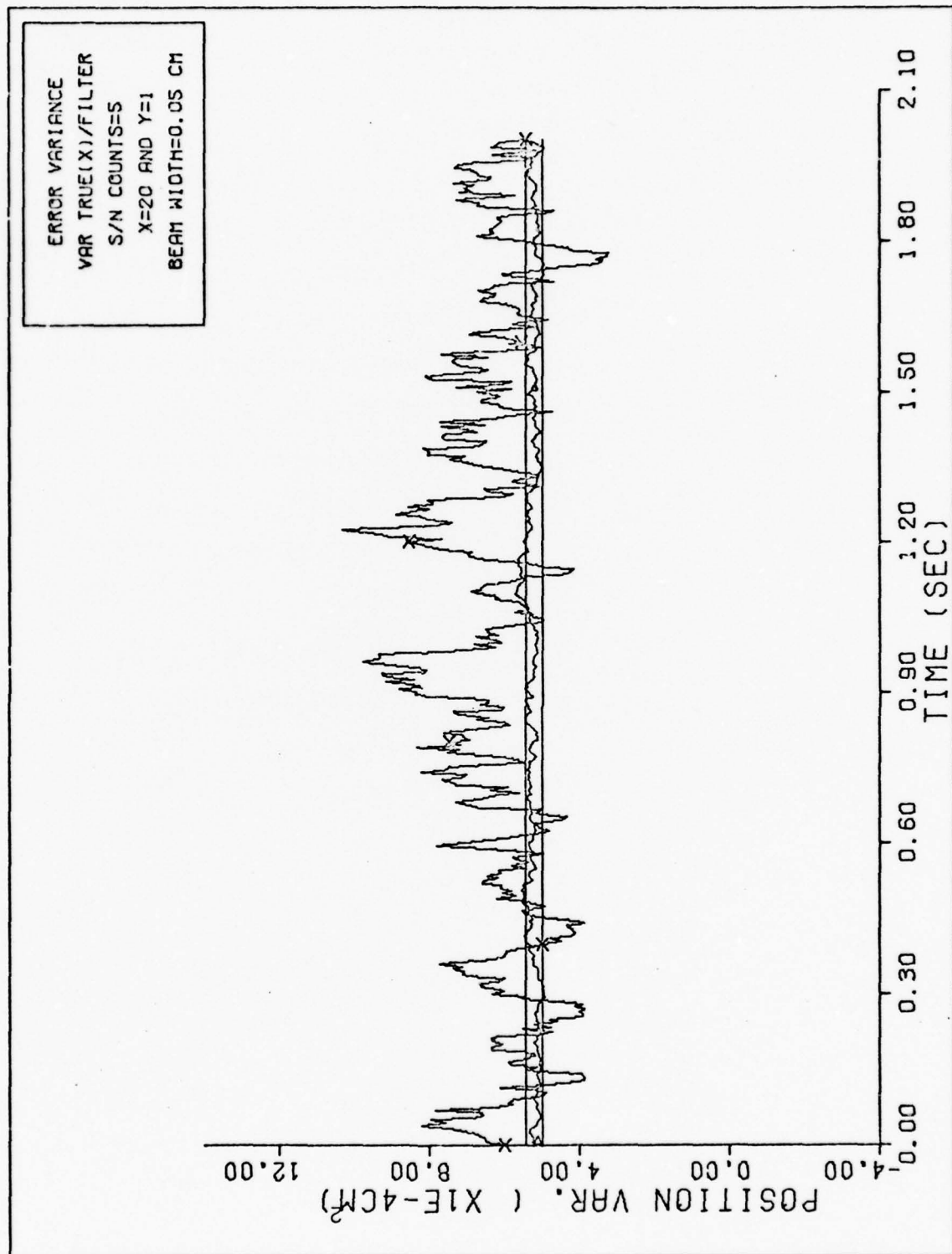


Figure 36a X-POSITION VARIANCES  
(RESIDUAL MONITORING)



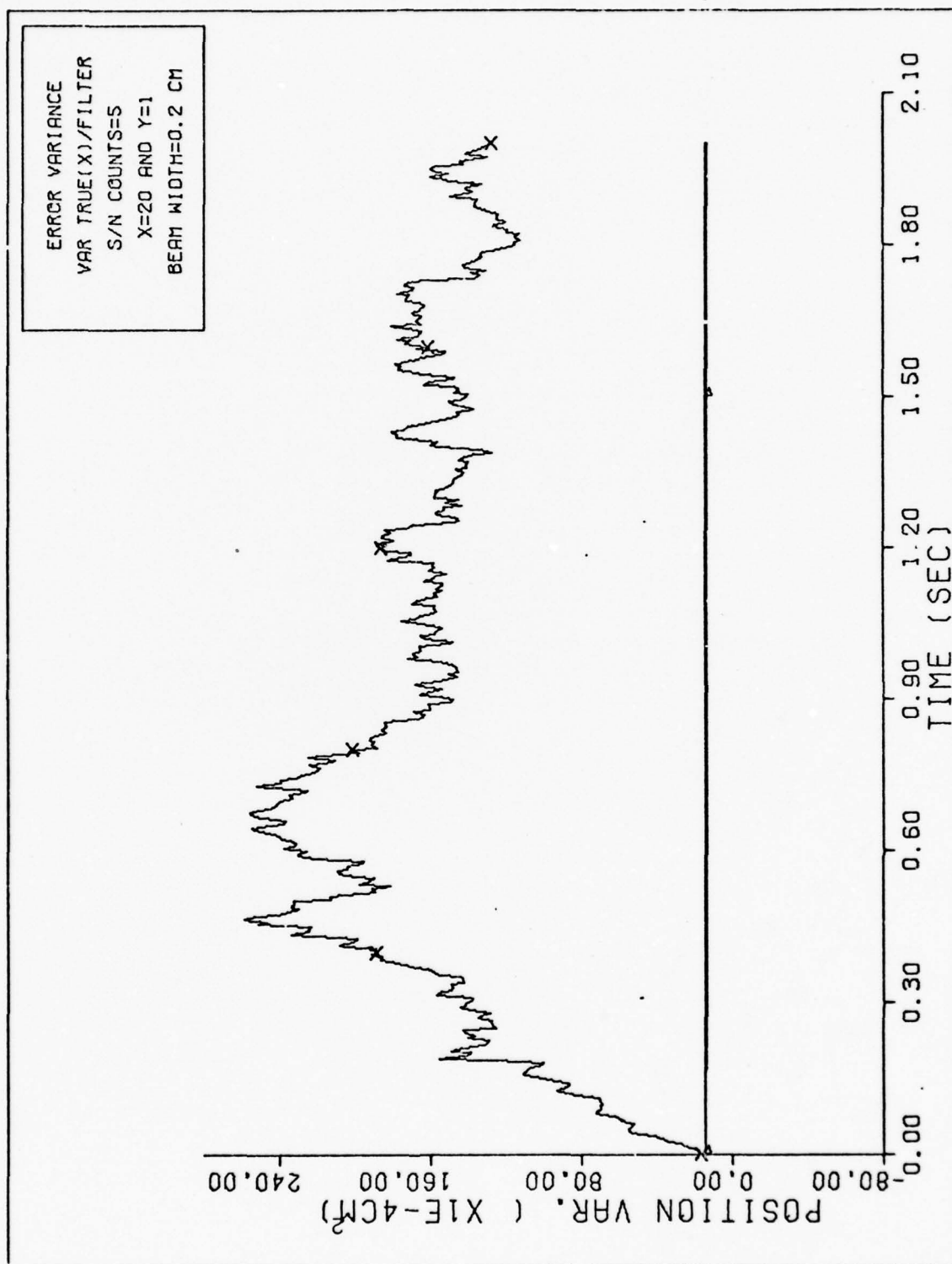


Figure 36b X-POSITION VARIANCES  
(FILTER TUNING)

### Summary

For the test cases considered, the filter's average performance lies near the upper bound curve, which seems reasonable since the set of parameters is selected to yield relatively poor tracking (i.e., few signal counts per coherence time).

When dark current is included in the measurement model of the Snyder Filter, the estimator is found to be very sensitive to dark measurements and tracking performance is degraded substantially.

Based on physical arguments and simulation results, residual monitoring provides a better method to compensate for the effects of dark current than filter tuning.

## V Conclusions and Recommendations

### Conclusions

Assuming no dark current, the average error performance of the Snyder Filter can be described by steady-state upper and lower bounds on mean square error (MSE). These bounds are evaluated as a function of two physically motivated parameters. These parameters are described as: (1) the average number of signal photoelectrons observed in a coherence time of spot's dynamics, and (2) the spot's jitter normalized by the square of the beam width. Based on these parameters, sufficient conditions are presented such that the bounds converge to the actual performance. When sufficient conditions are not established, the results from the Monte Carlo simulation indicate that actual performance can be described by the upper bound (in this study, the conditions correspond to low signal counts per coherence time).

Presenting the dark measurements in the simulation gave further insights into the tracking capabilities of the Snyder Filter. Even for an average signal-to-noise counts ratio of 500, the results show that this estimator was highly sensitive to dark measurements. Thus, the Snyder Filter treats all events as signal.

Based on simulation results and physical arguments, residual monitoring is a better way to handle the dark events rather than increasing the beam width. This can be explained as follows: by increasing the assumed beam width, the Snyder Filter puts less

weight on the dark measurements. At the same time, more events will be assumed to be distributed from the spot's centroid. Thus, the filter will not weigh heavily the measurement due to the spot's Gaussian intensity profile. Also, the Snyder Filter assumes the measurements are from a large photosensitive surface, and therefore the beam width must be very wide to "wash" out the dark current effects. On the other hand, residual monitoring is a method that involves testing for dark events. In this study, if a measurement (i.e., event location) occurred that is three beam widths away from the position of maximum intensity, the Snyder Filter would not process this measurement. Hence, it is unnecessary to increase the beam width in residual monitoring. For high signal-to-noise counts ratio, residual monitoring can be used effectively. Results from the simulation demonstrate this physical reasoning.

#### Recommendations

An area of recommended research is to conduct this study in two dimensions which would investigate different equal intensity ellipsoidal shapes of the spot's intensity profile. Also, investigation of other intensity profiles besides the assumed Gaussian-shaped may warrant further research. The effects in filter performance can then be investigated.

Another issue of research is how to incorporate the point-process measurements. This study was performed in which the rate function was chosen to have a low value, but in the real world, rates of  $10^{10}$  events per second can occur on the detector surface. This imposes a very strict requirement of computation on-line. A suggestion was made to store the photoelectrons in

charged-coupled devices. Then the Snyder Filter can process its measurement at fixed time intervals. In this case, multiple measurements are available to the Snyder Filter. Then, how does one process these stored or "batch" measurements, and how does one account for different arrival times (if at all)? This creates an area of research that warrants further investigation.

Another illustration in how to incorporate the point-process measurements is the issue of simultaneous events encountered in the study. How would one process these multiple measurements at single time instant in the structure? Obviously there is more information concerning the spot's position of maximum intensity (assuming no dark current). This question should be answered with further research.

This study analyzed the Snyder Filter in open-loop configuration; thus, a follow-on study with control inputs to position-sensitive devices, such as a mirror, warrants further investigation.

A final issue and recommendation is to develop ad-hoc methods in how to handle the dark current effects for low signal-to-noise counts ratio. Since residual monitoring was found to be a more effective method of compensation than filter tuning, different methods using residual monitoring should be investigated.



### Bibliography

1. Snyder, Donald L., How to Track a Swarm of Fireflies by Observing Their Flashes, "IEEE Trans. on Information Theory, (Nov. 1975).
2. Gagliardi, Robert M. and Shermann Karp. Optical Communications, New York: John Wiley and Sons Inc., 1976.
3. Snyder, Donald L., Random Point Processes, New York: John Wiley and Sons Inc., 1975.
4. Rhodes, Ian B. and Donald L. Snyder, Estimation and Control Performance for Space-Time Point-Process Observations, IEEE Trans on Automatic Control (June 1977).
5. Pratt, William K., Laser Communication Systems. New York: John Wiley and Sons, Inc., 1969.
6. Yariv, Amnon., Introduction to Optical Electronics (Second Edition) Chicago: Holt; Rhinehark and Wintron, 1976.
7. Karp, Sherman, E.L. O'Neill, and R. M. Gagliardi, Communication Theory for the Free-Space Optical Channel, Proc. IEEE, 58, No. 10, 1611-1626, Oct 1976.
8. Hoverstern, E. V., R. O. Harger, and S. J. Holme, Communication Theory for the Turbulent Atmosphere, Proc IEEE, 58, No. 10 16-26, Oct 1970.
9. Maybeck, Peter S., Stochastic Estimation and Control Systems, Part 1 (Notes for EE 7.65) Wright-Patterson Air Force Base, Ohio, Air Force Institute of Technology, 1977.
10. Lewantowitz, Zdzislaw H., Laser Pointing and Tracking Using an Adaptive Extended Kalman Filter, Unpublished Thesis, Wright-Patterson Air Force Base, Ohio: Air Force Institute of Technology, July 1975.
11. Wozencraft, John M. and Irwin M. Jacobs, Principles of Communication Theory, Wiley and Sons, 1965.
12. Davenport, Wilbur B., Probability and Random Processes- An Introduction for Applied Scientists, and Engineers, McGraw-Hill Book Company, 1970.
13. Jackson, Kenneth L., Users Guide for A Generalized Monte-Carlo Analysis Program (MCAP) to Kalman Filter Design, Wright-Patterson Air Force Base, Ohio, Air Force Institute of Technology, December 1977.

## Appendix A

### Statistics of a Time-Space Point Process

The purpose of this appendix is to derive the statistics of a point-process in time and space based on an incremental description. In its application of this report, we define a rate function to be

$$\lambda(t, \vec{r}) = \frac{\eta}{hf_0} \int_{A_d} |U_d(t, \vec{r})|^2 d\vec{r}; \quad d\vec{r} = dx dy$$

where  $t$  denotes the time continuum,  $\vec{r}$  is the dummy variable representing a location on a photodetector surface,  $\eta$  is the quantum efficiency,  $h$  is Planck's constant,  $A_d$  is the detector surface area,  $U_d$  is the complex field envelope,  $f_0$  is frequency of the input field,  $dx$  is differential length along x-axis,  $dy$  is differential length along y-axis and  $|\cdot|$  is modulus of field envelop. This rate function describes the intensity of events appearing on the detector surface in time and space.

Shown in Fig. A1 is a detector array of photon or quantum detectors which can measure the temporal and spatial location of a photon-to-electron conversion.

It is assumed that each photon-to-electron conversion or event on the detector surface is independent. Then based on its incremental properties the x-axis, y-axis, and t-axis are partitioned into intervals as shown in Fig. A-2:

Then, with  $r_{k=\Delta}(x_k, y_k)$ , the incremental description is as follows:

$$P \left[ \begin{array}{l} \text{event occurring} \\ \text{in } \Delta t \Delta A \text{ at} \\ (t_k, \bar{r}_k) \end{array} \right] = \lambda(t, \bar{r}) \Delta t \Delta A + o(\Delta t \Delta A) \quad (A-1)$$

$$P \left[ \begin{array}{l} \text{no event occurring} \\ \text{in } \Delta t \Delta A \text{ at} \\ (t_k, \bar{r}_k) \end{array} \right] = 1 - \lambda(t, \bar{r}) \Delta t \Delta A + o(\Delta t \Delta A) \quad (A-2)$$

$$P \left[ \begin{array}{l} \text{more than one} \\ \text{event in } \Delta t \Delta A \\ (t_k, \bar{r}_k) \end{array} \right] = o(\Delta t \Delta A) \quad (A-3)$$

where  $P[\cdot]$  denotes probability, of  $o(\Delta t \Delta A)$  are higher order terms of  $o(\Delta t \Delta A)$  with limit  $\lim_{\Delta t \Delta A \rightarrow 0} \frac{o(\Delta t \Delta A)}{\Delta t \Delta A} = 0$ . It is desirable to obtain a statistical description of event times  $t_k$ 's event locations  $r_k$ 's, and the number of events  $n$ , appearing on entire detector surface  $A_d$ , in a time interval  $[0, t]$ . Thus, we need the joint probability density function of these random variables  $t_k$ ,  $\bar{r}_k$ , and  $n$  (i.e.  $f[\{t_k\}, \{\bar{r}_k\}, n]$  where  $\{\cdot\}$  denotes set of event locations or times.  $f[\{t_k\}, \{\bar{r}_k\}, n]$  completely characterizes the output process from the detector surface.

To obtain  $f[\{t_k\}, \{\bar{r}_k\}, n]$ , consider a counting process  $N_t$  which is depicted in Fig. A-3.

The point process probability distribution for  $N_t$  (i.e.,  $P[N_t = n]$ ) will be derived using characteristic functions. Note that the process  $N_t$  is the number of events regardless of when and where the event occurred. Since  $N_t$  is a discrete random variable,

$$\begin{aligned} E[e^{jvN_t}] &= e^{j(0)} P[N_t = 0] + e^{jv} P[N_t = 1] \\ &+ e^{j2v} P[N_t = 2] + \dots + e^{jv} P[N_t = n] \end{aligned} \quad (A-4)$$

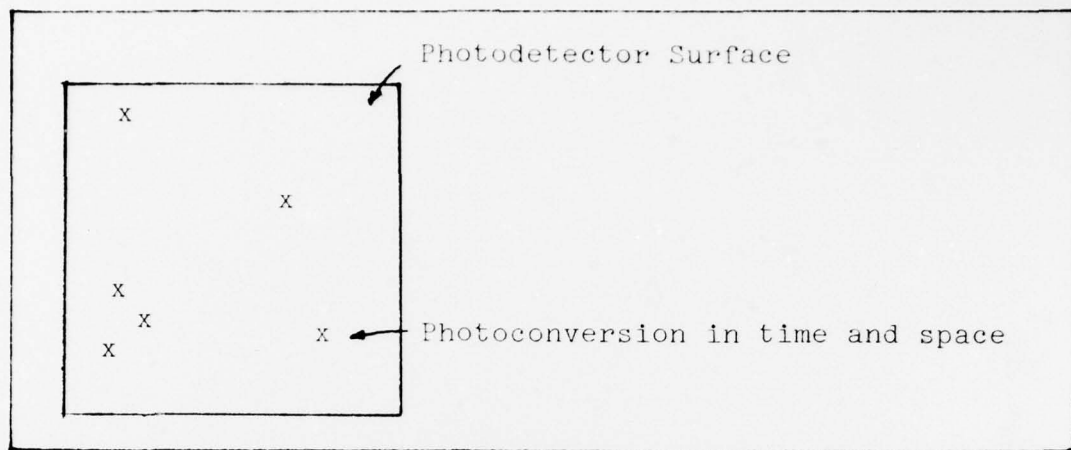


Fig A.1 Infinitely fine detector array.

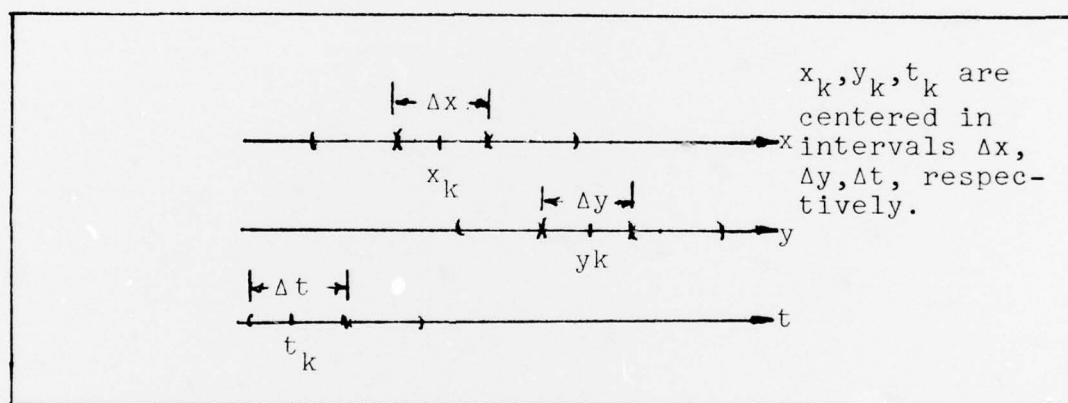


Fig A.2 Partitions of  $x$ -axis,  $y$ -axis and  $t$ -axis

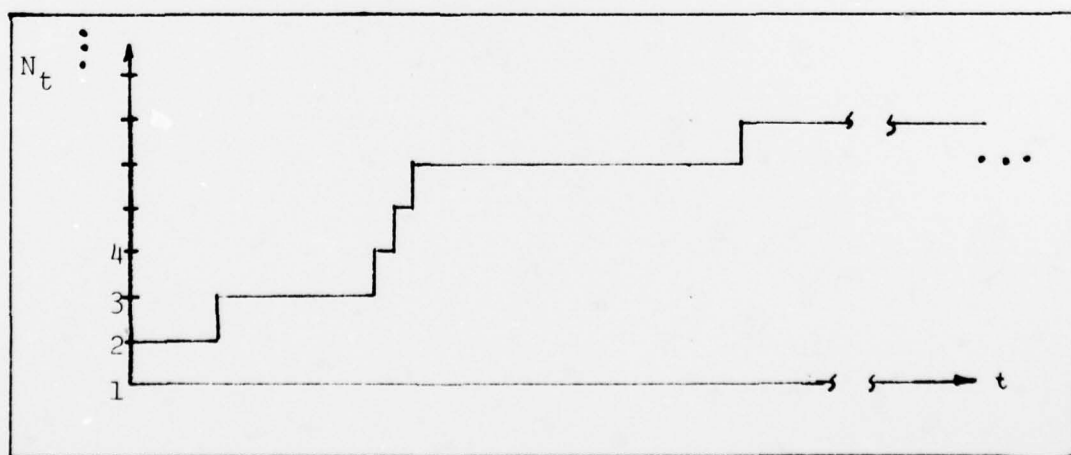


Fig A.3 Time-Space Counting Process

Let  $n_i$  be a random variable that is equal to a one in which an event occurred in  $\Delta t \Delta A$  or a zero in which case no event occurred. It then follows that  $N_t = \sum_{k=1}^n n_k$  where  $k = 0, 1, 2, 3, \dots, n$ . Then Eq. (A-4) becomes

$$\begin{aligned} E[e^{jvN_t}] &= E[\exp(jv \sum_{k=1}^{N_t} n_k)] \\ &= \prod_{k=1}^{N_t} E[\exp(jvn_k)] \end{aligned} \quad (A-5)$$

where we have used the property of statistical independence of events. Upon using Eqs. (A-1) through (A-3), Eq. (A-5) becomes

$$\begin{aligned} E[e^{jvN_t}] &= \prod_{k=1}^{N_t} e^{jv \lambda(t_k, \bar{r}_k) \Delta t \Delta A} + e^{jv_0 [1 - \lambda(t_k, \bar{r}_k) \Delta t \Delta A] + o(\Delta t \Delta A)} \\ &= \prod_{k=1}^{N_t} \lambda(t_k, \bar{r}_k) \Delta t \Delta A (e^{jv} - 1) + 1 + o(\Delta t \Delta A) \\ &= \exp \sum_{k=1}^{N_t} \ln[1 + \lambda(t_k, \bar{r}_k) \Delta t \Delta A (e^{jv} - 1) + o(\Delta t \Delta A)] \end{aligned} \quad (A-6)$$

and using  $\ln(1+z) \approx z$  for small  $z$ , Eq (A-6) becomes

$$E[e^{jvN_t}] = \exp \left[ \sum_{k=1}^{N_t} \lambda(t_k, \bar{r}_k) \Delta t \Delta A (e^{jv} - 1) \right]$$

Also, as  $\Delta t \Delta A \rightarrow 0$ , the sum in the above relation becomes a definite integral so that

$$E[e^{jvN_t}] = \exp[(e^{jv} - 1) \int_{A_d} \int_0^t \lambda(\alpha, \bar{\beta}) d\alpha d\bar{\beta}] \quad (A-7)$$

with the series expansion of  $\exp(x) = 1 + x + \frac{x^2}{2!} + \dots$



Eq (A-7) yields

$$E[e^{jvN_t}] = \exp(-\mu_{A_d,t}).$$

$$\left( 1 + e^{jv \exp(\mu_{A_d,t})} + \frac{e^{2jv [\exp(\mu_{A_d,t})]^2}}{2!} + \dots + \frac{e^{jv [\exp(\mu_{A_d,t})]^n}}{n!} \right) \quad (A-8)$$

where  $\mu_{A_d,t} = \int_{A_d} \int_0^t \lambda(t, \bar{r}) d\alpha, d\bar{\beta}$

Comparing Eq. (A-8) with Eq. (A-4), we obtain

$$P[N_t = n] = \frac{(\mu_{A_d,t})^n \exp(-\mu_{A_d,t})}{n!} \quad (A-9)$$

Eq (A-9) describes the counting process  $N_t$  in interval  $[0, t]$  without regard to the event times and event locations.

To obtain  $f[\{t_k\}, \{\bar{r}_k\}, n]$ , and using independence of events, consider the following probabilities:

$$P[\text{one event at } (t_1, \bar{r}_1)] = \lambda(t_1, \bar{r}_1) \Delta t \Delta A \quad (A-10)$$

$$P[\text{one event at } (t_1, r_1) \text{ and no events in } [t, T]] =$$

$$= \lambda(t_1, r_1) \Delta t \Delta A \exp\left(- \int_{A_d} \int_{t_1}^t \lambda(\alpha, \bar{\beta}) d\alpha d\bar{\beta}\right) \quad (A-11)$$

Finally, the probability density function of the ordered event times, event locations, and the number of events in  $[0, T]$  on  $A_d$  is defined

$$f[\{t_k\}, \{r_k\}, n] = \lim_{\Delta t \Delta A \rightarrow 0} \frac{P[;]}{(\Delta t \Delta A)^n} \quad (A-12)$$

where  $P[;]$  denotes the probability of one event at  $(t_1, \bar{r}_1)$ , one at  $(t_2, r_2)$ , ..., one at  $(t_k, r_k)$ . Using the Eqs (A-10) and (A-11), (A-12) will yield

$$f[\{t_k\}, \{r_k\}, n] = \exp\left(- \int_{A_d} \int_0^t \lambda(\alpha, \bar{\beta}) d\alpha d\bar{\beta}\right) \prod_{k=1}^n \lambda(t_k, r_k) \quad (A-13)$$

Eq (13) completely characterizes the statistical output process of the detector surface.

Since this report simulates the detector output in one dimension, simply replace  $\bar{r}_k$  with  $r_k$ , to yield

$$f\{t_k, r_k, n\} = \exp\left(- \int_{\ell} \int_0^t \lambda(\alpha, \beta)(\alpha, \beta) \prod_{k=1}^n \lambda(t_k, t_k)\right) \quad (A-14)$$

where  $\ell$  is detector length.

To obtain the joint probability density of event times and number of events without regard to where the events occurred (i.e.  $f\{\{t_k\}, n\}$ ), Eq (A-11) will yield the marginal density

$$f\{\{t_k\}, n\} = \exp\left(- \int_{\ell} \int_0^t \lambda(\alpha, \beta)(\alpha, \beta) \prod_{i=1}^n \int_{\ell} \lambda(\alpha, \beta) d\alpha\right)$$

where the rate function @  $\lambda(r_k, t_k)$  is integrated over the detector length yielding no spatial dependence on  $\int_{\ell} \lambda(\alpha_k, t_k) d\alpha$

This completes the statistical description of a time-space point process which characterizes the output of a photo-sensitive surface.

## Appendix B

### Upper and Lower Bounds on Mean Square Error

The Snyder Filter is a minimum mean-square-error estimator that uses time-space point process observations. The purpose of this appendix is to solve the upper and lower bounds on mean-square-error (MSE) in order to evaluate the estimation performance of the Snyder Filter. Also, the bounds, derived in Ref. 4 are solved in steady-state (i.e.,  $\frac{dP^*}{dt} = \frac{dP_*}{dt} = 0$ ). Parameters are defined from the dynamical equation of  $P^*$  and  $P_*$  to provide meaningful physical descriptions about the actual performance of the Snyder Filter. Based on these parameters, sufficient conditions can be established, such that the bounds are identical; thus, actual performance can be determined. However, when the parameters do not establish sufficient conditions, the bounds are no longer identical, and actual performance is difficult to obtain. These parameters will now be derived in one dimension which involves only estimation performance.

The parameters are derived in one-dimension for a spot's dynamics to be modelled as a Scalar First-Order Markov process. In addition, this solution only involves estimation performance.

Consider the spot's centroid (or position of maximum intensity) which is modelled by a linear stochastic differential equation

$$dx(t) = F(t)x(t)dt + G(t)d\beta(t) \quad (B-1)$$

where  $x(t)$  is position of maximum intensity,  $\beta(t)$  is a Wiener process,  $F(t)$  is the state coefficient, and  $G(t)$  is the noise

input coefficient. The time-space point process has a rate function modelled as

$$\lambda(r, \underline{x}(t), t) = \mu(t) \gamma(r, \underline{x}(t)) \quad (B-2)$$

where

$$\mu(t) = \frac{n I_0(t)}{h f_0} \sqrt{2\pi} \sigma \quad (B-3)$$

$$\gamma(r, x_t) = \frac{1}{\sqrt{2\pi}\sigma} \exp\left\{-\frac{(r-x(t))^2}{2\sigma^2}\right\} \quad (B-4)$$

with  $r$  is a dummy variable for spatial location on detector, and  $\sigma$  is the beam width.

The lower bound on MSE, denoted as  $P_*(t)$ , is described by the following differential equation that is specialized in one-dimensional space as

$$\begin{aligned} \frac{dP_*}{dt} = & F(t)P_*(t) + P_*(t)F(t) + G(t)Q(t)G(t) \\ & - P_*^2(t)\left[\frac{\mu}{\sigma^2}\right] \end{aligned} \quad (B-5)$$

where  $\mu = E[\mu(t)]$ ;  $E[\cdot]$  = expected value operator

$Q(t)$  is strength of  $\beta(t)$

The lower bound is specialized for the following assumptions:

(1)  $\underline{x}$  is modelled as an output process of a First Order Lag; then  $F(t) = -\frac{1}{\tau_c}$  and its state transition function is  $\phi(t, \tau) = e^{-(t-\tau)/\tau_c}$ . The strength  $Q$  of the white noise driving the First Order lag is given in Ref (9) as  $Q = \frac{-2}{\tau_c} \sigma_x^2$



to obtain stationary statistics at the output.  $\sigma_x^2$  is the mean square value of the spot's displacement on the detector surface (i.e.  $E[\tilde{x}(t)\tilde{x}(t+\tau)] = \sigma_x^2 e^{-(\tau)\tau_c}$ ) and (2)  $G(t) = 1$ . Eq (B-6) will yield,

$$\frac{dP_*}{dt} = \frac{-2}{\tau_c} P_* + Q - \frac{\mu}{\sigma^2} P_*^2 \quad (B-6)$$

Solving for steady state  $\frac{dP_*}{dt} = 0$ , yields a quadratic equation which is expressed as

$$P_* = \frac{2\sigma^2}{2\tau_c\bar{\mu}} + \frac{1}{2} \left[ \left( \frac{2\sigma^2}{\tau_c\bar{\mu}} \right)^2 + 4 \left( \frac{Q\sigma^2}{\bar{\mu}} \right) \right]^{1/2} \quad (B-7)$$

$$\begin{aligned} &= \left( \frac{\sigma^2}{2} \left( \frac{2}{\tau_c\bar{\mu}} \right) \right) \left( -1 + \left[ 1 + 4 \left( \frac{Q\sigma^2}{\bar{\mu}} \right) \left( \frac{\tau_c\bar{\mu}}{2\sigma^2} \right)^2 \right]^{1/2} \right) \\ &= \left( \frac{\sigma^2}{2} \left( \frac{1}{\bar{\mu} \frac{\tau_c}{2}} \right) \right) \left( -1 + \left[ 1 + 4 \left( \frac{Q\tau_c}{2\sigma^2} \right) \left( \frac{\tau_c\bar{\mu}}{2} \right) \right]^{1/2} \right) \end{aligned} \quad (B-8)$$

Dividing Eq (B-8) by  $\sigma^2$  and defining  $X = \frac{\tau_c\bar{\mu}}{2}$ ,  $Y = \frac{Q\tau_c}{2\sigma^2}$  yields

$$\frac{P_*}{\sigma^2} = \frac{1}{2X} \left( -1 + [1 + 4XY]^{1/2} \right) \quad (B-9)$$

But,  $\bar{\mu} = \frac{\eta I_o}{hf_o} \sqrt{2\pi\sigma}$  and  $Q = \frac{2\sigma_x^2}{\tau_c}$ , and substituting into  $X$  and  $Y$  gives

$$X = \left( \frac{\eta}{hf_o} I_o \sqrt{2\pi\sigma} \right) \left( \frac{\tau_c}{2} \right) \quad Y = \frac{\sigma_x^2}{\sigma^2}, \quad (B-10)$$

X describes the average number of photons detected in a coherence time of the spot's dynamics and Y results in the spot's jitter normalized by the square of the beam width. These parameters are discussed in detail in Chapter II.

The relation for the upper bound on MSE is expressed as

$$\frac{dP^*}{dt} = FP^* + P^*F + GQG - \bar{\mu}P^*[P^* + \sigma^2]^{-1} P^* \quad (B-11)$$

Applying the same assumptions as in  $P_*$ , Eq (B-11) yields

$$\frac{dP^*}{dt} = \frac{-2}{\tau_c} P^* + Q - \frac{-\bar{\mu}P^{*2}}{P^* + \sigma^2}$$

For  $\frac{dP^*}{dt} = 0$  yields another quadratic equation which solves for

$$\begin{aligned} P^* &= \frac{1}{2} \left\{ \frac{Q - \frac{2\sigma^2}{\tau_c}}{\frac{2}{\tau_c} + \bar{\mu}} + \left[ \frac{Q - \frac{2\sigma^2}{\tau_c}}{\frac{2}{\tau_c} + \bar{\mu}} + \frac{4Q\sigma^2\tau_c}{\frac{2}{\tau_c} + \bar{\mu}} \right]^{\frac{1}{2}} \right\} \\ &= \frac{1}{2} \left\{ \frac{Q\tau_c - 2\sigma^2}{2 + \bar{\mu}\tau_c} + \left[ \frac{Q\tau_c - 2\sigma^2}{2 + \bar{\mu}\tau_c} + \frac{4Q\sigma^2\tau_c}{2 + \bar{\mu}\tau_c} \right]^{\frac{1}{2}} \right\} \\ &= \frac{1}{2} \left\{ \frac{\sigma^2}{(1 + \frac{\bar{\mu}\tau_c}{2})} \right\} \left( \frac{Q\tau_c}{2\sigma^2} - 1 \right) + \left[ \left( \frac{Q\tau_c}{2\sigma^2} - 1 \right)^2 \right. \\ &\quad \left. + 4 \left( \frac{Q\tau_c}{2\sigma^2} \right) \left( 1 + \frac{\bar{\mu}\tau_c}{2} \right) \right]^{\frac{1}{2}} \quad (B-12) \end{aligned}$$

Again, letting  $X = \frac{\bar{\mu}\tau_c}{2}$ ,  $Y = \frac{Q\tau_c}{2\sigma^2}$ , and dividing  $\sigma^2$

into Eq (B-12) yields

$$\frac{P^*}{\sigma^2} = \left( \frac{1}{2(X+1)} \right) \left( (Y-1)^2 + [(Y+1)^2 + 4(X+1)Y]^{1/2} \right)$$

where X and Y is defined in (B-10). Note that for  $X \gg 1$   
 $Y \ll 1$ , the bounds converge to actual mean square-error. These  
conditions are discussed in Chapter II.

### Vita

John Mangona Santiago, Jr., was born on 15 July 1956 in Los Angeles, CA. On June 1977 he graduated from the University of California, Los Angeles with a Bachelor of Science degree, and was commissioned in the Air Force through Reserve Officer Training Corps. He entered active duty in June 1977 to be assigned to the Air Force Institute of Technology in pursuit of the Master's Degree in Electrical Engineering, Electro-optics.

Permanent Address: 2350 Elmgrove St  
Los Angeles, CA 90031

UNCLASSIFIED

SECURITY CLASSIFICATION OF THIS PAGE (When Data Entered)

REPORT DOCUMENTATION PAGE		READ INSTRUCTIONS BEFORE COMPLETING FORM
1. REPORT NUMBER AFIT/GEO/EE/78-4	2. GOVT ACCESSION NO.	3. RECIPIENT'S CATALOG NUMBER
4. TITLE (and Subtitle) FUNDAMENTAL LIMITATIONS OF OPTICAL TRACKERS		5. TYPE OF REPORT & PERIOD COVERED MS Thesis
		6. PERFORMING ORG. REPORT NUMBER
7. AUTHOR(s) John M. Santiago, Jr. 2nd Lt USAF		8. CONTRACT OR GRANT NUMBER(s)
9. PERFORMING ORGANIZATION NAME AND ADDRESS Air Force Institute of Technology (ATC) AFIT/EN Wright-Patterson AFB, OH 45433		10. PROGRAM ELEMENT, PROJECT, TASK AREA & WORK UNIT NUMBERS
11. CONTROLLING OFFICE NAME AND ADDRESS		12. REPORT DATE December 1978
		13. NUMBER OF PAGES 165
14. MONITORING AGENCY NAME & ADDRESS (if different from Controlling Office) Air Force Weapons Laboratory (AFWL/ALO) Air Force Systems Command Kirtland AFB, NM		15. SECURITY CLASS. (of this report) UNCLASSIFIED
		15a. DECLASSIFICATION/DOWNGRADING SCHEDULE
16. DISTRIBUTION STATEMENT (of this Report) Approved for public release; distribution unlimited		
17. DISTRIBUTION STATEMENT (of the abstract entered in Block 20, if different from Report)		
18. SUPPLEMENTARY NOTES Approved for public release; IAW AFR 190-17 JOSEPH P. HIBBS, Major, USAF Director of Information 1-23-79		
19. KEY WORDS (Continue on reverse side if necessary and identify by block number) Optical Trackers Direct Detection Direct Detection Optical Receiver Time-Space Point Process Quantum-Limit		
20. ABSTRACT (Continue on reverse side if necessary and identify by block number) A problem is considered to determine the tracking capabilities of an estimator, applied in optical sensing. The estimator tracks the centroid of a one-dimensional Gaussian-shaped intensity based on time-space point process measurements. The centroid assumes to move dynamically as a First Order Gauss-Markov process. Filter performance is described by steady-state upper and lower bounds on mean-square-error (MSE) which are evaluated as a function of two physically motivated parameters: average number of photons		

DD FORM 1 JAN 73 1473

EDITION OF 1 NOV 65 IS OBSOLETE

UNCLASSIFIED

SECURITY CLASSIFICATION OF THIS PAGE (When Data Entered)



UNCLASSIFIED

SECURITY CLASSIFICATION OF THIS PAGE(When Data Entered)

20. Abstract (continued)

detected in a coherence time of centroid dynamics and mean square of the beam width. The parameters establish regions of operations where upper and lower bounds converge to the actual MSE. Results from the Monte-Carlo simulation demonstrates the bounds usefulness. Noise measurements from dark current or background radiation are included in the simulation. Results show that the filter is very sensitive to these measurements, resulting in very poor tracking. Ad hoc methods of filter tuning and residual monitoring are employed to improve tracking performance; results indicate that filter performance can be improved substantially through residual monitoring.

UNCLASSIFIED

SECURITY CLASSIFICATION OF THIS PAGE(When Data Entered)